TABLE OF CONTENTS

Page

LIST OF TABLES

Page

LIST OF FIGURES

Page

LIST OF ABREVIATIONS AND SYMBOLS

Symbols:

Ac_1 & Ac_3	Critical transformation temperatures
r	Mean equivalent radius of cementite
r_o	Initial mean radius of cementite at the onset of coarsening
r_θ	Average radius of cementite
r_{cell}	Average radius of spherical cell
K	Coarsening constant in multi component system
K_i	Coarsening constant due to i alloying element
k_i	Partition coefficient (Chemical composition ratio of element i in cementite to that in ferrite)
C_e	Equilibrium solute concentration
C_i^α	Chemical composition of i element in ferrite
C_i^θ	Chemical composition of i element in cementite
t	Time
T	Temperature
σ	Interfacial energy
V_m^θ	Molar volume of cementite
V_f^θ	Volume fraction of cementite
R	Universal gas constant
D	Diffusion coefficient
D_i	Diffusion coefficient of i alloying elements
λ	Mean free carbide path or Inter-particle spacing

v^{α}	Migration rate of the interface in ferrite
v^{θ}	Migration rate of interface in cementite
C_i^{α}	Concentration of the component i in matrix adjacent to interface
C_i^{θ}	Concentration of the component i in cementite adjacent to interface
C_i	Concentration in mole per volume
J_i^{α}	Flux of component i on ferrite
J_i^{θ}	Flux of component i on cementite
J_i	Flux of component in multicomponent system i
∇C_j	Concentration gradient of component j
V_{θ}	Volume of cementite
V_{cell}	Volume of the spherical cell
$\nabla \mathrm{G}_m$	Gibbs-Thomson capillarity term
Z1	Hardened zone
Z2	Transition or loss of hardness zone
Z3	Over-tempered zone
Z4	Core zone

Acronymes:

AISI	American Iron and Steel Institute
AMS	Aerospace Material Specification
ASTM	American Society for testing of Materials
ISO	International Organization for Standardization
ÉTS	École de Technologie Supérieure
BASP	Boiling Alkaline Sodium Picrate etching solution

XRD	X-ray diffraction
EDX	Energy-dispersive X-ray
SEM	Scanning electron microscope
BSC	Back scatter secondary electron microscope
BCC	Body centered cubic (crystal structure of ferrite)
FCC	Face centered cubic (crystal structure of cementite)
BCT	Body Centered Tetragonal (crystal structure of martensite)
HRC	Hardness Rockwell C (Unite of hardness measurement Rockwell)
HVx	Hardness Vickers (Unite of micro hardness measurement Vickers using a mass x)
DICTRA	DIffusion Control TRAnsformation software
Thermo-Calc	Thermodynamic calculation software
TCFE7	Thermodynamic database version 7
DIV	Divergence operator
MOBFE2	Mobility database version 2
Q&T	Quenched and tempered
LSW	Lifshitz-Slyozov and Wagner steady state distribution
PSD	Particle size distribution
PLE	Local-equilibrium condition with partitioning
NPLE	Negligible partition local equilibrium
PE	Para-equilibrium condition

INTRODUCTION

A common industrial process for surface hardening is induction hardening. The green process of fast induction heating is increasingly used in the aeronautics industry in power transmission devices. It allows combining speed, repeatability, automation, wear, and fatigue performance of the treated parts, and it is an essential substitute to thermo chemical treatments (Rudnev 2005).

Initial microstructure and process parameters are influenced on the final mechanical properties of heat treated parts. For example, to harden steel spur gear initial quenched and tempered martensite microstructure is recommended for having desirable final properties. It provides a hard metastable phase in hardening case and sufficient toughness in the core of the component.

Despite all advantages of using this initial microstructure, the component is affected just below the transformed zone due to high temperature exposure, by a process called tempering. The meta-stable quenched and tempered martensite softens by turning into more stable phase with lower hardness in the so-called over-tempered zone (Ducassy 2010). In this area the formed carbides coarsen in very short time by high heat exposure of induction process. This coarsening stage is mainly responsible for the loss of hardness in this area. The recovery of the dislocation substructure and ferrite grain growth may play secondary roles on hardness loss.

In order to understand and predict the kinetic of transformation, a fundamental study is conducted to investigate the coarsening kinetics of cementite. Then the microstructural features could be predicted by using elaborate models and hardness may be estimated in the

over-tempered zone area. The chapter one reviews the literature existing on the subject. Then the chapter two describes the context of the study.

The aforementioned goal was achieved by characterizing representative samples of over-tempered zone, tempered at isothermal high temperature condition and different times, which is described in chapter three. In chapter four, the investigation of carbides by different methods revealed the average precipitate size, volume fraction, morphology, chemical composition, roundness, as well as quantities derived from former measurements such as inter-particle spacing, volume number density, and coarsening rate.

The results showed gradual increase of mean equivalent cementite size, supersaturation of carbides by substitutional alloying elements Cr, Mn, and reduction of their number density during isothermal tempering. A mathematical method was used to calculate volume size distributions of precipitates in order to compare with the corresponding LSW distribution function. The LSW distribution complies with the experimental distributions only for the average size, although a low fraction of large precipitates overpass this limit.

In addition, a complementary study is performed by Thermo-Calc and DICTRA software packages in chapter five to model the coarsening of precipitates in hardness loss area. Experimental and calculated radius of precipitates is compared. The chemical composition of precipitates determined by experiment and model shows that Cr, Mn, and Mo partitioned into cementite, Cr and Mn at the early stage of tempering, and Mo at the longer stage of tempering. These elements influence coarsening resistance of cementite particles. The non-partitioning alloying elements Ni and Si accumulated in matrix, and play role on coarsening resistance at later stage of tempering. These results are good evidence for explaining the remarkable resistance of AISI 4340 steel under thermal treatment. In addition due to low

temperature 653 K (380 °C) selected for initial tempering to reach 460 HV only carbon can diffuse to reach thermodynamics stability, and any further high temperature exposure (over-tempering) will require a new set of thermodynamic condition to be reach, preventing rapid cementite growth. Moreover, the kinetics coarsening of cementite and ferrite grain growth are modeled by extension of Björklund model. It takes into account the effective diffusion coefficient by considering grain boundary as fast diffusion path. Using existing strength models one could estimate hardness of the tempered samples. Based on Holloman-Jaffe equation that uses the concept of time-temperature equivalence, the former results of isothermal tempering could explain the non-isothermal condition of tempering occurring during induction hardening process in over-tempered zone.

This manuscript ends with a conclusion followed by recommendations and appendixes.

CHAPTER 1

LITERATURE REVIEW

1.1 Introduction

Understanding the phenomena that happen during fast tempering of AISI 4340 steel is the main concern of this study. Induction hardening, as a most favourable surface hardening process of steel, is frequently used for cylindrical and gear components (Rudnev 2005). The other goal of this chapter is to know the effective parameters of induction treatment influence on final properties of components. Furthermore, this chapter will introduce a method for predicting the hardness in over-tempered area, based on the thermodynamics and kinetics laws.

1.2 Induction hardening

Induction heating is one of the most popular localized heating processes (Yang, Hattiangadi et al. 2010). It provides clean, accurate, and internal heating of an object. Its complexity makes it somewhat hard to control compared to other surface hardening process such as cementation.

It works based on the principal of electromagnetic law discovered by Michael Faraday in 1831. During this process, a metallic bar is placed in the coil through which high frequency current passed by as illustrated in Figure 1-1. This figure shows how magnetic field created by high-frequency alternating current passing through an inductor, usually made of water-cooled copper, could induce eddy current in a metallic bar.

The induced eddy currents generated adequate heat for heat treatment process. The heat can be calculated according to the $H=RI^2$ equation, where (R) is the electrical resistance and (I) is the electric current. Fast change in the internal magnetization domain direction produces considerable heat up to steel Curie temperature around 768 °C (Krauss 2005).

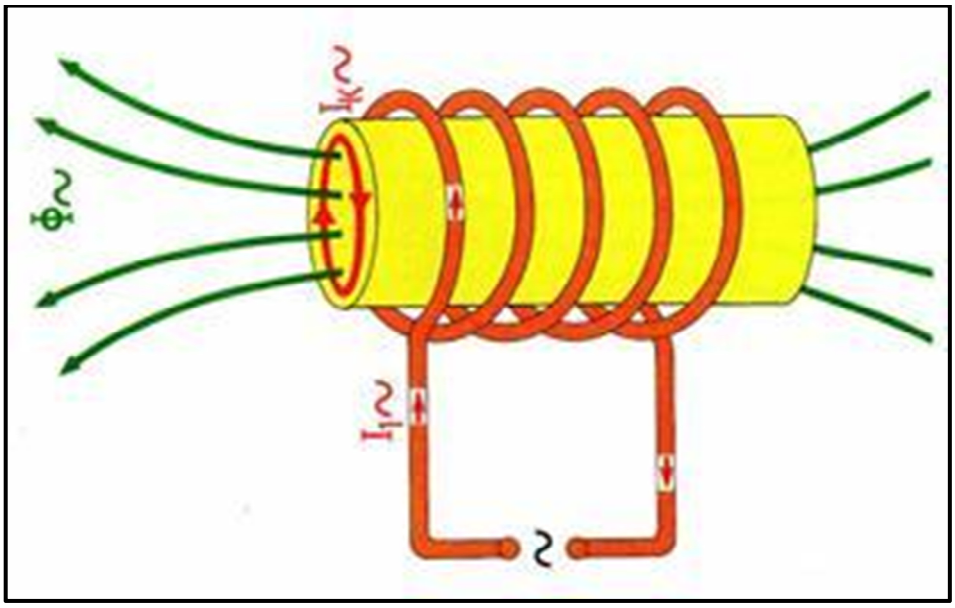

Figure 1-1 Principle of induction hardening
(http://www.saetgroup.com).

Induction heating process is performed by the interrelation of electromagnetism, heat transfer, and metallurgy; therefore, it is strongly influenced by parameters such as operating frequency, time of holding, electrical power, workpiece, coil number of turns and geometry (Rudnev, Loveless et al. 2003).

Desirable component properties for hard surface layer and tough core are achieved by adjusting these parameters appropriately. As an example, high frequency and high power density, in combination with short heating time, are required to harden the tooth's tips of gears, whereas low frequency is necessary for hardening the tooth's roots of gears. Figure 1-2 shows the schematic frequency effect on a gear component during case hardening treatment.

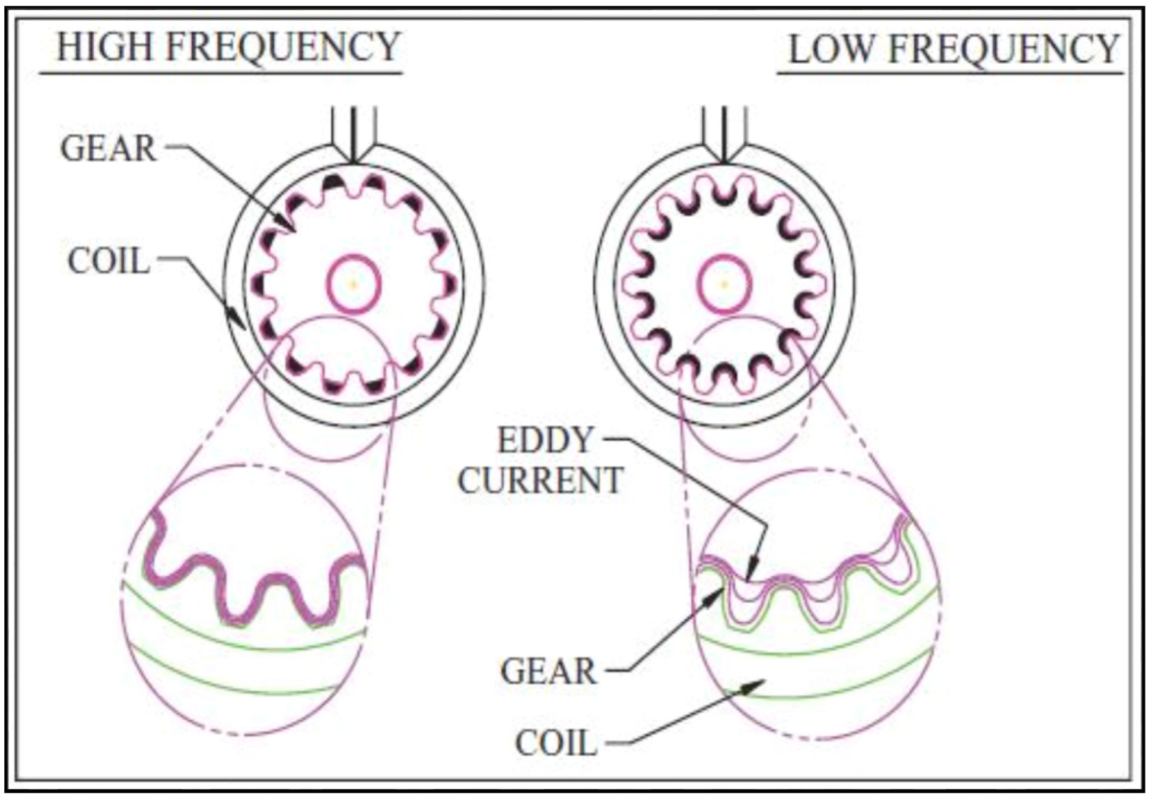

Figure 1-2 Illustration of frequency influence on eddy current flow within the gear when using an encircling inductor (Rudnev 2008).

1.3 Mechanical properties after induction hardening

High wear resistance accompanied with tough core increase fatigue property of steel component. Induction hardening surface treatment is frequently applied on tempered low alloyed medium carbon steels to provide desirable mechanical property especially for aerospace application when fatigue resistance is demanded.

During the thermal treatment the steel must be heat up at austenizing temperature and quenched by high cooling rate to form martensite and to avoid from any decomposition of austenite to other products such as ferrite, pearlite, and bainite (Bhadeshia and Honeycombe 2006).

Full hardened section is not always desirable for machine parts when combination of hard wear resistant surface with a tough core is required (Bhadeshia and Honeycombe 2006). Surface hardening is preferred compared to complete ones, because the core creates a tensile internal stress while the surface is under compressive stress. Fulfilling both requirement achieve by surface treatment such as induction hardening. It avoids any fatigue cracks nucleated at surface propagate easily in presence of compressive residual stress, as well as resist tensile bending fatigue (Rudnev, Loveless et al. 2003).

1.4 Metallurgical aspect of induction hardening

Induction hardening involves heating through or on surface or at selected areas of the component to austenitizing temperature, holding at this temperature to have complete austenite transformation (homogenization) and then, quenching very fast to form martensite microstructure. During this process, austenite transforms to martensite and any phase transformation known as self-tempering to phases with lower hardness should be controlled (Valery and Rudnev 2007).

Critical factors like the prior microstructure, the composition, and the heating rate, etc affect the resulting microstructures and the properties of components by changing case depth, maximum surface hardness, and minimum hardness found in the sublayer between the surface and core. In particular, they control the hardness profile found in the case-core transition zone, and improve compressive residual stresses (Clarke, Van Tyne et al. 2011).

1.4.1 Initial microstructure

The initial microstructure of steel has a pronounced effect on the final properties of heat treated parts under induction hardening process. As an illustration, Figure 1-3 displays the effect of annealed, normalized, quenched and tempered initial microstructures on hardness profile after surface hardening of AISI 1070 steel by using 450 kHz induction generator. These steels are operated at the same power density and time duration 2.5 kW/cm^2 (16 kW/in^2) (Speich and Leslie 1972, Rudnev 2005). The quenched and tempered initial

microstructure is the most desirable ones in aerospace industry. It helps to obtain suitable hardness pattern, deepest hardened case depth, and the shortest transition zone compare to other initial microstructure (Rudnev 2005). Despite all advantages of this initial microstructure, hardness loss in over-tempered zone between surface hardened layer and tough core is recognized as a weak area which is not desirable for fatigue life.

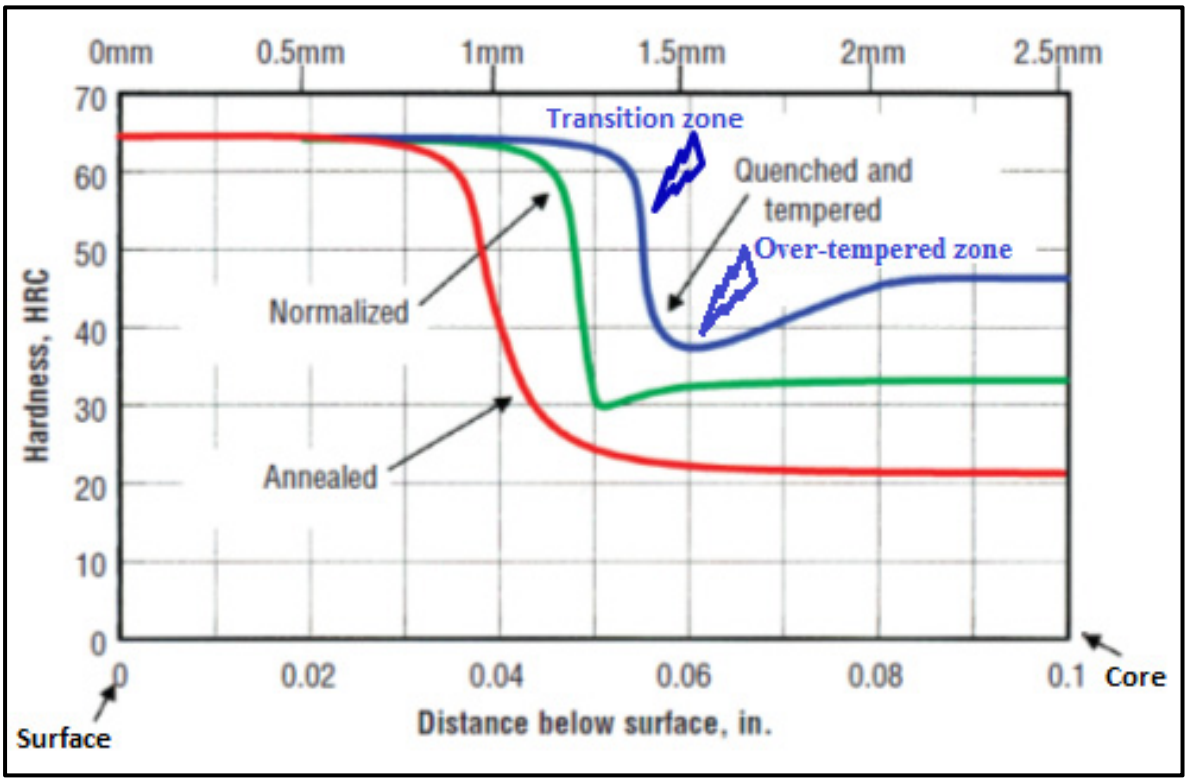

Figure 1-3 Effect of initial microstructure on surface hardening response for steel bars AISI type 1070 (Rudnev 2005).

1.4.2 **Composition**

The carbon content of steel influences effectively on the properties of components treated by induction hardening. It affects not only hardenability, (i.e., the process of forming martensite

during cooling) but also the transition zone, namely eutectoid steels has a shorter transition zone compared with a hypoeutectoid steel at the same condition of heating and quenching (Rudnev 2005).

In addition, substantial alloying elements such as chromium, manganese, molybdenum nickel, silicon, affect steel properties even in small amount. They are categorized based on their influence on the critical temperatures (i.e. A_1, A_3, A_{cm}), solubility in iron, kinetics of austenitic transformation upon cooling, ability to prevent grain growth (Rudnev, Loveless et al. 2003). They affect the tempering process, subsequent to quenching or during additional tempering. In fact, they retard considerably growth and coarsening of the cementite particles by partitioning in cementite or segregating in the interface of cementite and matrix (Chang and Smith 1984).

1.5 Phase transformation

The thermodynamics and kinetics laws could be used to simulate diffusional phase transformation in multicomponent alloy system. The concern would be how and how fast one or more phases in an alloy transform into a more stable phase. Then, the mechanical properties can be predicted by knowing the microstructural evolution described by cementite growth and coarsening in conjunction with Orowan theory.

1.5.1 Fe-C phase diagrams, TTT, and CCT

Phase diagram presents the interrelationships between the different phases, compositions, and temperatures of an alloy at equilibrium condition. Its application is a traditional and primary approach for binary or ternary alloy system to determine the stable phases during thermal treatment; however, in multicomponent alloy system its application has been limited significantly. As an example, the Iron-Carbon (Fe-C) phase diagram is used as a guideline for thermal treatments of steel alloys by taking into account that in any thermal treatment alloying elements changes the position of phase boundary. Figure 1-4 shows the equilibrium

phase diagram of Fe-C without the effects of alloying elements. This effect can be monitored by thermodynamic calculation with T-C software in multicomponent system (Krauss 2005).
In this diagram, cementite and ferrite are shown as stable phases in room temperature. They form from austenite under equilibrium condition. The variation in the lattice structure is followed by the allotriomorphic change, when austenite (fcc, γ) with face-centered cubic lattice structure transform to ferrite (bcc, α) with body-centered cubic lattice structure, and cementite (Fe_3C) orthorhombic crystal structure.
The transformation of austenite to martensite (bct) body centered tetragonal crystal structure by fast quenching and non-equilibrium condition could be monitored by adding time parameter to the equilibrium phase diagram. The temperature, time, and transformation (TTT) diagrams are used to show how fast the system transforms to equilibrium state at isothermal state of treatment. Figure 1-5 illustrates the TTT diagram of AISI 4340 steel. It shows the variation of product phases during fast austenite transformation at different times and temperatures. These kinds of diagrams are limited to isothermal treatment. To make a solution on this limitation, Continuous Cooling Transformation (CCT) phase diagram can be used to determine the progress of phase transformation during continuous cooling process by different cooling rate. Figure 1-6 present the (CCT) diagram for AISI 4340 steel.

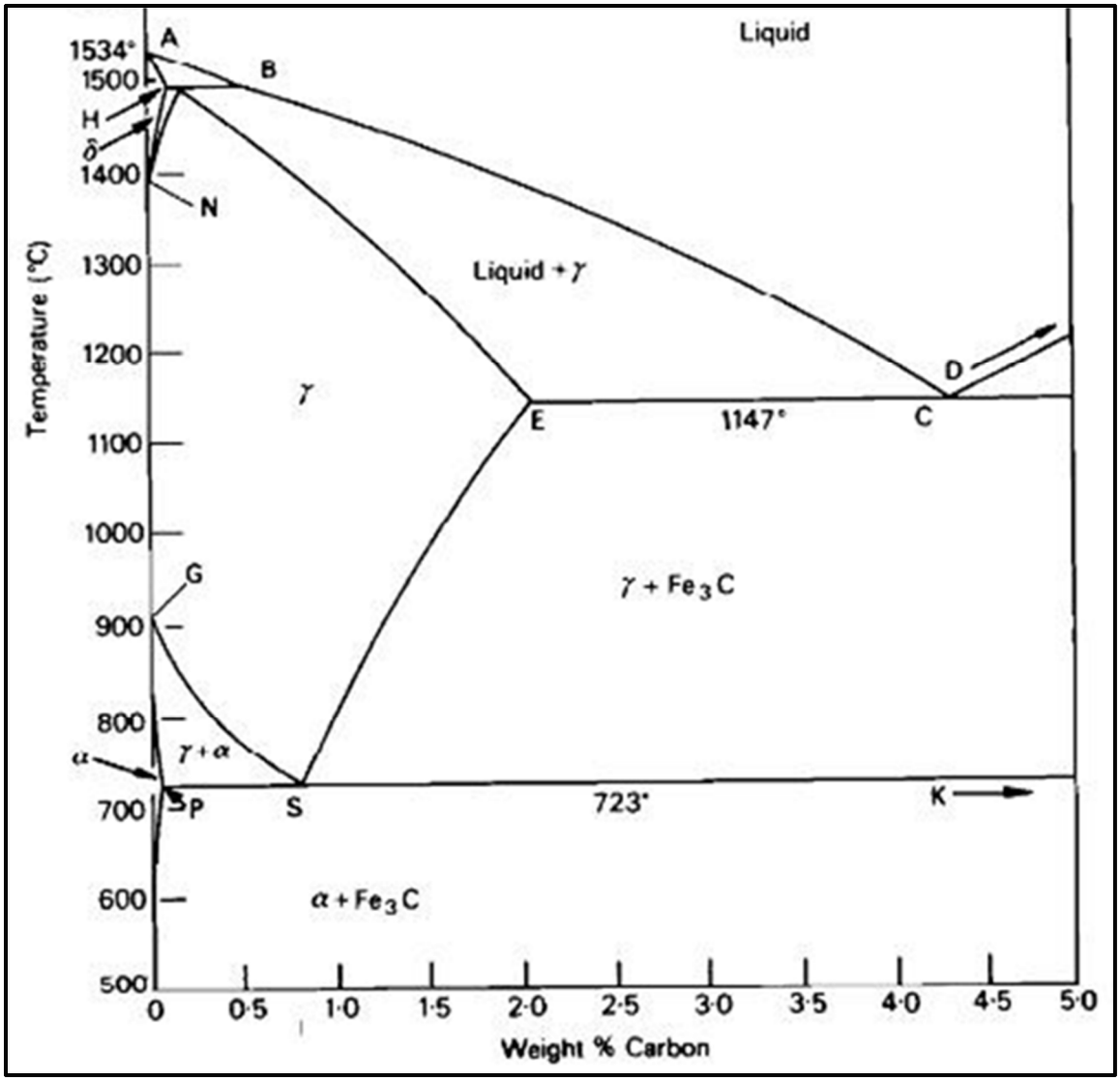

Figure 1-4 The equilibrium iron-carbon phase diagram
(Bhadeshia and Honeycombe 2006).

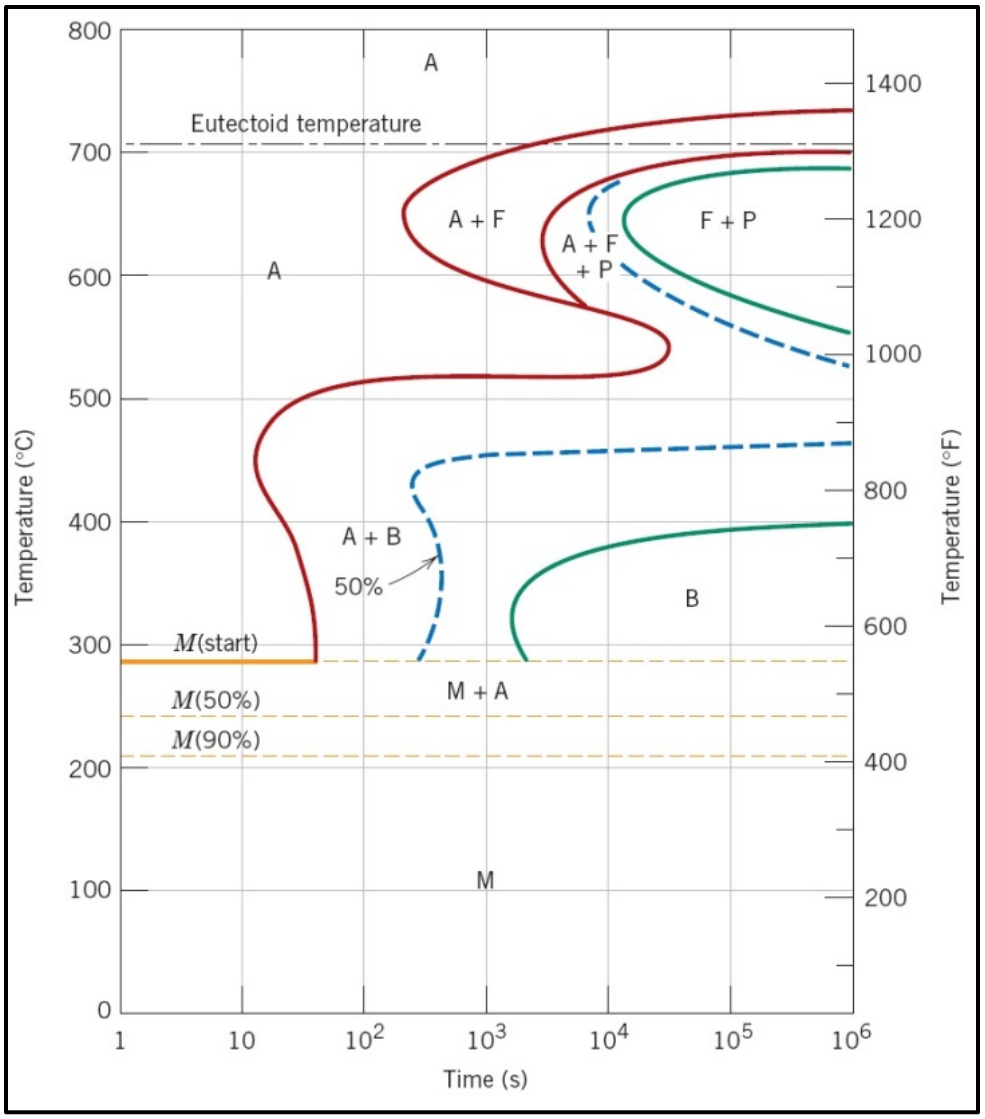

Figure 1-5 Isothermal transformation diagram for an alloy steel (type 4340): A, austenite; B, bainite; P, pearlite; M, martensite; F, proeutectoid ferrite (ASM 1977).

1.5.2 **Gibbs free energy**

Prediction of any phase transformation like precipitation requires to take into account the Gibbs free energy in a multicomponent and multiphase system. Phase transformation does

not go directly to the stable state but can pass through a whole series of metastable states. This transformation can be described by the concept of driving force and activation energy.

Figure 1-7 illustrates a phase transformation from metastable state (here tempered martensite) to a more stable state (ferrite with dispersed carbides). If G_1 is the free energy of initial state and G_F is the free energy of final state, the driving force for transformation will be $\Delta G = G_F - G_1$. Activation free energy ΔG_A more than G_1 is required to pass through from state 1 to final state condition (Porter and Easterling 1992).

The decrease of interfacial area and thus energy produces driving force for precipitation coarsening, spheroidization, and grain growth (Martin, Doherty et al. 1997). It is usually considered insignificant in phase transformation, however in case of coarsening it should be taken into consideration (Perez 2005). The surface free energy change due to radius of curvature is so called Gibbs-Thomson effect. The solubility limit of A atoms in α matrix in equilibrium with θ particle cementite for equilibrium spherical shape particles of radius r can be given by the Gibbs-Thomson equation (1.1):

$$X^{\alpha}_{eq_r} = X^{\alpha}_{eq_\infty} exp(\frac{2\sigma V_m}{rRT}) \quad (1.1)$$

where $X^{\alpha}_{eq_\infty}$ is solubility limits when interface is flat, T is the temperature, V_m is the molar volume, R the molar gas constant, and σ is the interfacial energy (Perez 2005). The interfacial energy per unit area between particle cementite and matrix ferrite has a vital role during cementite coarsening process. These values in steel are reported in Table 1-1. They are defined by data fitting procedures with experimental growth rate (Pandit 2011).

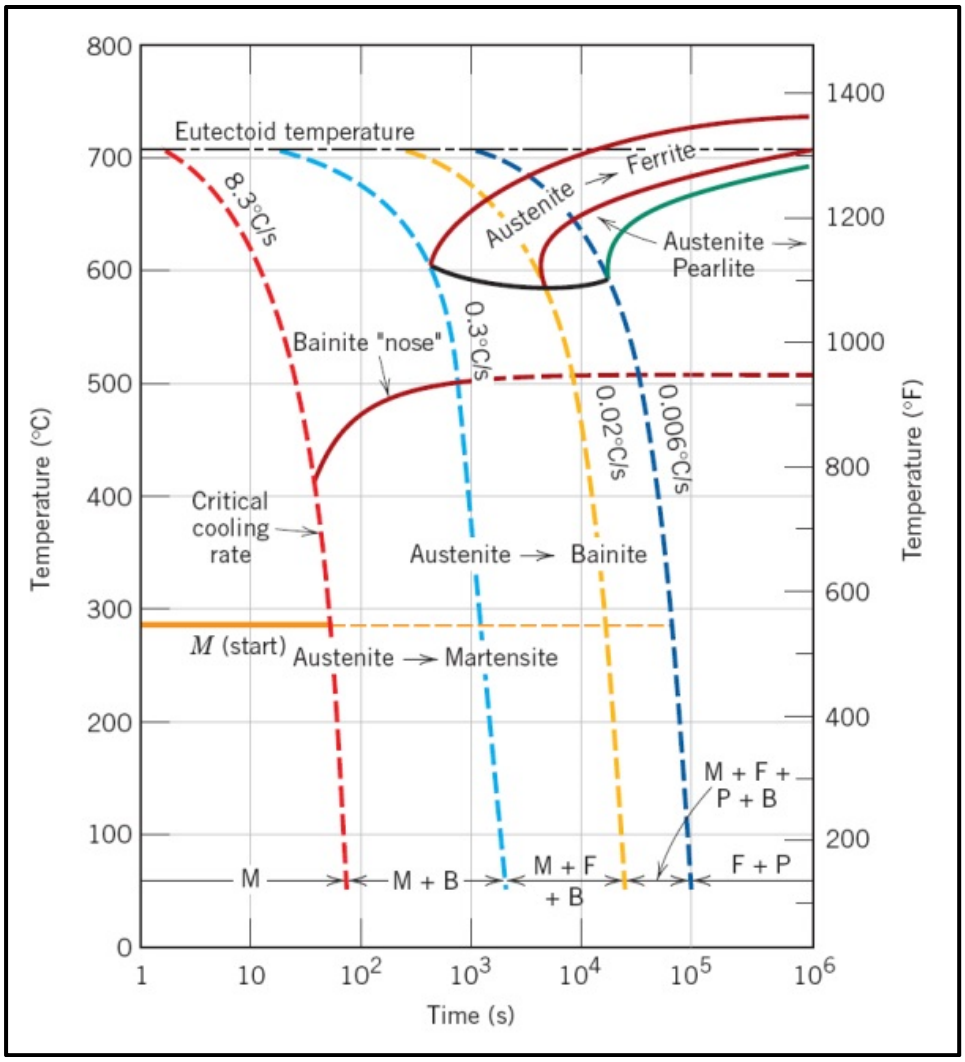

Figure 1-6 Continuous Cooling transformation diagram for an alloy steel (type 4340) and several superimposed cooling curves demonstrating dependence of the final microstructure of this alloy on the transformations that occur during cooling (Lankford, Samways et al. 1985).

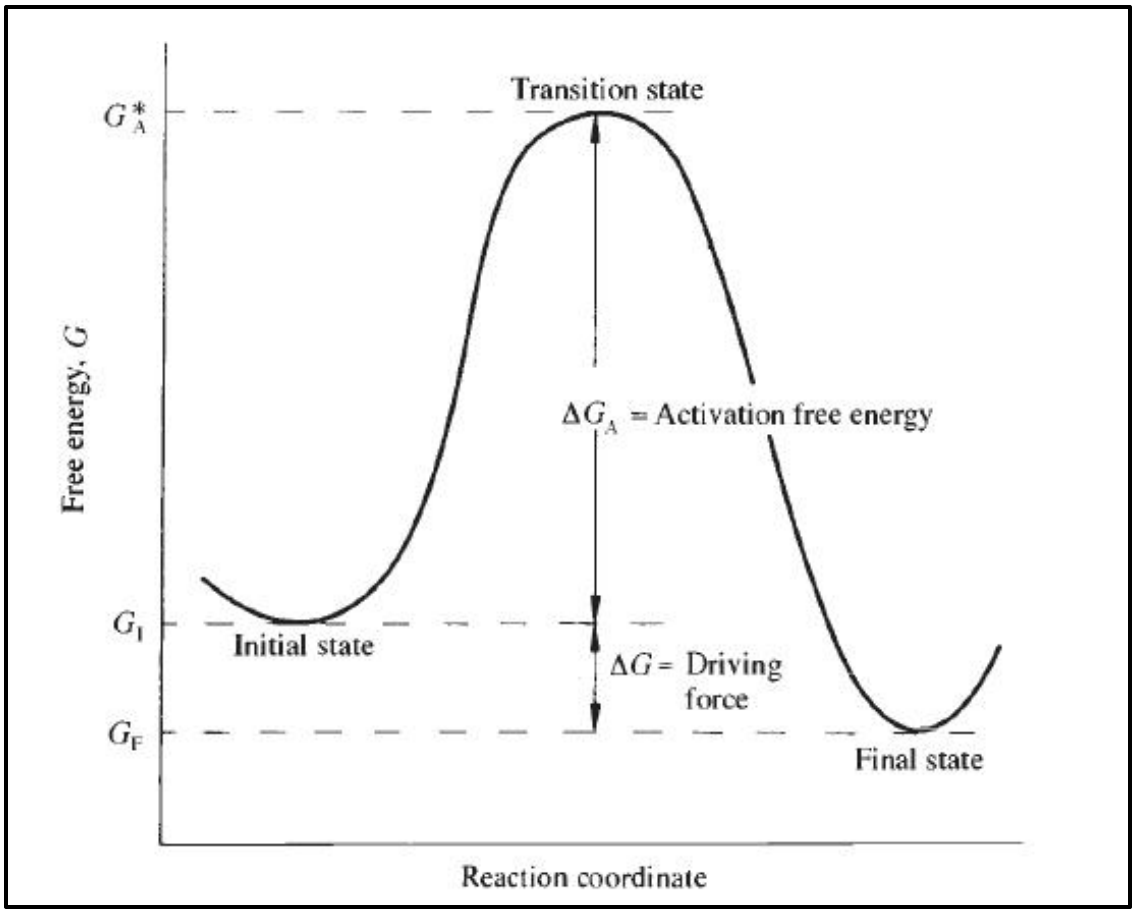

Figure 1-7 Illustration of a phase transformation from metastable to stable state (Martin, Doherty et al. 1997).

Table 1-1 The ferrite-cementite interfacial energy per unit area value published by previous research (Pandit 2011).

Temperature, K (°C)	Method	σ (Jm^{-2})
861 (588)	Coarsening rate and data fitting	0.56
903-963 (630-690)	Coarsening rate and data fitting	0.417−0.248
1000 (727)	Interfacial enthalpy measuring	0.7±0.3

1.6 Quenched & tempered martensite

The process of heating hard martensite and cooling to elevated temperature is called tempering. It is usually used to supply ductility enhancing toughness to this phase. Several reactions would occur during the tempering of martensitic steels. These reactions involve the segregation of carbon, precipitation of carbides, decomposition of retained austenite, the recovery (eventually recrystallization) of the martensitic structure. The rate of each stage depends on several parameters such as percentage of carbon, alloying elements, temperature of tempering, and duration of treatment (Bhadeshia and Honeycombe 2006) (Speich and Leslie 1972). Figure 1-8 shows the schematic illustration of the phenomena occurring in carbon steels during one hour tempering at various temperatures (Speich and Leslie 1972). The hardness variation of fresh martensite with different percentage of carbon show different trend from 100 °C to 700 °C in this diagram.

1.6.1 Carbon segregation

At low temperature carbon segregation takes place. During this process, carbon atoms redistributed to certain interstitial lattice sites around individual dislocation and cell walls in lath martensite. Because some of these places are preferred sites for carbon segregation rather than normal interstitial lattice positions (Speich and Leslie 1972).

This stage could be detected by monitoring the change in electrical resistivity or internal friction when carbon is at a given interstitial site or segregates to dislocations during quenching. It is reported when carbon is below 0.2 wt%, almost 90% of it segregated to lattice defect during quenching; however, such places are saturated in steel with carbon above 0.2 wt%, therefore carbon is kept in defect free lattice (Speich and Leslie 1972).

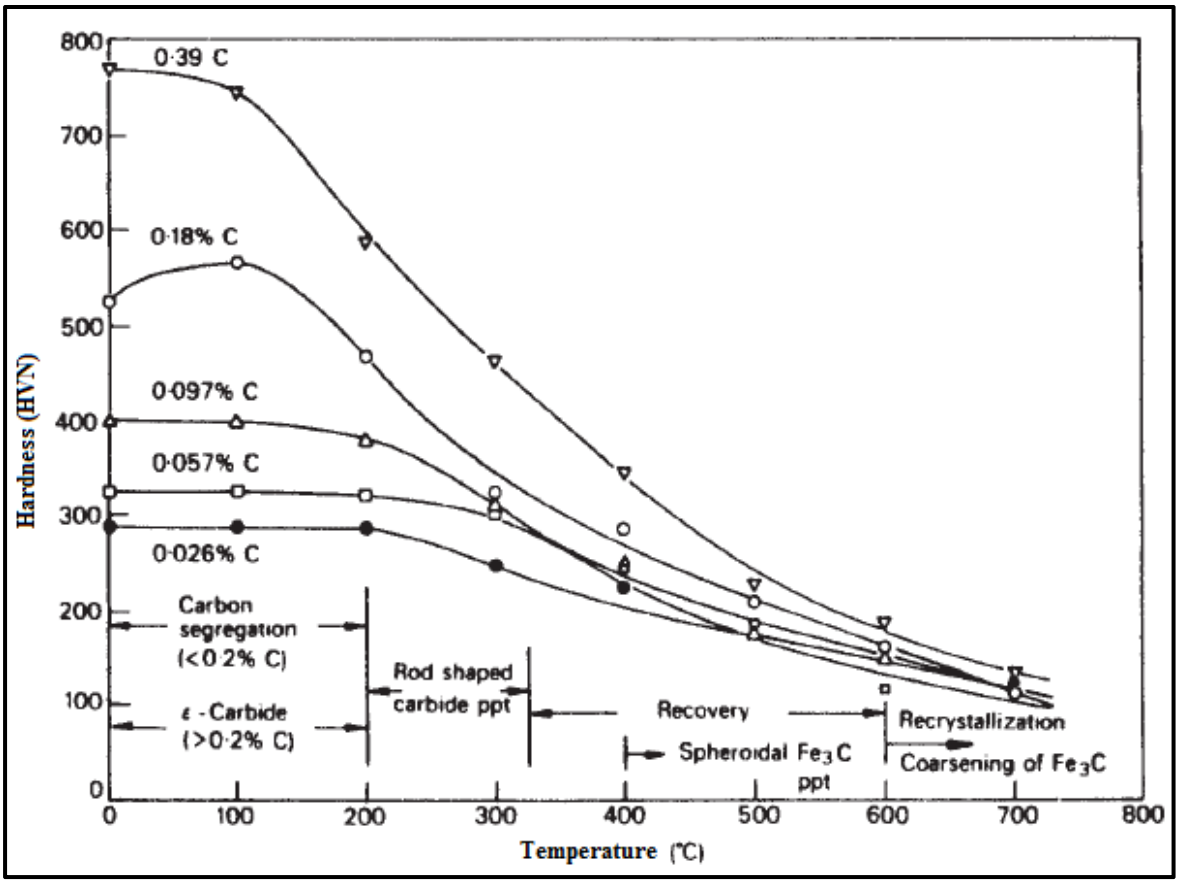

Figure 1-8 Hardness variation versus temperature for different iron-carbon martensite tempered 1 h at 100 – 700 °C (Bhadeshia and Honeycombe 2006).

1.6.2 **Carbide precipitation**

The first carbide precipitated at temperature between 100 °C to 200 °C in steel containing more than 0.2 wt% carbon is ε-carbide ($Fe_{2.3}C$). In low-alloyed steels containing less than 0.2 wt% carbon, precipitation of ε-carbide ($Fe_{2.3}C$) is inhibited in this range of temperature because segregated carbon in defects like dislocations has less driving force to precipitate.

As the carbon content increase to 0.4 wt% carbide precipitation takes place very fast even at 150 °C. Formation of Hägg carbide (Fe_5C_2, monoclinic) occurs in some high-carbon steels tempered at 200 °C to 300 °C. Then, cementite formation (Fe_3C, orthorhombic) happens between 250 °C to 700 °C. The first morphology of tempered martensite is needle-like during

cementite precipitation. The martensite lath boundaries are the nucleation sites at low temperature, whereas ferrite grain boundaries are nucleation sites at higher temperature.
At the end, Fe_3C spheroids forms in a defect free α-iron matrix when tempering temperature increases to 700 °C (Speich and Leslie 1972).

1.6.3 **Decomposition of retained austenite**

Retained austenite is decomposed to ferrite and cementite during tempering at tempering temperatures between 200 °C to 300 °C (Krauss 2005). It is sometimes called the second stage of the tempering process. An appreciable content of retained austenite remained in steel with equal or more than 0.4 wt% carbon, therefore this reaction is important for medium or high carbon steel (Speich and Leslie 1972). Removal of retained austenite is possible using cryogenic treatment by complete transformation from austenite to martensite (Zhirafar, Rezaeian et al. 2007).

1.6.4 **Recovery and recrystallization**

Recovery happens above 400 °C, when cell boundaries and the random dislocations tangles present in the martensite structure annihilated very fast.
Recrystallization occurs during tempering process in low carbon steels between 600 °C to 700 °C, when aligned lath morphology transform gradually to equi-axed ferrite matrix (Caron and Krauss 1972) (Speich and Leslie 1972).

1.6.5 **Spheroidization**

For high enough temperature and for time enough tempering, cementite precipitates transform to more stable spheroidized shape, this process being called spheroidization. This provides the most stable structure in steel. The strength of material reduces by the increase in the ductility of microstructure associated with spherical carbide precipitates.

The driving force for spheroidization is the reduction of carbide/matrix surface free energy as the minimum surface to volume ratios existed for spherical particle compare to other particles shape (Krauss 2005).

1.6.6 **Coarsening or Ostwald ripening**

Coarsening as a later stage of tempering process takes place at temperature started between 300 °C and 400 °C. During this process, precipitates cementite lose their crystallography morphology and spheroidized increasingly up to 700 °C (Bhadeshia and Honeycombe 2006). Then, small particles dissolve and large ones grow due to Gibbs-Thomson effect. This process is well known as Ostwald ripening, which was first discovered by the chemist W. Ostwald (Ratke and Beckermann 2001) (Porter and Easterling 1992).

In a binary system, two spherical particles with different size of r_1 and r_2, the solute concentrations for precipitates are equal with equilibrium Gibbs-Thomson value, when volume diffusion controls the rate of process. Due to larger particles with higher radius of curvature has less molar free energy comparing to smaller particles, a diffusive flux of atoms could be found from particles with smaller radius of curvature r_1 to particles with greater radius of curvature r_2 as illustrated in Figure 1-9 (a). This flux makes smaller particles disappear in expense of larger particles (Martin, Doherty et al. 1997). Figure 1-9 (b) is presented the effect of curvature radius on molar free energy.

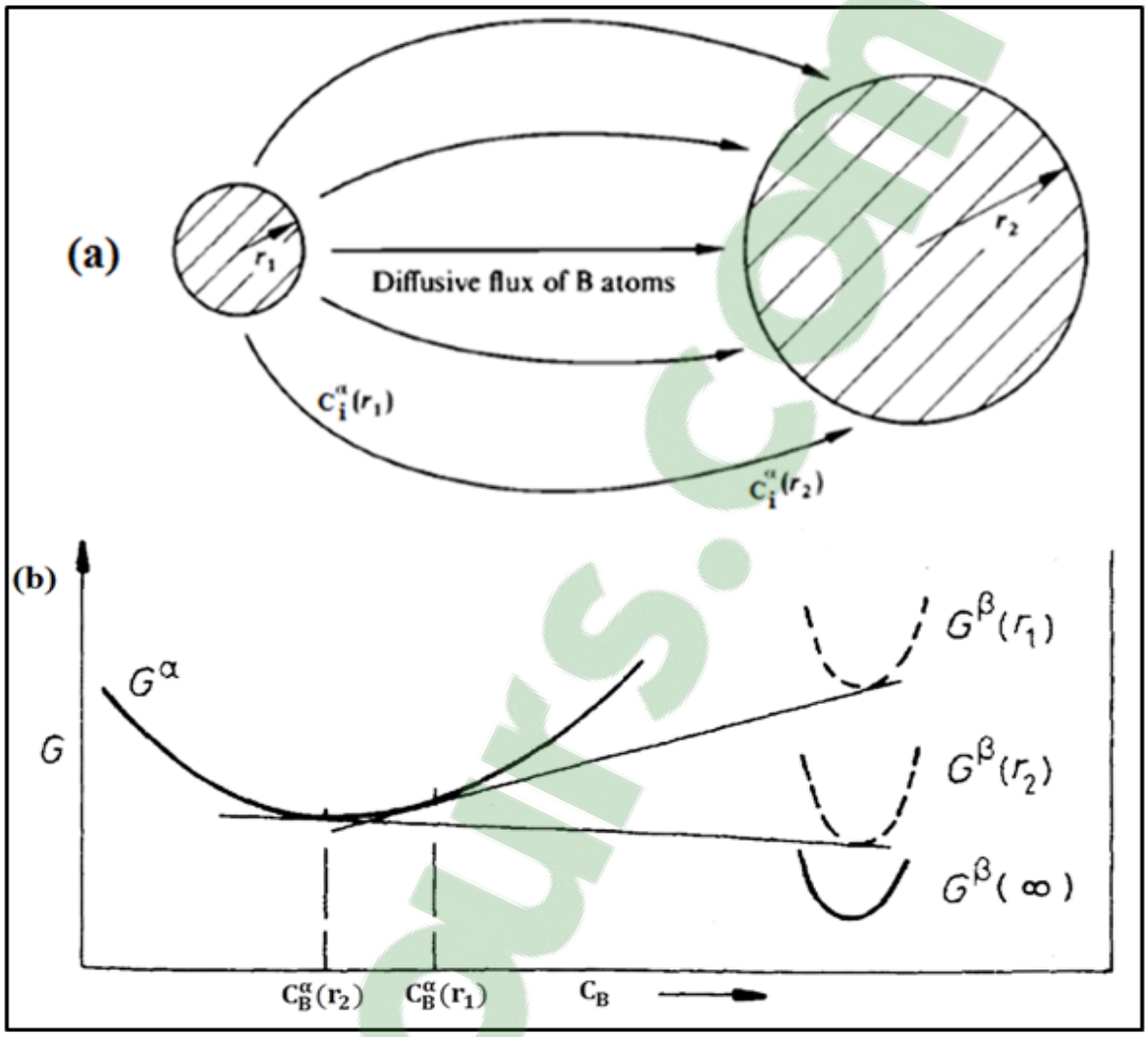

Figure 1-9 The origin of particle coarsening. a) illustration of two spherical precipitates β of small radius of curvature r_1 and large radius of curvature r_2 in matrix α diffusive flux from 1 to 2, where $C_i^{\alpha}(r_1) > C_i^{\alpha}(r_2)$ b) small particles β has higher molar free energy andless stability comparing to large particles (Martin, Doherty et al. 1997) (Porter and Easterling 1992).

Coarsening makes undesirable loss of strength and grain boundary pinning effects. The concentration of solute in the matrix around the spherical precipitates will increase following by decreasing the radius of curvature. In addition, the size and number of small particles reduce to feed large particles growth, therefore the mean particle radius $\bar{r}$ increases with time

according to coarsening relations equations (1.2) and (1.3) (Nishizawa 2008) (Porter and Easterling 1992).

$$\bar{r}^3 - \bar{r}_0^3 = K.t \quad (1.2)$$

$$K \propto D\sigma X_e \quad (1.3)$$

where r_0 is the mean radius at time t=0, D is the diffusion coefficient, σ is the interfacial energy, and X_e is the equilibrium solubility of very large particle, and $\bar{r}$ is the mean particle radius.

At moderate temperature, cementite coarsening occurs very fast due to the high diffusivity of interstitial carbon. However, slower diffusion rate of substitutional alloying elements which segregates to carbide can slow down the rate of coarsening (Porter and Easterling 1992).

During coarsening or Ostwald ripening, there is a critical size r_c, where the smaller particles shrink and disappear and the larger particles grow at their expense. The rate of shrinking and growing is controlled by alloy diffusion, which is much lower than the rate of carbon diffusion (Björklund, Donaghey et al. 1972).

1.6.7 **Effect of alloying elements addition on coarsening**

The coarsening of cementite particles are retarded by addition of third alloying elements (Cr, Mn, Mo, Ni, Si,…) to martensite steel in binary Fe-C system (Lv, Sun et al. 2008) (Zhu, Xiong et al. 2007). The mechanisms retard coarsening and softening influence by time and temperature of tempering. For example, at low temperature of tempering, Mn does not substantially partition in cementite, therefore it makes small effect on softening. However at high temperature of tempering, it affects substantially on resistance coarsening due to large amount of partitioning into cementite (Lv, Sun et al. 2008) (Krauss 2005).

Zhu et.al is reported no partitioning of alloying elements in 4340 steel at 300 °C and 350 °C for 1 hr. At 400 °C for 1 hr, Si, due to higher diffusivity, than other alloying elements is detected in the matrix. At 400 °C and longer time of tempering, carbide forming alloying elements Cr and Mn are partitioned into cementite, and Ni and Si non carbide forming

alloying element are rejected from cementite and distributed in the matrix. At this stage of tempering as distribution of sluggish alloying elements controls the cementite coarsening, the coarsening rate is reduced comparing to binary steel Fe-0.4C (Zhu, Xiong et al. 2007).
The significant retarding effect of Si on softening is reported in many references due to its low solubility in the cementite. Therefore, Si enriched area in matrix around precipitates produces kinetics barrier to subsequence growth of particle cementite (Krauss 2005). The more insight theory about tempering procedures and the importance role of alloying elements in medium carbon steel could find in chapter 5.

1.7 Hardness prediction by Holloman-Jaffe equation

Prediction of the mechanical properties in quenched and tempered low alloyed medium carbon steel is desirable for industrial application. Some practical models are applicable to predict hardness as a function of temperature and time of tempering such as Holloman–Jaffe equation. The equivalent Holloman-Jaffe parameter (PT) appearing in equation (1.4) describes the linear hardness behavior equation (1.5) with tempering time at a given temperature, or with varying temperature.

$$PT(T,t) = T.(C + logt) \quad (1.4)$$

$$HV(T,t) = a + b.PT(T,t) \quad (1.5)$$

where T and t are temperature and time of tempering, and a, b are constant parameters, and C is material constant (Murphy and Woodhead 1972) (Ducassy, Bridier et al. 2009). However, the evolution of microstructure or the composition of the steel except for carbon diffusion is not taken into account with this model.

1.8 Hardness prediction by microstructural features

The evolution of hardness based on microstructural features is studied by many authors (Malik and Lund 1972) (Venugopalan and Kirkaldy.J.S 1978) (Wang, Appolaire et al. 2006) (Kim, Boucard et al. 2014). They involved different strengthening mechanism to predict

hardness by using parameters such as precipitate size, dislocation density, lath size, and grain boundary effect. These models are developed by calculating yield stress σ_y equation (1.6) of the tempered martensite in steel component under thermally heat treatment:

$$\sigma_y = \sigma_{Fe} + \sigma_C + \sigma_{SS} + \sigma_P + \sigma_\rho + \sigma_g \quad (1.6)$$

where σ_{Fe} is the threshold stress or the friction stress of pure iron (Peierls stress), σ_C is the solid solution hardening due to carbon atoms, σ_{SS} is the solid solution hardening due to substitutional alloying elements (such as Cr, Mn, Mo, Ni and Si in AISI 4340 steel), σ_P is due to dispersion hardening theory by incoherent disperse carbides that works with Orowan theory, σ_ρ is strain hardening due to dislocation density, and σ_g is hardening due to grain or subgrain boundaries based on the Hall-Petch effect (Kim, Boucard et al. 2014).

1.9 Strengthening mechanisms

The effect of different strengthening mechanisms on the yield strength of low carbon tempered martensitic steels can be described as follow:

1.9.1 Peierls-Nabarro strengthening

The required resolved shear stress to make dislocation glide in a non-perfect crystal structure without any thermal activation is nominated the Peierls (or Peierls–Nabarro) stress (Hull and Bacon 2011). There is dispersion for contribution of strength due to friction stress σ_{Fe} in literature from 13 MPa to 218 MPa probably due to the grain size effect, equation (1.7) studied by Wang is used to derive this value.

$$\sigma_{Fe} = 78 - 0.023 \times T \quad MPa \quad (1.7)$$

where T is the absolute temperature (Wang, Appolaire et al. 2006). It could be considered constant at room temperature.

1.9.2 **Solid solution strengthening**

The contribution of solid solution strengthening σ_C and σ_{SS} due to interstitial atom C and substitutional atoms (Cr, Mn, Mo, Ni, Si) have special importance in low alloyed medium carbon steel. Interstitial σ_C and substitutional σ_{ss} atoms, by interacting with moving dislocations, makes obstacle against any deformation, which is the reason of solid solution hardening (Malik 1972). These elements are called interstitial when their size is much smaller than matrix atom, and substitutional when their size are approximately similar. Depending to their size, they occupy vacancy or interstitial sites (or lattice points) of matrix atoms, respectively. This theory inferred that strength due to carbon interstitial atoms can be determined by the dissolved carbon content as presented in equation (1.8) and varys with square root of carbon concentration:

$$\sigma_C = KG\sqrt{X_C} \quad MPa \tag{1.8}$$

where strength is in MPa, K has been calculated from previous research as equal to 0.0167 (Wang, Appolaire et al. 2006), G is shear modulus, and X_C is the molar fraction of carbon in matrix.

As explained before, the role of alloying elements for contributing in strengthening mechanisms is important term during tempering procedure. By partitioning to cementite or accumulating in the interface, they prohibit from continuous growth and coarsening of precipitates. They contribute on strengthening of steel by a solid solution mechanism, which can be calculated by equation (1.9) and data in Table 1-2Table 1-2 (Wang 2006).

$$\Delta\sigma_{ss} = \sum x_i \Delta\sigma_{ss,i} \tag{1.9}$$

Table 1-2 Estimating solid solution strengthening contribution.

Solute	Cr	Mn	Ni	Si	Mo	C
$\Delta\sigma_s$(MPa/%wt) (1)	-30	32	33	83	11	5000
$\Delta\sigma_s$(MPa/%wt) (2)	60	80	45	60	-	5000

where x_i is weight percent of alloying elements, $\Delta\sigma_{ss,i}$ (MPa/%wt) (1) and (2) are the increased in strength per 1 wt% (weight percentage) of elements. These data are derived according to two different sources. No. (1) is used for this study.

1.9.3 **Precipitation hardening**

The contribution of precipitates on strength σ_P is different, depending to their coherency, semi-coherency, or incoherency with matrix. As an illustration, when the second phase has the same crystal structure and similar lattice parameters to the matrix, they are called coherent precipitate; in this condition dislocation should overcome the strain due to small particles in matrix by shearing mechanisms.

In contrary, when the second phases have different crystal structures compare to the matrix or random lattice orientation, they called non-coherent particles, and the active hardening mechanism is dispersion hardening by by-passing mechanism.

The interaction between precipitates and dislocations is then described by the most common Orowan theory, where dislocations by bending and bowing out between them under an applied shear stress makes an expanding loop around precipitates with λ inter-particle distance. Then, the loop around them makes an obstacle against the next moving dislocations. The schematic illustration of Orowan mechanism is presented in Figure 1-10. The strengthening effect due to the non-coherent particles can be described by equation (1.10):

$$\sigma_P = \frac{M\bar{F}}{\lambda b} \tag{1.10}$$

where M is the Taylor factor equal 2 to 3, and $\bar{F}$ is the average force required for dislocation to by-pass from the obstacles, λ is the inter-particle spacing that at later stages of tempering would be the order of 100b and b is the burgers vector equal to 0.248 nm in ferrite with 0.286 nm as lattice parameters and $\frac{1}{2}a < 111 >$ as burgers vector.

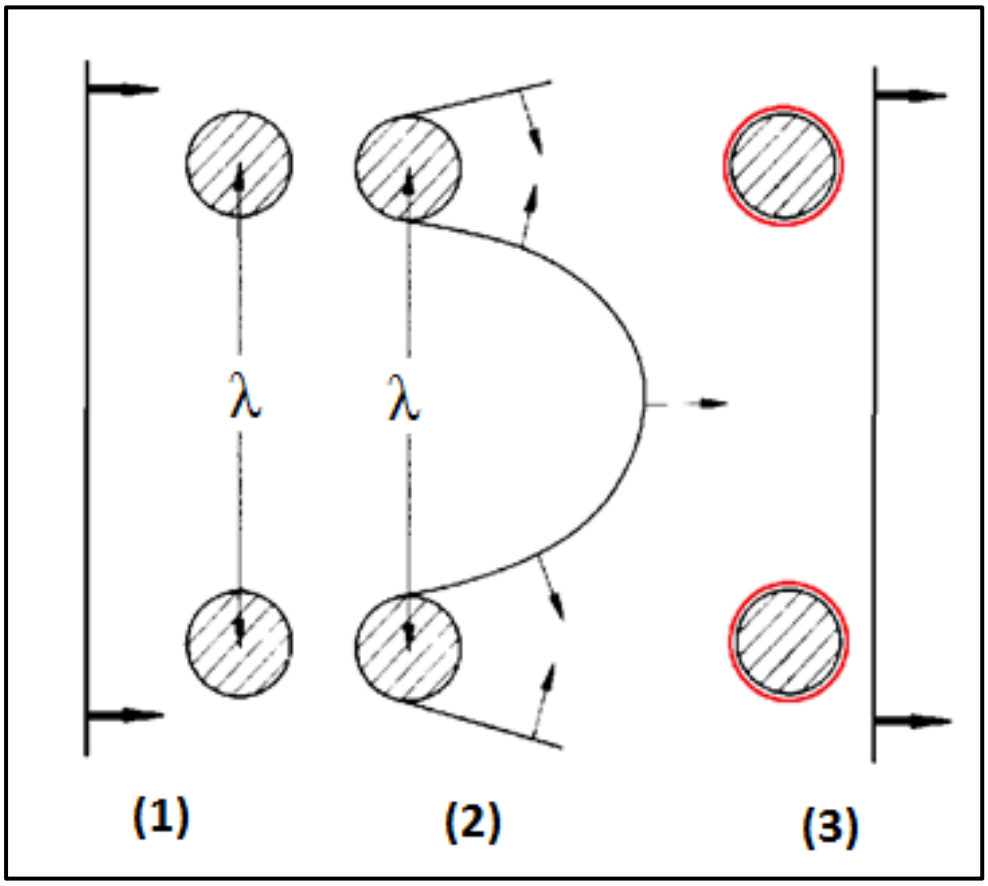

Figure 1-10 The schematic of Orowan mechanism for large precipitates (1), bowing between particles (2), by-passing particles and leaving a dislocationloop surrounding each precipitates (3)
(Martin, Doherty et al. 1997)

During long time tempering, any increase in inter-particle spacing will decrease the strength of the tempered alloy by a process called over-ageing. The formation of more stable

precipitates with wider inter-particle spacing, and the coarsening of precipitates as a reason of interfacial energy between precipitates and matrix are two significant reasons of over ageing (Martin, Doherty et al. 1997).

The interaction of dislocation with particles contributes on hardening mechanism. It could describe by shear and by-passing mechanisms. The strengthening by shear is represented by equation (1.11):

$$\sigma_P = K_1\sqrt{\bar{r}\,V_f} \qquad and \qquad K_1 = 0.02\,MG/\sqrt{b}\ MPa \tag{1.11}$$

where V_f is the volume fraction of precipitates, $\bar{r}$ is the precipitate mean radius that could be calculated by the microstructural model. M is the Taylor factor and b the burgers vector and G the shear modulus. The strengthening by by-passing is represented as below by equation (1.12):

$$\sigma_P = K_2\sqrt{V_f}/\bar{r} \qquad and \qquad K_2 = 0.6\,MGb\,MPa \tag{1.12}$$

Critical radius equal 10b is a transition size for precipitation hardening from shear to by-passing mechanism (Wang, Appolaire et al. 2006).

The other study by Kim et.al estimated the contribution of particle due to by-passing mechanism with Ashby-Orowan theory as equation (1.13):

$$\sigma_P = \left(\frac{0.538Gb\sqrt{V_f}}{X}\right) ln\left(\frac{X}{2b}\right) \quad MPa \tag{1.13}$$

where G is the shear modulus equal 80 GPa for cubic ferrite, b is burgers vector in ferrite, V_f is volume fraction of precipitates, and $X=2\times\bar{r}$ is the diameter of particle in (nm) (Kim, Boucard et al. 2014).

1.9.4 **Strain hardening**

The strengthening contribution due to interaction of moving dislocations with dislocations present in the system is called strain hardening. It has a pronounced effect on hardening mechanism as described by equation (1.14).

$$\sigma_\rho = M\alpha Gb\sqrt{\rho} \tag{1.14}$$

where M is Taylor factor equal 2 to 3, ρ is the dislocation density, G is the shear modulus, b is burgers vector, and α is a material constant depending on temperature and strain rate and equal to 0.38 for steel (Bhadeshia and Honeycombe 2006).

The dislocation density reduces during tempering process due to recovery of microstructure, which has a significant effect on strength. It could be measured by TEM microscope technique as a local method, or XRD analysis technique as global method (Cong and Murata 2011). The latter has been privileged to determine the disperse dislocation density in tempered martensite structures.

1.9.4.1 Dislocation density

In order to measure the dislocation density, a thorough study based on TEM method was done by Morito.et.al. They found a linear relation between overall carbon content and dislocation density as equation (1.15):

$$\rho \times 10^{-15} = 0.7 + 3.5wt\%C \tag{1.15}$$

Based on the chemical composition of 4340 AISI steel and martensite transformation, this quantity is equal 2.1×10^{15} m^{-2}. However, throughout tempering process, recovery is accompanied with tempered martensite. Therefore, the evolution of the dislocation density should be estimated in our calculations by considering equation (1.16):

$$\frac{d\rho}{dt} = -C \times exp(-Q/R\,T) \times \rho \tag{1.16}$$

where C is a constant, Q is the activation energy for moving dislocation equal to (134 $KJmol^{-1}$), due to iron atoms diffusion along dislocation, R is the universal gas constant, and T is the absolute temperature, and t the tempering time (Wang, Appolaire et al. 2006). Thereafter, by integrating from this relation, the following equation (1.17) defines dislocation density during tempering process.

$$\rho = exp(-C_1 \times exp(-Q/R\,T)\,t + C_2) \tag{1.17}$$

where C_1 and C_2 are constant, that can be derived from literature as equal to 2.1×10^4 and 36.84 respectively (Wang 2006).

1.9.5 **Hardening due to grain or subgrain boundaries**

The other contributions in strengthening mechanism are grain or subgrain boundaries. They influence on yield strength by making stress for dislocation to by-passing from them by the effect of Orowan theory. (Kim, Boucard et al. 2014).

In addition, the Hall-Petch relationship has shown the contribution of grain or subgrain boundaries on strength properties in tempered martensite steel by the equations (1.18) and (1.19):

$$\sigma_g = k_g l^{\frac{-1}{2}} \tag{1.18}$$

$$\sigma_g = k_t t^{\frac{-1}{2}} \tag{1.19}$$

where k_g is a constant related to material property ranging from 0.45 $MNm^{-3/2}$ to 1 $MNm^{-3/2}$ values, and k_t is a constant ranging from 0.3 $MNm^{-3/2}$ to 0.45 $MNm^{-3/2}$ values as derived from different literatures, and l and t are grain size and subgrain size respectively.

There are different approaches to elucidate these terms precisely including a plasticity model based on irreversible thermodynamics, misorientation angle characterization by electron backscattered diffraction, and transmission electron microscopy analysis (Kim, Boucard et al. 2014).

1.10 Summary

In summary, induction hardening as a popular surface hardening treatment is introduced. It is recognized that due to the high-heat exposure, transformation towards equilibrium state of martensite in sublayer (loss of hardness) area happens by coarsening and spheroidization of precipitates and recovery and recrystallization of the matrix. Furthermore, the principal of hardness calculation theory based on microstructural features are discussed in this section. It is understood that the multiple physical processes occurring during tempering influence on final property.

CHAPTER 2

CONTEXT OF RESEARCH

2.1 Introduction

Overall study about the research problem during fast tempering is explained in previous chapter. In this chapter, this problem explains specifically.

2.2 Research context of problematic

The initial microstructure used in gear components influences greatly austenitization during induction hardening treatments. As a matter of fact, a quenched and tempered initial microstructure helps to obtain higher hardness and larger hardened case depth compare to other initial microstructures (Rudnev 2005).

Although the quenched and tempered initial microstructure has the aforementioned advantages on induction hardened parts, these parts often show an area of reduced hardness situated between the hardened surface layer and the tough core. In this region, called over-tempered zone the heat exposure was not high enough to transform martensite and carbides into austenite but high enough to cause further tempering of the martensite; that reduces the local hardness. As an illustration, Figure 2-1 exhibits a hardness profile measured after induction hardening at the cross section of an AISI 4340 gear from the tip to the root. It shows different structural zones at the edge of the gear, Z_1 is the hardened area with average 657 HV hardness, Z_4 is the core of component which hardness is about 472 HV that has not been affected by the induction treatment, Z2 shows a dramatic loss of hardness from maximum 657 HV to minimum 357 HV, and Z3 is the over-tempering area whom hardness recovers with a less steep slope from 357HV to 472 HV.

This variation in hardness is a consequence of an existing gradient of temperature in the different layers, i.e. Z_1 has been heated above austenitizing temperature, Z_2 has been heated to inter critical temperatures (between Ac_1 and Ac_3), Z_3 has not been transformed to austenite but suffers high temperatures that induce tempering and Z_4 remains unaffected.

These transformations induce internal stresses of compressive nature at the surface due to martensitic transformation. Residual stresses are effective for dynamically loaded components (Grum 2007). They increase not only wear resistance, but also overall toughness (Bhadeshia and Honeycombe 2006). The absolute amount of residual stress on the surface and the stress profile in the transition from compressive into tensile stresses are important characteristics for fatigue life (Grum 2007).

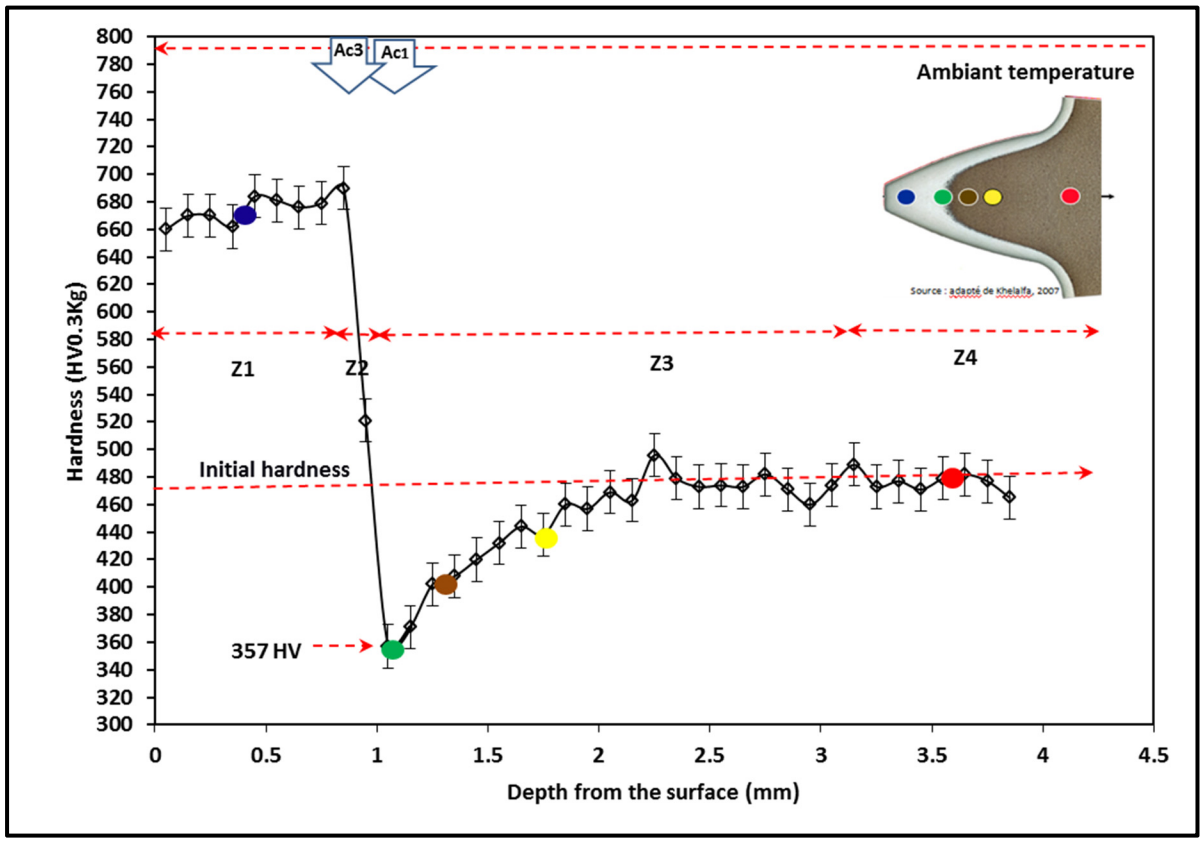

Figure 2-1 Hardness profile along the cross section of an induction hardened gear tip, circle from left to right are belong to hardened zone, lowest hardness, hardness-loss zone, and the last one core, standard error is used for this measurement .

The variation of hardness and residual stress profile versus distance in gear components is shown in Figure 2-2. The maximum residual tensile stress occurs in the over-tempering zone,

which has the lower hardness. However, it is recommended to have the most sensitive region of the steel parts, under compressive stresses to avoid from nucleation and propagation of fatigue cracking (Bhadeshia and Honeycombe 2006), which it is not compatible with our condition.

In addition, fatigue test results are shown the lowest amount of maximum stress to failure for the samples representing the over-tempering zone. Figure 2-3 shows these results on uniform hardness samples from different parts of gear after induction hardening. It indicates that representative samples with hardness equal with the core of gear have the middle amount of maximum stress to failure. Also, the samples represent the surface of gear with highest amount of hardness have the highest values of maximum stress to failure.

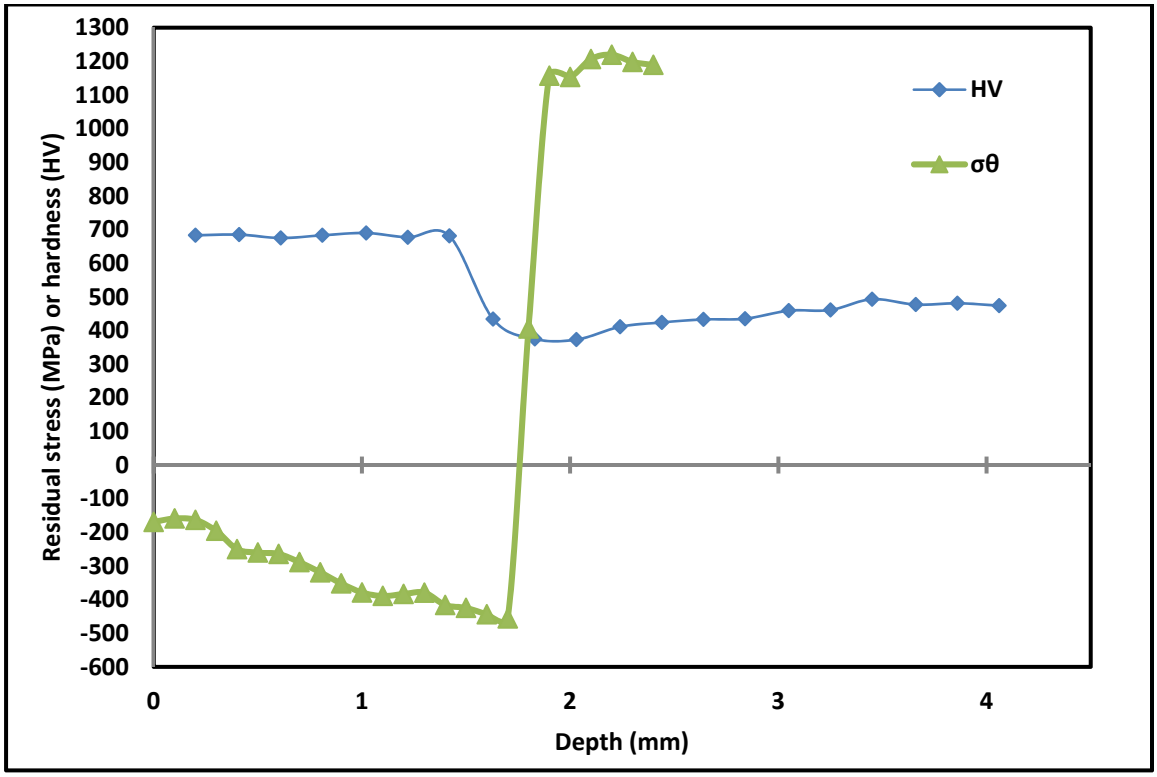

Figure 2-2 Hardness and residual stress profiles in hardened case depth (Savaria 2014).

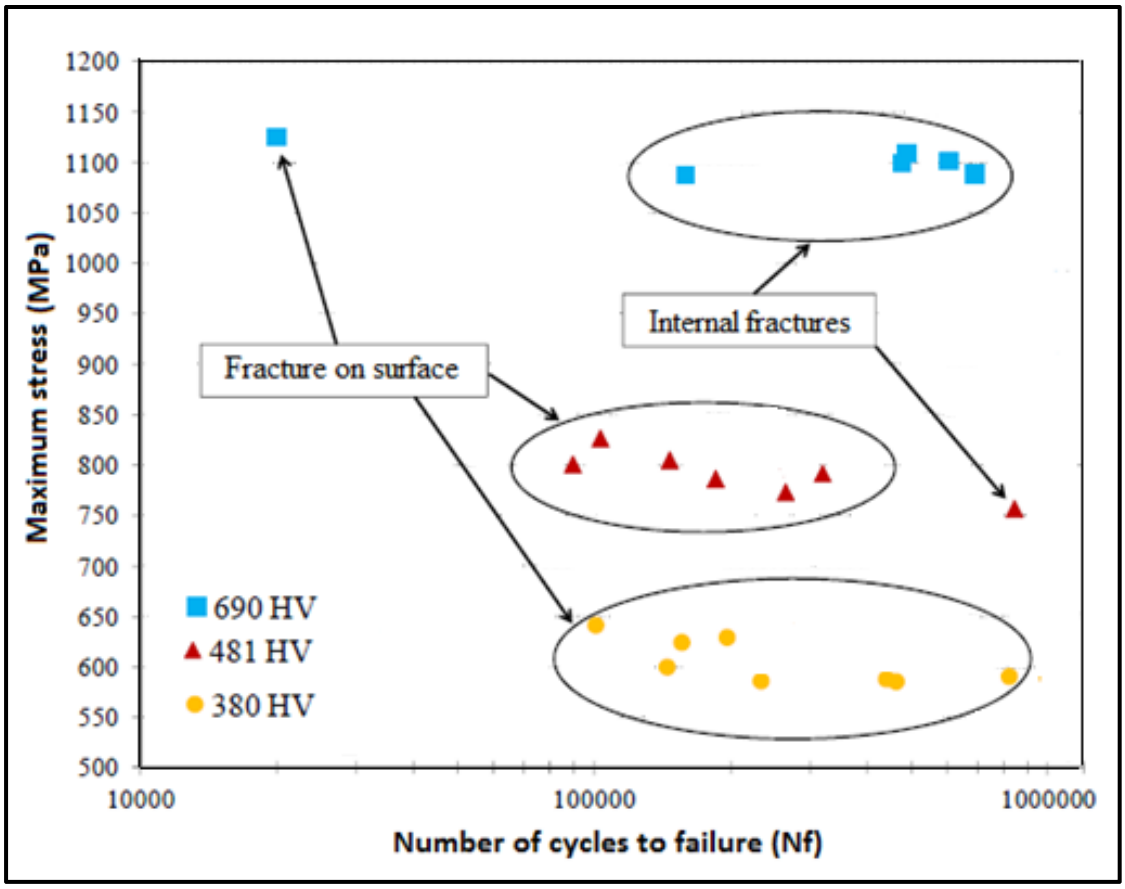

Figure 2-3 Illustration of fatigue testing result on uniform hardness sample (R=-1), (Savaria 2014).

2.3 Research problematic

The existence of over-tempered zone with low hardness even lower than initial ones where the maximum tensile residual stress is located has a long lasting concern for aerospace industry after induction hardening treatment of gear component AISI 4340 martensitic steel. Therefore the concern of this research is to know the effective parameters which decrease the mechanical properties of this area. Investigating around this subject requires knowing the kinetics evolution of microstructural features.

2.4 Research objectives

Investigating the evolution of hardness based on microstructural features in the over-tempered zone is the main purpose of this research; therefore, the classical kinetics involved in the AISI 4340 martensitic steel was identified and quantified by experiments and computational material science as following:

- The final properties of the component in over-tempered zone are determinted by some microstructural characteristic factors such as size, morphology, volume fraction, number density and size distribution of precipitates. These parameters accompanying the chemical composition of the matrix and the dislocation density influence on softening.
- In addition, the mobilities and other relevant kinetics factors are used in a formalism suitable to a model industrial alloy that is multicomponent, complex alloy. This parameters are used in an overall kinetic model to predict the hardness of the over-tempering zone of AISI 4340 steel under the non-isothermal conditions intrinsic to the nature of the induction process.

To do so, an investigation of the alloy under experimentally controlled thermal conditions i.e. isothermal at different tempering temperatures help to reach optimal description of the alloy. The microstructural investigation made use of quantitative metallography of scanning electron microscopy (SEM) images to quantify the number and the size of the mean carbides at different stages of tempering. The experimental information is used to obtain reliable set of parameters for the modeling process. This information is thus a crucial point in this project.
Once the calculated parameters are set, they are used to predict the constant of coarsening, and to determine the significant role of alloying elements. Then, other alloy compositions can be proposed to minimize the extent and the magnitude of the over-tempering zone. The results could be used in a larger scale finite element simulation of the induction process for process optimization. Figure 2-4 shows a block diagram of the procedure used for this research.

2.5 Industrial spinoffs

Hardness in over-tempered zone is measured and predicted by using a semi-empirical model. This model could propose other alloy compositions to minimize over-tempering zone. In another word, application of this model could help to prevent or predict subsurface fatigue failures. This model can be used as a guideline for process design or material selection, for industrial research project.

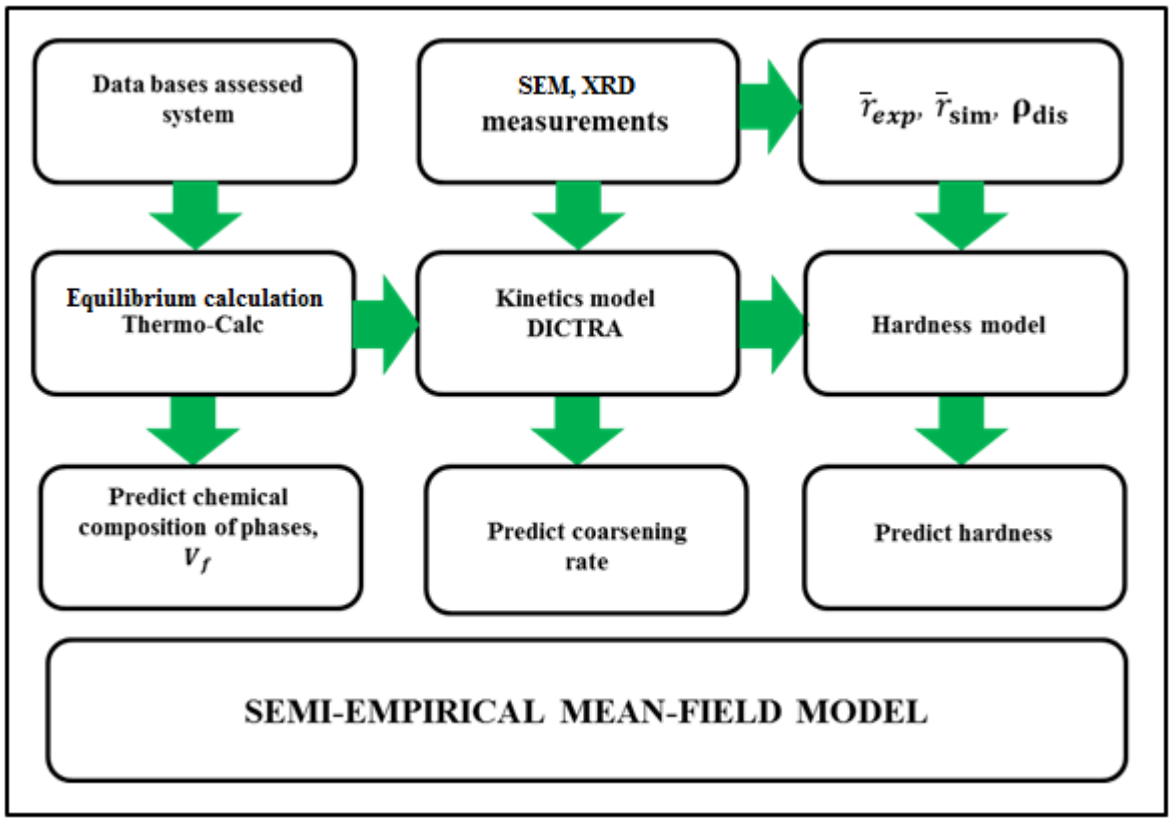

Figure 2-4 Block diagram of research procedure.

CHAPTER 3

METHODOLOGY

3.1 Introduction

In this chapter, the procedure to produce representative samples of over-tempered zone is introduced. Then different methods are used to monitor the microstructure of prepared samples. Developed Image analysis tool is used to determine the characteristics of microstructures. Mathematical methods are introduced to calculate the inter-particle spacing and volume size distribution of the precipitates.

3.2 Material

Standard chemical composition of AISI 4340 low alloyed medium carbon steel, which is equivalent of aerospace standard AMS 6414 used for this research, is shown in Table 3-1.
A 485 HV tempered martensite, which is typical hardness value for the core region of induction hardened 4340 parts provide from industry. This steel has been austenitized at 1123 K (850 °C) for 45 min, quenched in liquid with 10 percent polymer, and then tempered at 653 K (380 °C) for 90 min in controlled atmosphere. Blocks of size 4×9×12 mm^3 dimensions were cut from the determined material.

Table 3-1 The chemical composition of 4340 and equivalent aerospace standard 6414 steel (ASM 1995)

Chemical Composition, (wt%)									
Grade	**C**	**Cr**	**Mn**	**Mo**	**P max**	**S max**	**Si**	**Ni**	**Cu**
AISI 4340	**0.37-0.43**	**0.7-0.9**	**0.6-0.8**	**0.2-0.3**	**0.035**	**0.040**	**0.15-0.3**	**1.65-2.00**	**--**
AMS 6414	**0.38-0.43**	**0.7-0.9**	**0.65-0.9**	**0.2-0.3**	**0.01**	**0.01**	**0.15-0.35**	**1.65-2.00**	**0.35**

3.3 Isothermal ageing

In order to analysis the precipitate sequences, isothermal tempering at temperatures lower than Ac_1 (formation of austenite) 823K (550˚C) for 5, 10, 30 and 90 min and 923K (650˚C) for 5, 10, 30, 60, 90, 120, 240, 480, 720, 1440, and 2900 min and 973 K (700˚C) for 3, 5, 10, and 12 min were made in electrical furnace in ambient atmosphere to reach the hardness of over-tempered zone. These temperatures and tempering times are selected based on additivity rule i.e. non-isothermal temperature profile during induction hardening can be divided into a series of discrete isothermal tempering reaction (Massih and Jernkvist 2009). Then, based on temperature and time equivalent equation Holloman-Jaffe, it would be possible to choose lower temperature and longer time of tempering instead of high temperature and short time of induction hardening treatment. The decarburized and oxidized surface layers were measured in appendix I to determine required thickness for grinding and polishing. The treatment temperatures were carefully monitored using a thermocouple connected to a reference sample with roughly a 10 °C uncertainty involved with temperature control. After tempering, the samples were quenched in a mixture of water with 10 percent polymer (aqua quench 251).

3.4 Hardness

Samples for Vickers (pyramid) microhardness measurements were mounted in thermosetting phenolic powder for grinding and polishing. Thermal cycle due to this preparation does not affect hardness as the temperatures are lower than 200 °C and the duration of exposition is limited to a few minutes. They were grinded on SiC paper from 80 up to 1200 grit. The average hardness of 5 different points with 2,942 N (300 kgf) loads was measured with micro hardness tester FM Future-Tech corp and reported based on procedure (ASTM E384 – 10).

3.5 Microstructural characterisation

In this research, the microstructural evolution is monitored by quantitative metallography of samples tempered under isothermal conditions. It is used to find the evolution of size, inter-

particle spacing, shape, roundness, chemical composition, size distribution, volume fraction and density of precipitates with tempering time.

However the combination of fine and coarse scale of the microstructural features under investigation requires advanced, although well-established metallographic techniques that would be somewhat detailed in the following:

SEM: A scanning electron microscope produces images of a sample by scanning it with a beam of electrons. The information given is the surface topography and composition can be detected by various signals which are produced when the electrons interact with electrons in the depth of sample. Electron Backscatter Diffraction dark field is used to give better contrast.

XRD: X-ray diffraction is a technique for characterizing crystalline materials. The incident beam on a crystalline material causes a diffracted beam that yields information about the structure of the crystal. It provides information on precipitates chemical composition, and dislocation substructure.

3.5.1 **Metallography**

Prepared isothermal tempered sample were then polished with pads soaked with monocrystalline 1 micron diamond suspension. They were subsequently removed from mounted cover and etched for 20 min in Boiling Alkaline Sodium Picrate (BASP) etchant to darken cementite precipitates (Bramfitt and Benscoter 2002). The microstructure of samples was observed with scanning electron microscope (SEM) Hitachi S3600N and Hitachi SU70 under 7000 times magnification and 15 to 20 KV voltages.

3.5.2 **Extraction replica**

Besides sectioning method, extraction replica was used as a complementary procedure was used to quantify the precipitate characteristics. These methods allow extracting information on the morphologies, and measure the composition of precipitates that is required for

studying coarsening. Precipitates size could be derived accurately when the particles were not too large.

Extraction replica preparation was done in the same way that discussed for sectioning method but etching was done in 3% alcohol and nitric acid (Nital) solution. Etched samples were coated in Edwards vacuum carbon coater E306 and replica were extracted by floating the carbon films in 10% Nital solution, and collected on flat aluminum SEM holders. Figure 3-1 shows the schematic procedure for extracting particles from matrix by carbon replica technique.

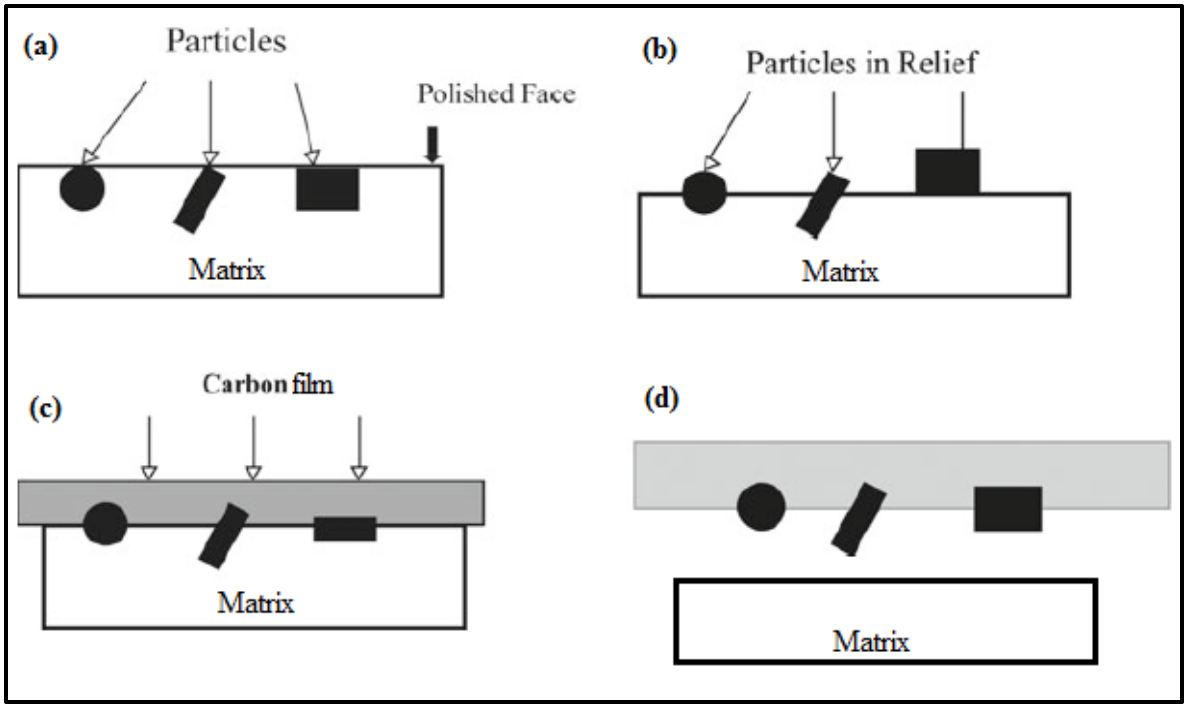

Figure 3-1 (a) Initial sample; (b) sample after polishing and chemical etching; (c) sample after carbon deposition; and (d) extracted particles by carbon replica separated by chemical etching from matrix (Ayache, Beaunier et al. 2010).

The extracted precipitates were observed in a scanning electron microscope (SEM), using secondary electron detector (SE), and backscattered electron (BSE) detectors dark field to

enhance the phase contrast between cementite precipitates and aluminum holder. SEM was operated at 3 to 5 KV and under magnification 7000. Compositions have also been measured by energy dispersive x-ray spectroscopy (EDX) at 15 KV. Figure 3-2 (a) to (c) illustrates the procedure used for sample preparation by Edwards vacuum carbon coater (E306) for extraction replica technique.

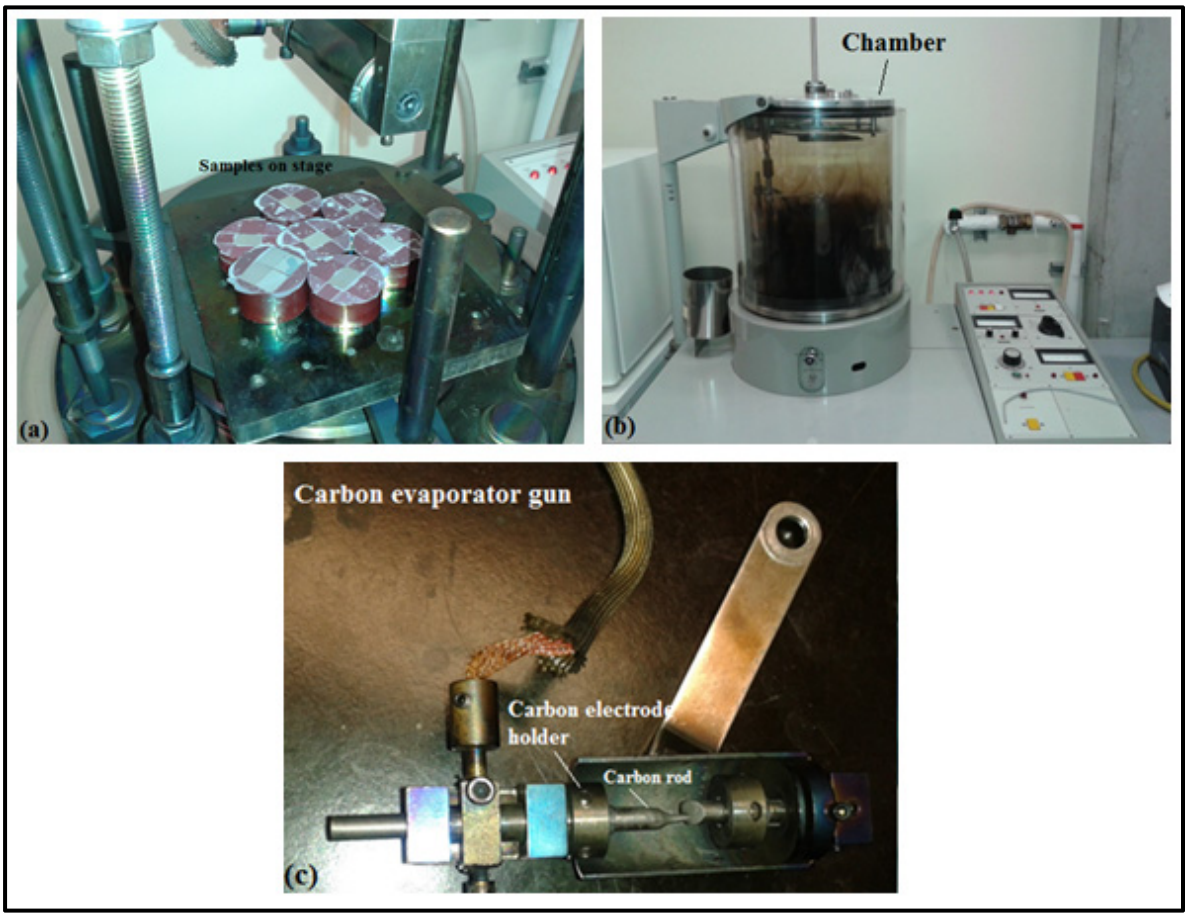

Figure 3-2 The procedure of extraction replica sample preparation a) prepared samples located on holder of carbon deposition machine, b) the chamber of carbon deposition, c) carbon evaporator gun

BASP etching and replica techniques were used for different purposes, sectioning is appropriate for stereological analysis such as volume fraction and size distribution and replica result was devoted to quantify roundness and morphology of precipitates. Usually a bias was introduced in the quantification of precipitate size distributions, because the larger precipitates cannot be extracted at later stages of coarsening by using the extraction replica technique.

3.5.3 **Electrolytic extraction**

Electrolytic extraction of carbides was used according to standard (E963-95) in 10% hydrochloric acid aqueous solution. A 3 volt DC potential has been set with a stainless steel electrode as cathode, samples are kept in solution by tantalum holder Figure 3-3 (Byeon and Kwun 2003). The dissolution of matrix in acid allowed to isolate cementite carbide entirely. The agglomerated powder after operation was analyzed by X-ray diffraction (XRD) and its composition measured by EDX in SEM chamber. The X'pert High score software was used to analyze the XRD patterns of powder.

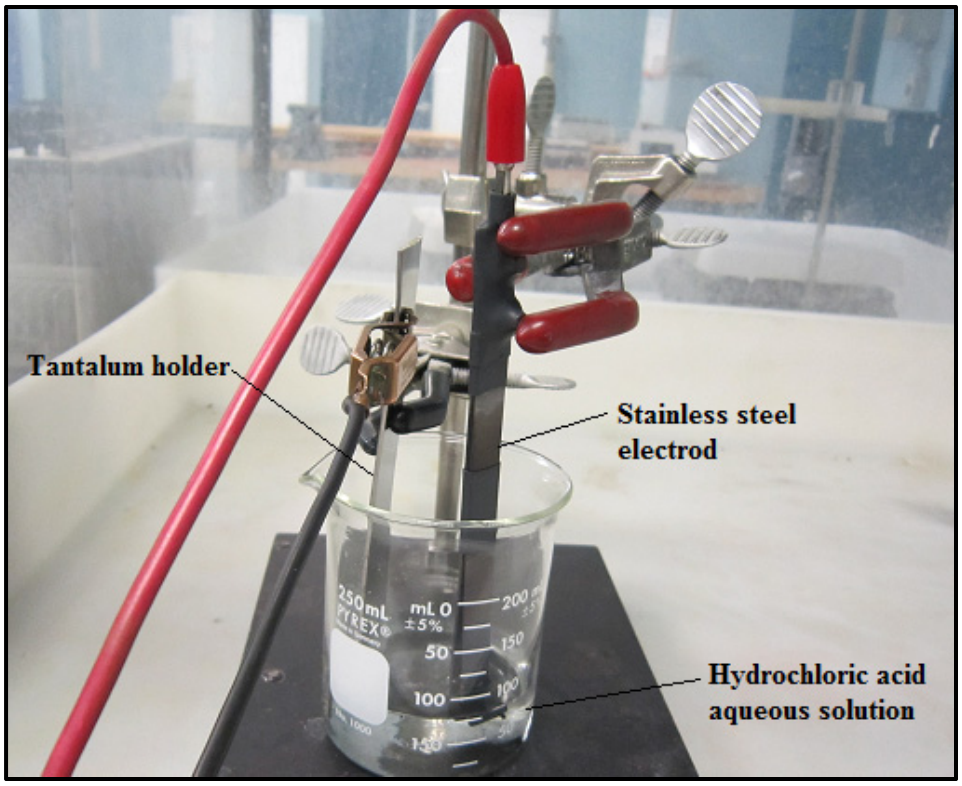

Figure 3-3 Illustration of electrochemical reaction procedure for extracting precipitates carbides from matrix

3.6 Image Analysis

Back scattered-dark field SEM images have been analyzed using an in-house developed software based on Image J digital image analysis software package (Schindelin, Arganda Carreras et al. 2012) (Schneider, Rasband et al. 2012).

The principle is to use digital segmentation procedures to produce binary images suitable to particle analysis. The software operations include watershed segmentation, binarization, and particle section analysis. It is followed by denoising and validations of the detected particles by superposition of the binarized image with the original image. Figure 3-4 shows the different steps of operation on a SEM image.

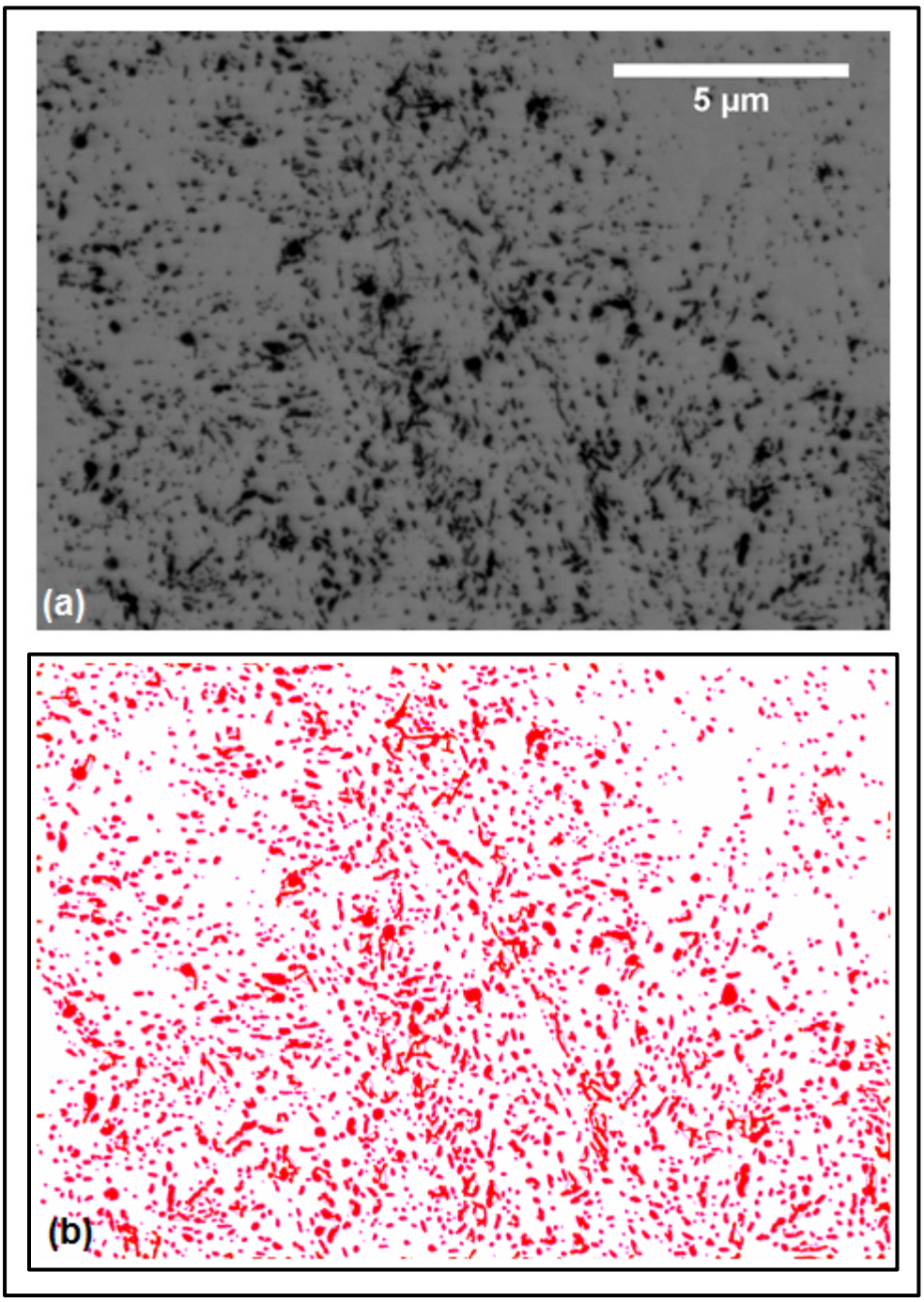

Figure 3-4 Tempered sample at 923 K (650 °C) for 60 min
revealing by carbon replica a) SEM microstructure
b) particles-segmentation and binarization,
c) validation

Figure 3-4 (continued)

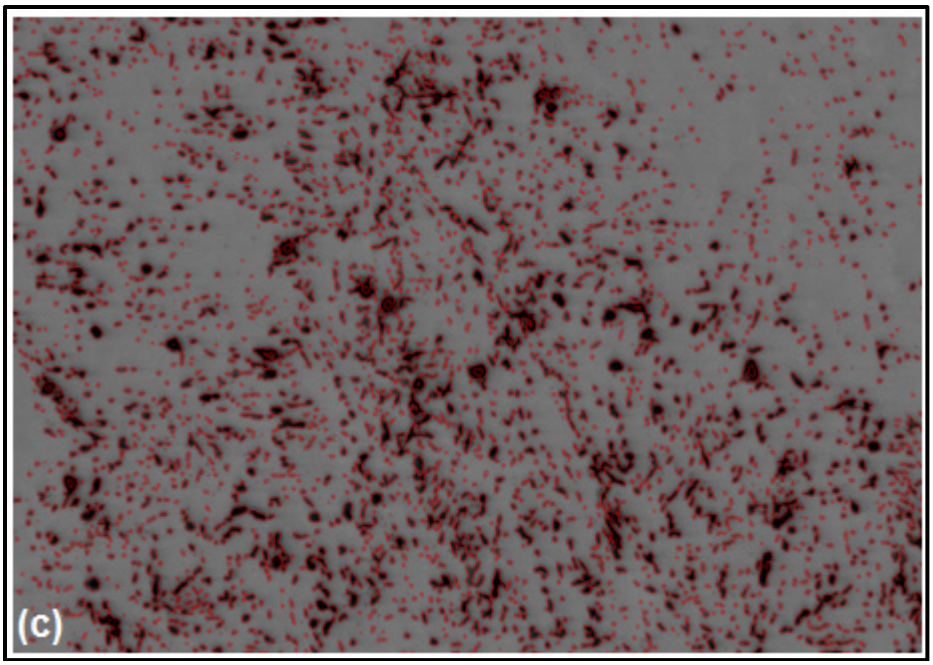

3.7 Particle Size Distribution

3.7.1 Number density

The number density values N_A directely measured on the polishing plane is not representative of the bulk information, because after sectioning all the particles are not lucky to cut from the biggest diameter. Figure 3-5 displays how sectioning procedure could cut particles from different diameters. Therefore the particle size distribution and the number density of precipitates for the bulk should be corrected with Saltykov 's coefficients methods (Underwood 1970) (Lewis, Walters et al. 1973).

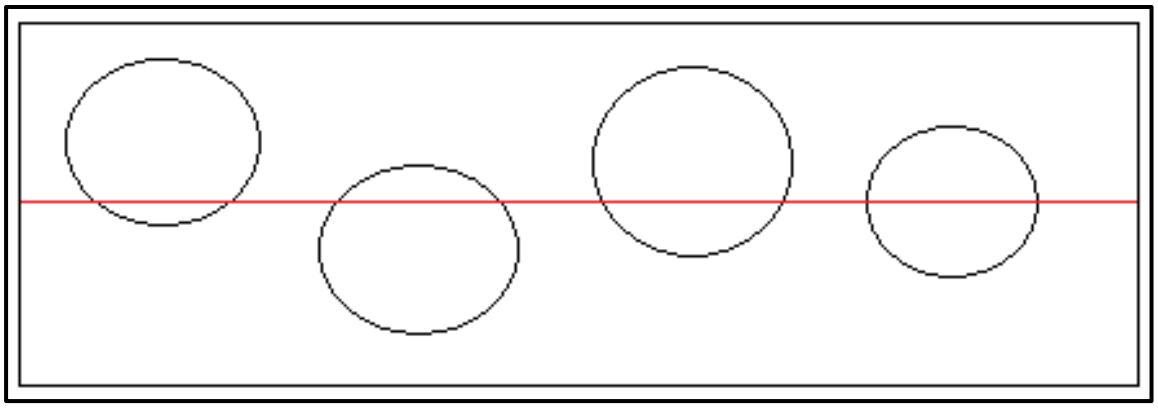

Figure 3-5 Schematic illustration of how sectioning procedure could cut particles from different diameters.

In this method, precipitates with different shapes have been assumed as a spherical particles located in a poly dispersed system. Instead of absolute area for particles, the ratio of $\frac{A}{A_{max}}$ is used to determine the section area. A large number of particles in polished sections are examined to determine A_{max} value, due to significant important of it in this calculation. Also, twelfth class interval are considered. The class intervals is determined based on a logarithmic scale of diameters with factor $(10^{-0.1})^{n} = 0.7943$ (n=number of class) (Underwood 1970). Figure 3-6 displays the 5 class intervals of this method to explain how the corrected Saltykov's coefficients method categorized particles.

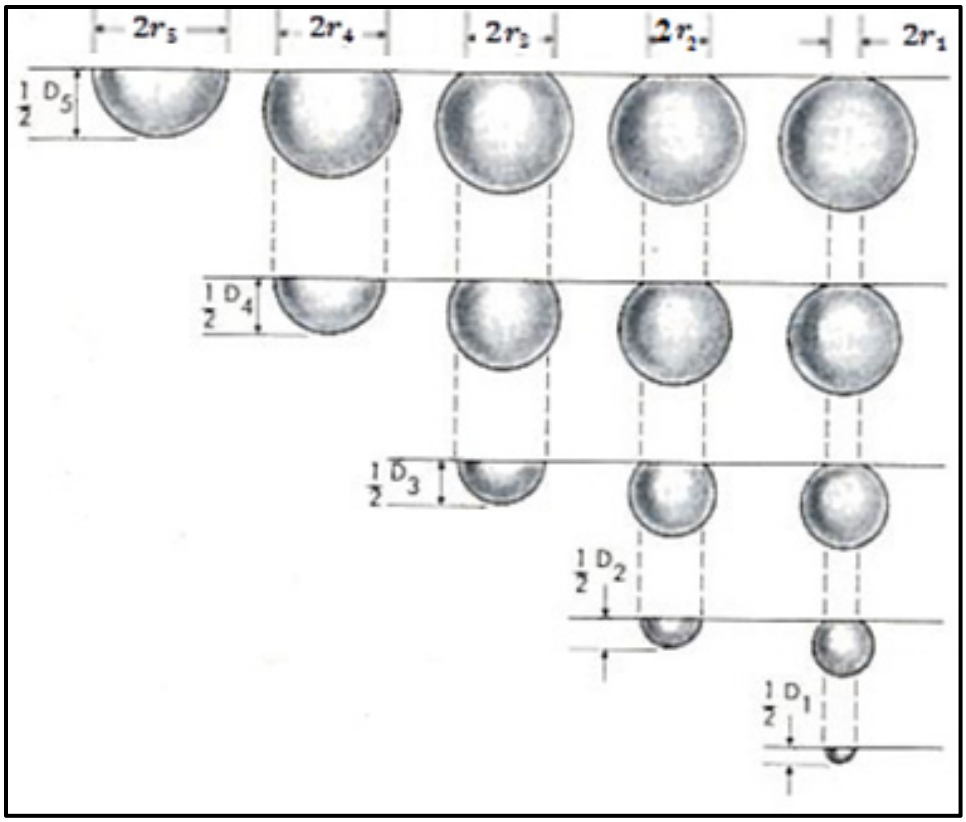

Figure 3-6 Schematic illustration of the 5 class intervals of sectioned spherical particle in Saltykov methods (Underwood 1970).

For each class the maximum diameter is defined (D_i). Then, the volume number density could be derived from the following equation (3.1) for 12 class intervals.

$$(N_V)_i = \frac{1}{D_i}[1.6461 \times (N_A)_i - 0.4561 \times (N_A)_{i-1} - 0.1162 \times (N_A)_{i-2} - 0.0415 \times (N_A)_{i-3} - 0.0173 \times (N_A)_{i-4} - 0.0079 \times (N_A)_{i-5} - 0.0038 \times (N_A)_{i-6} - 0.0018 \times (N_A)_{i-7} - 0.0010 \times (N_A)_{i-8} - 0.0003 \times (N_A)_{i-9} - 0.0002 \times (N_A)_{i-10} - 0.0002 \times (N_A)_{i-11}]. \quad (3.1)$$

where $(N_V)_i$ is number of particles in class i per unit volume, and $(N_A)_i$ is number of particles in class i per unit area. For this calculation $(N_V)_i$ for a given class is continued until

the index of $(N_A)_i$ reduces to zero. i.e. to calculate $(N_V)_1$ only the first term, and for $(N_V)_{12}$, 12 coefficients are needed as follow:

Class No.1 $(N_V)_1=(1/D_1)\times[(1.645\times(\mathrm{N_A})_1]$

.

.

.

Class No.12 $(N_V)_{12}=(1/(D_{12})\times[1.645(\mathrm{N_A})_{12}-0.4542\times(\mathrm{N_A})_{11}-0.1173\times(\mathrm{N_A})_{10}-0.0423\times(\mathrm{N_A})_9-0.01561\times(\mathrm{N_A})_8-0.0083\times(\mathrm{N_A})_7-0.0036\times(\mathrm{N_A})_6-0.0019\times(\mathrm{N_A})_5-0.0009\times(\mathrm{N_A})_4-0.00044\times(\mathrm{N_A})_3-0.00036\times(\mathrm{N_A})_2-0.0001\times(\mathrm{N_A})_1]$.

Class number 1 is for the largest particles, and class number 12 in for the smallest particles. The volume size distribution, number density could determine by application of this method. The evolution of particle size distribution of precipitates during coarsening process reaches steady state. It follows the Lifshitz-Slyozov-Wagner (LSW) distribution law. The theory of LSW predicts that the kinetics of coarsening and the particle size distribution function could apply to dilute systems i.e. in the limit of zero volume fraction of second particle, in which the interaction between particle-particle are not significant (Lifshitz and Slyozov 1961) (Baldan 2002) (Tiryakioğlu, Ökten et al. 2009). Its propability density function (f) is written as equations (3.2) and (3.3):

$$f\left(\frac{r}{\bar{r}}\right)=\frac{4}{9}\left(\frac{r}{\bar{r}}\right)^2\left(\frac{3}{3+\frac{r}{\bar{r}}}\right)^{\frac{7}{3}}\left(\frac{1.5}{1.5-\frac{r}{\bar{r}}}\right)^{\frac{11}{3}}exp\left(\frac{\frac{r}{\bar{r}}}{\frac{r}{\bar{r}}-1.5}\right)\quad 0<\frac{r}{\bar{r}}<1.5 \tag{3.2}$$

$$f\left(\frac{r}{\bar{r}}\right)=0\,;\ \frac{r}{\bar{r}}\geq 1.5 \tag{3.3}$$

when $\frac{r}{\bar{r}}$ is the normalized particle size, and $\bar{r}$ the mean spherical radius is the only parameter that should be estimated. Based on this equation no particle have normalized size larger than 1.5 as shown in Figure 3-7 (Tiryakioğlu, Ökten et al. 2009). In next chapter, the corresponding normalized volume size of LSW distributions are calculated for comparison with normalized volume size distribution of precipitates.

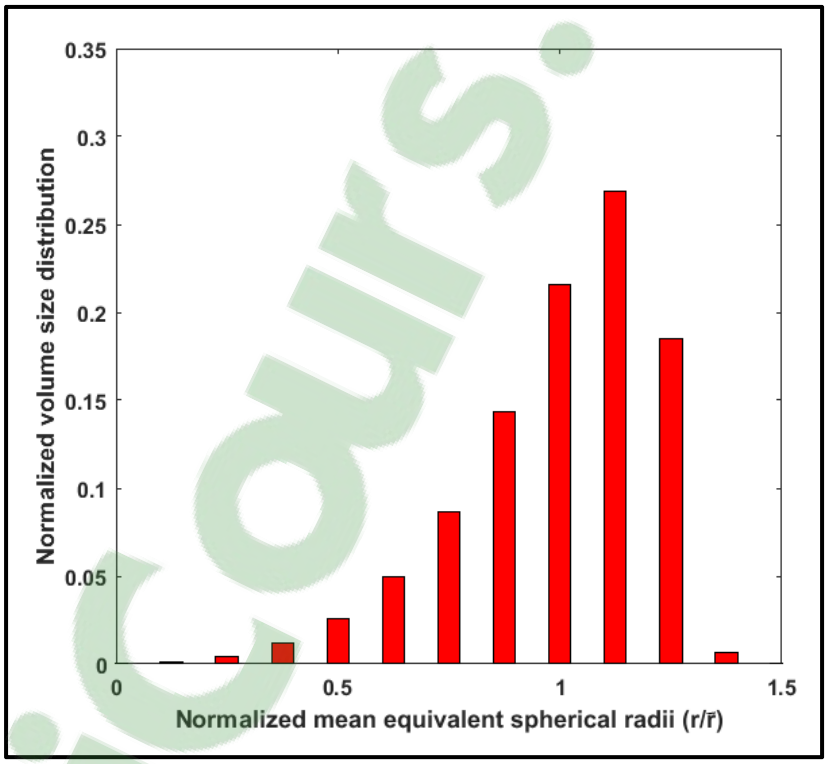

Figure 3-7 Illustration of LSW particle size distribution.

3.7.2 **Mean values**

The average mean radius of precipitates can be extracted from previous particle size distribution data from equation (3.4):

$$\bar{r} = \frac{\sum_i (Nv)_i r_i}{\sum_i N_i} \tag{3.4}$$

where $(Nv)_i$ is number of particle per unit volume $(\#/m3)$ in each size class and r_i is the maxium mean radius related to each size class i. Then, the total number of precipitates can be derived based on equation (3.5):

$$N = \sum_i N_i \tag{3.5}$$

In addition, based on above theoretical values the volume fraction of spherical particles can be calculated by the following equation (3.6) (Nicolas 2009).

$$V_f = \sum_i \frac{4}{3} \times \pi \times r_i^3 \times N_i \tag{3.6}$$

3.8 **Mean free distance or inter-particle spacing (λ)**

Important parameter to determine the microstructural features is inter-particle spacing, λ which is defined by Fullman equation (3.7):

$$\lambda = \frac{1 - V_f}{N_L} \tag{3.7}$$

where V_f is volume fraction of second particle, and N_L is the number of intercept particles per unit length of random line. It can be assumed that N_L is proportional to N_s (number of intercept particles per unit area). This equation is applicable in any system regardless of size, shape, distribution (Underwood 1969) (Underwood 1970). Then, it is possible by considering equation (3.6) per unit area, and equation (3.7) extract the mean free carbide path or inter-particle spacing λ equation (3.8):

$$\lambda = \frac{4}{3} r \frac{(1-V_f)}{V_f} \tag{3.8}$$

where V_f is the theoretical equilibrium volume fraction of particle, and r is the spherical equivalent mean radius of particles (Caron and Krauss 1972).

3.9 XRD analysis

X-ray diffraction was used to analysis the extracted powder obtained from electrolytic extraction. Diffractometer system XPERT-PRO using average CuKα_1 and CuKα_2 radiation equal 1.54187 °A wavelength, with voltage 45 KV and 40 mA with step size of 2θ equal 0.0330 is used for this matter. The scan start position (°2θ) started from 30.0167 and end scan position (°2θ) was 99.9437.

It is also used to determine the dislocation density of tempered sample. The initial quenched and tempered sample at 653 K (380 °C) and tempered samples at 923K (650 °C) and very short time are characterized. Sample preparation, grinding and polishing to reach a smooth surface was performed to apply XRD test. Diffractometer system XPERT-PRO using average CuKα_1 and CuKα_2 radiation equal 1.54187 °A wavelength, with voltage 45 KV and 40 mA with step size of 2θ equal 0.0170 is used for this matter. The scan start position (°2θ) started from 35.0184 and end scan position (°2θ) was 155.9904. This information was used to detect and estimate the line broadening and micro strains ε_{micro}due to tempering process. The instrumental broadening is also taken into account by XRD measurement on 4340 steel before any heat treatment.

3.10 **Summary**

In summary, the experimental procedure has been explained. Tempered samples prepared under isothermal condition are fully characterized by SEM electron microscope. Three methods are used to reveal and to determine the chemical composition of precipitates. Developed software based on image analysis tools used to measure the particle size, volume fraction, small and large diameters of precipitates. The other information size distribution and number density, and inter-particle spacing are derived from former results by application of mathematical methods.

CHAPTER 4

EXPERIMENTAL RESULTS AND DISCUSSIONS

4.1 Introduction

This chapter is dedicated to the investigation of hardness property, the microstructural evolution, and chemical composition of cementite in low alloyed medium carbon steel after isothermal tempering treatment. The investigated samples are representative of over-tempered zone of fast hardening. Size, volume fraction, morphology, inter-particle spacing, and distribution of the particles are useful information for simulating the kinetics cementite coarsening.

4.2 Hardness

The evolution of hardness during tempering of the tempered martensite with initial 460 HV hardness can be seen in Figure 4-1 for tempering at 823 K (550 °C), 923 K (650 °C), and 973 K (700 °C). A gradual decrease in hardness with time at different tempering temperatures can be observed. Tempering AISI 4340 at temperatures over 823 K (550 °C) results a drop in hardness that is typically attributed to the rapid coarsening of iron based Fe_3C cementite by Ostwald ripening (Lee, Allen et al. 1991). At the temperature of 923K (650 °C), the hardness drops significantly for holding times less than 100 sec, from about 450 HV to 332 HV. For longer exposure period, the rate of softening changes, showing similar trend than the tempering effect at 823K (550 °C) on a hardness versus time on a log scale of this figure. The hardness reaches values much lower than the ones encountered in the over-tempered zone of induction hardened 4340 parts. At higher temperature of tempering 973K (700 °C) the trend of hardness showed lower values.

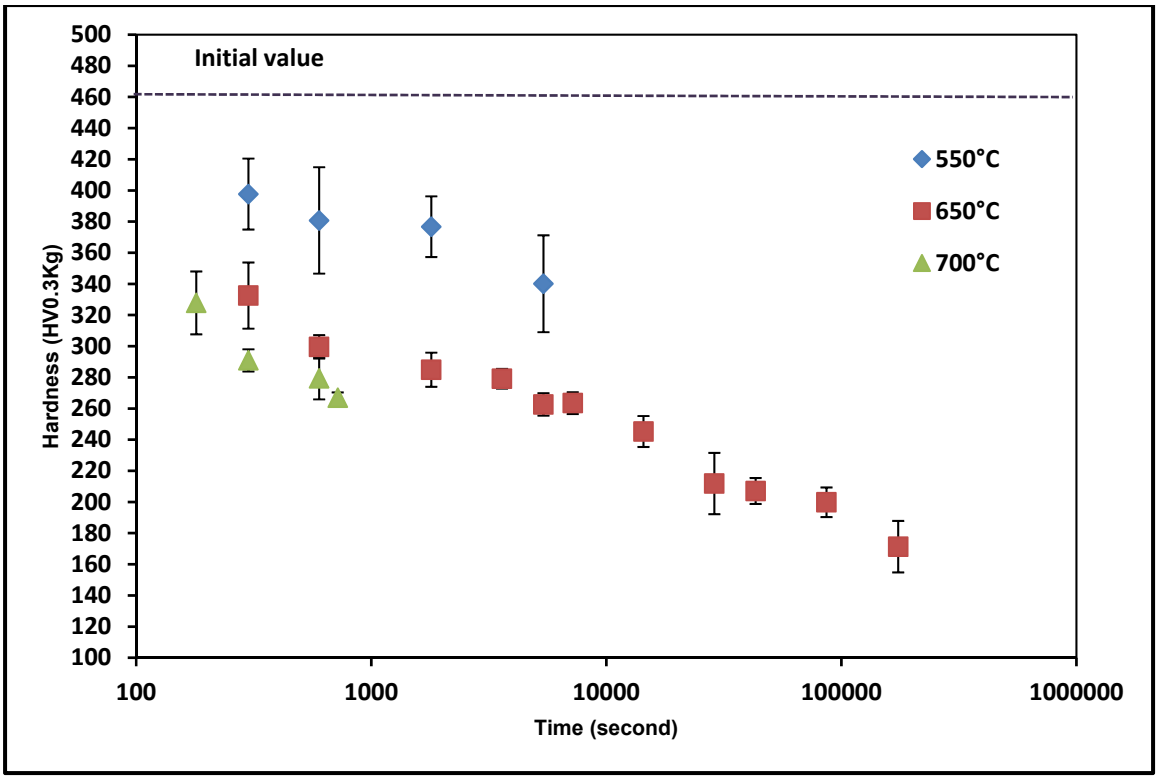

Figure 4-1 Hardness evolution during the tempering for various heating time at 550 °C, 650 °C, and 700 °C, the initial hardness value was added to the figure for reference.

4.3 Equilibrium calculations

Thermodynamic calculations were performed by Thermo-Calc software console mode version 3.1 in equilibrium multicomponent, multiphase systems in order to determine the equilibrium quantities of cementite in AISI 4340 steel at the investigated temperatures. The TCFE7 database was selected for this calculation. In order to make predictions on the equilibrium composition of metastable cementite, only ferrite and cementite have been retained for equilibrium calculations. The volume fraction of the cementite and equilibrium chemical composition of existing phases are calculated at the initial tempering condition 653K (380 °C) and at second tempering conditions 823K (550 °C), 923K (650 °C) and 975 K (700 °C). The volume fraction and concentrations of alloying elements in cementite and ferrite are represented in Table 4-1. Under equilibrium conditions significant partitioning of

Si and Ni in the matrix is predicted; however, Cr, Mn, and Mo partition preferentially in cementite at all temperatures.

Table 4-1 Predicted volume fraction and chemical compositions of cementite and ferrite at equilibrium condition calculated by Thermo-Calc software, wt%.

Temperature, K (°C)	Phase	Volume fraction, (%)	Fe	C	Cr	Mn	Mo	Ni	Si
653 (380)	Ferrite	93.87	97.58	4.85×10^{-05}	0.03	0.11	0.14	1.91	0.24
	Cementite	6.13	67.90	6.71	12.96	10.04	2.05	0.35	4.70×10^{-11}
823 (550)	Ferrite	93.90	0.97	1.00×10^{-03}	0.13	12.8	0.18	1.91	0.239
	Cementite	6.11	73.21	6.71	11.44	6.88	1.38	0.37	4.71×10^{-11}
923 (650)	Ferrite	93.95	97.00	5×10^{-03}	0.22	0.43	0.19	1.91	0.24
	Cementite	6.05	76.72	6.71	10.11	4.93	1.15	0.38	4.71×10^{-11}
973 (700)	Ferrite	94.01	96.88	9×10^{-03}	0.27	0.49	0.20	1.91	0.24
	Cementite	5.99	78.41	6.71	9.41	4.04	1.06	0.38	4.71×10^{-11}

4.4 Microscopic analysis

The initial quenched and tempered (Q&T) microstructure is displayed in Figure 4-2 (a) after BASP etching. Cementite is clearly delineated as a dense dispersion of dark elongated small precipitates, although a few bigger spherical ones are visible. The black and white image corresponding to the segmentation procedure starting from a grey-level image is shown for illustration purpose in Figure 4-2 (b). The average mean precipitate size of initial quenched and tempered sample is reported to be approximately 3.88×10^{-8} m by converting pixel section area to its equivalent radius.

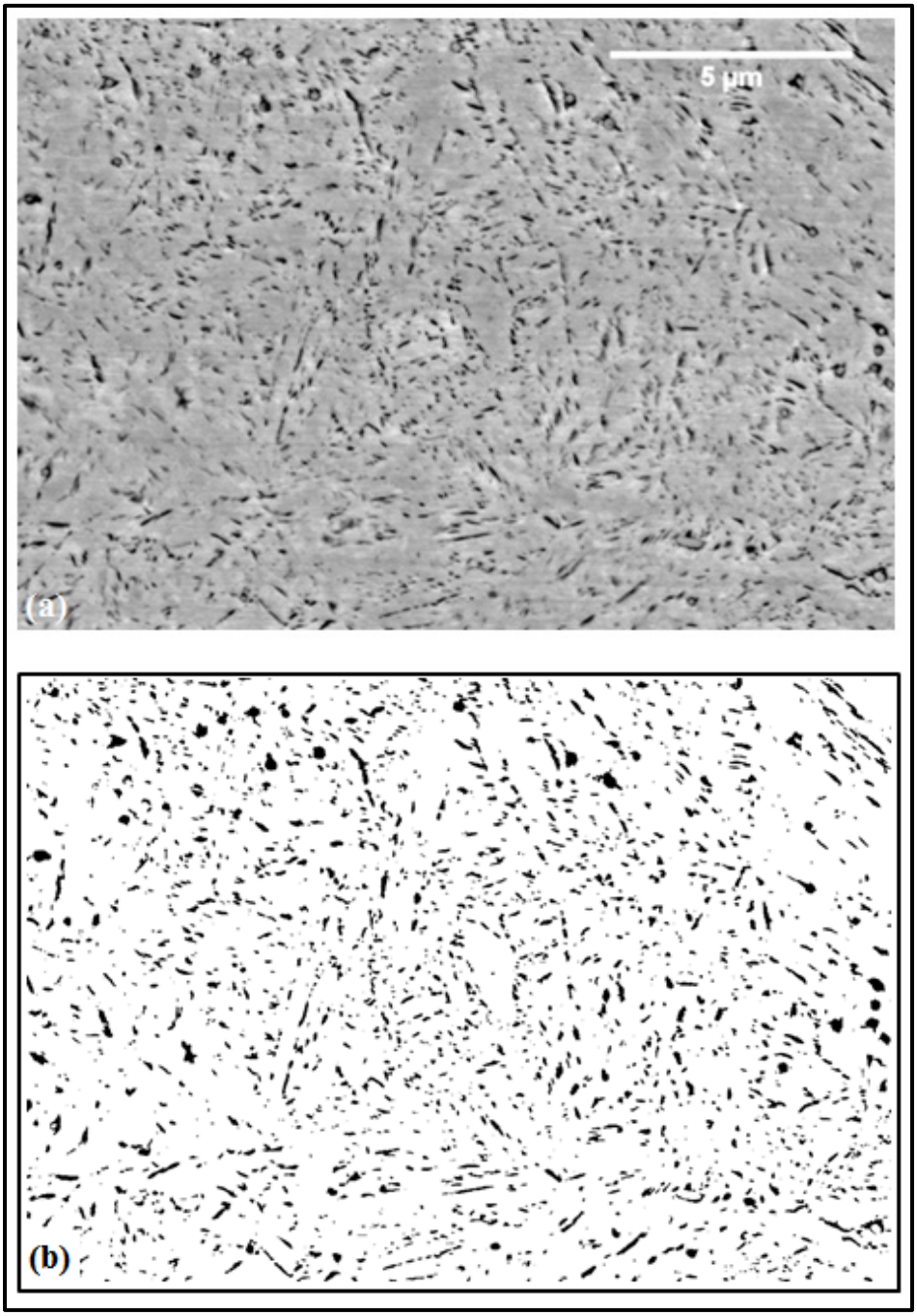

Figure 4-2 Initial quenched and tempered sample at 653 K (380 °C) for 90 min to reach 460 HV revealing by BASP etchant (a) SEM microstructure, and (b) segmented black and white image

The precipitation sequences documenting the coarsening of cementite dispersions in AISI 4340 during isothermal tempering at 923 K (650 °C) is presented in Figure 4-3. The average precipitate size increases with tempering duration and can be visually recognizable immediately even after 10 min of exposure as shown in Figure 4-3 (a). The black and white images corresponding to the segmentation procedure are shown for more illustration on Figure 4-3 (a´). In each tempering condition, precipitates of various shapes coexist; from fine globular to almost spherical ones. However after more than 60 min tempering at 923 K (650 °C) spheroidal precipitates become predominant, indicating coarsening occurs mainly by spheroidization and Ostwald ripening. The smaller and more sharply tipped precipitates disappeared after 240 min of tempering at this temperature to the expense of more spheroidal precipitates. As plate morphology is dominant in the initial quenched and tempered material, it can be inferred that the spheroidization of plates occurred before 60 min tempering at 923 K (650 °C), see Figure 4-3 (b), (b´). After longer time of tempering, a coarse microstructure constituted of spheres and idiomorphic precipitates was found in Figure 4-3 (g), (g´).

The comparison between the two carbide revealing techniques was illustrated in Figure 4-3 (c), (c´) and (d), (d´) for the sample tempered for 240 min. As it can be seen in later image, carbon replica extraction method lead to an overestimation of cementite volume fraction due to the non-negligible thickness of extracted cementite particles in the replica; therefore the estimated cementite volume fraction is much larger than the real one, however the size of the precipitates can be considered. In addition, at later stages of coarsening, the replica technique introduces a bias in the quantification of precipitate size because the larger precipitates cannot be extracted, see Figure 4-3 (e), (e´) and Figure 4-3 (f), (f´). Both techniques show similar precipitate size for 60 and 240 min of tempering.

The smaller and more sharply tipped precipitates are disappeared after 12 min tempering at 973 K (700 °C) by BASP revealing technique in Figure 4-4 (i), (i´) comparing to those observed after 5 min tempering in Figure 4-4 (h), (h´).

The equivalent sphere average radii were measured using SEM images in two different images of different locations in the samples, accruing 200 up to 2500 particles depending on the state of precipitation. Table 4-2 presents the mean spherical equivalent radius for different tempering times, with corresponding volume fraction of precipitates.

Table 4-2 The average mean equivalent radius and area fraction of precipitates extracted by microstructural analysis from tempered samples, the area fraction error is calculated based on volume fraction calculated by T-C

Temperature, K (°C)	Time, (min)	Carbide revealing techniques	Mean equivalent radius (Rm), (m)	Inter-particle spacing, λ(m)	Area fraction, (%)	Error area fraction, (%)
Q & T	**-**	**BASP**	**3.88×10^{-08}**	**7.92×10^{-07}**	**7.31**	**21**
923 (650)	**10**	**BASP**	**4.21×10^{-08}**	**8.72×10^{-07}**	**5.56**	**-8**
923 (〃)	**60**	**BASP**	**6.45×10^{-08}**	**1.34×10^{-06}**	**6.12**	**1**
923 (〃)	**60**	**Replica**	**5.73×10^{-08}**	**1.19×10^{-06}**	**14.26**	**136**
923 (〃)	**240**	**BASP**	**7.69×10^{-08}**	**1.59×10^{-06}**	**4.76**	**-21**
923 (〃)	**240**	**Replica**	**6.97×10^{-08}**	**1.44×10^{-06}**	**13.14**	**117**
923 (〃)	**720**	**BASP**	**1.17×10^{-07}**	**2.43×10^{-06}**	**6.30**	**4**
923 (〃)	**720**	**Replica**	**6.94×10^{-08}**	**1.44×10^{-06}**	**10.72**	**77**
923 (〃)	**1440**	**BASP**	**1.55×10^{-07}**	**3.21×10^{-06}**	**4.82**	**-20**
923 (〃)	**1440**	**Replica**	**7.54×10^{-08}**	**1.56×10^{-06}**	**8.01**	**32**
923 (〃)	**2900**	**BASP**	**1.68×10^{-07}**	**3.47×10^{-06}**	**5.44**	**-10**
973 (700)	**5**	**BASP**	**4.20×10^{-08}**	**8.79×10^{-07}**	**6.85**	**14**
973 (〃)	**12**	**BASP**	**4.62×10^{-08}**	**9.66×10^{-07}**	**5.08**	**-15**

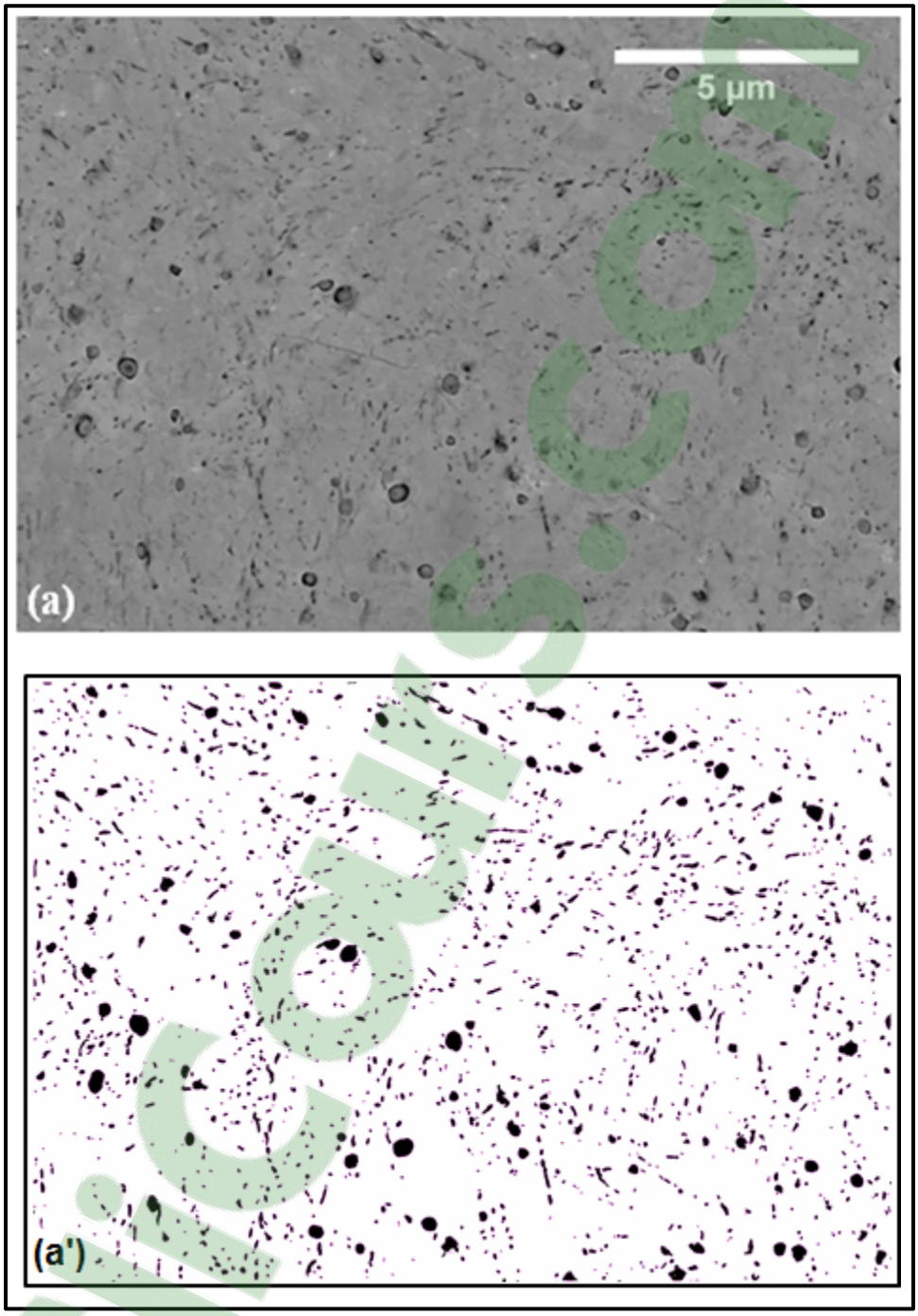

Figure 4-3 (a) SEM microstructure, and (a′) segmented black and white image of tempered steel at 923 K (650 °C) for 10 min revealing by BASP etchant

Figure 4-3 (continued) (b) (b´) at 923 K (650 °C) for 60 min
revealing by BASP etchant

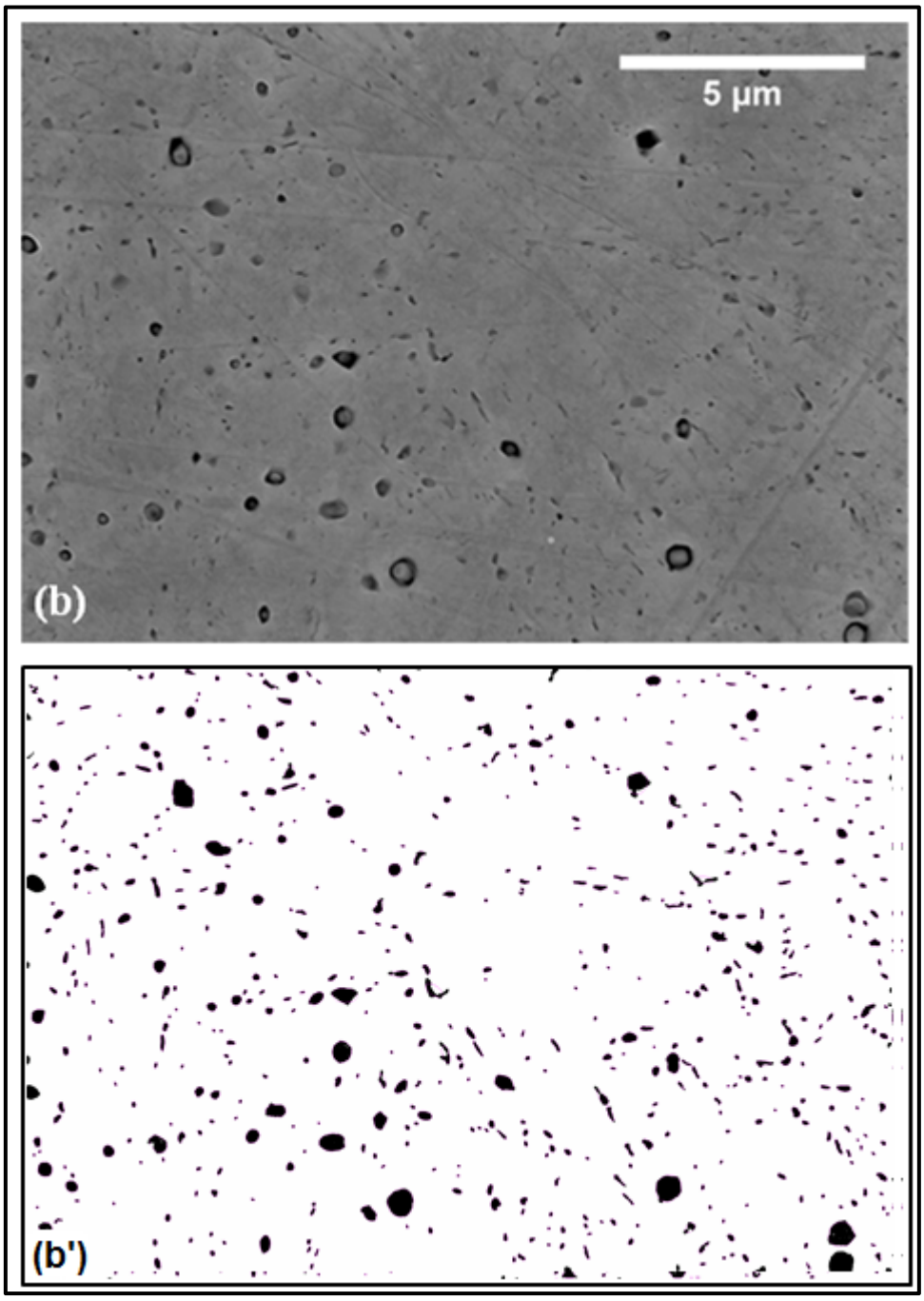

Figure 4-3 (continued) (c) (c´) at 923 K (650 °C) for 240 min revealing by BASP etchant

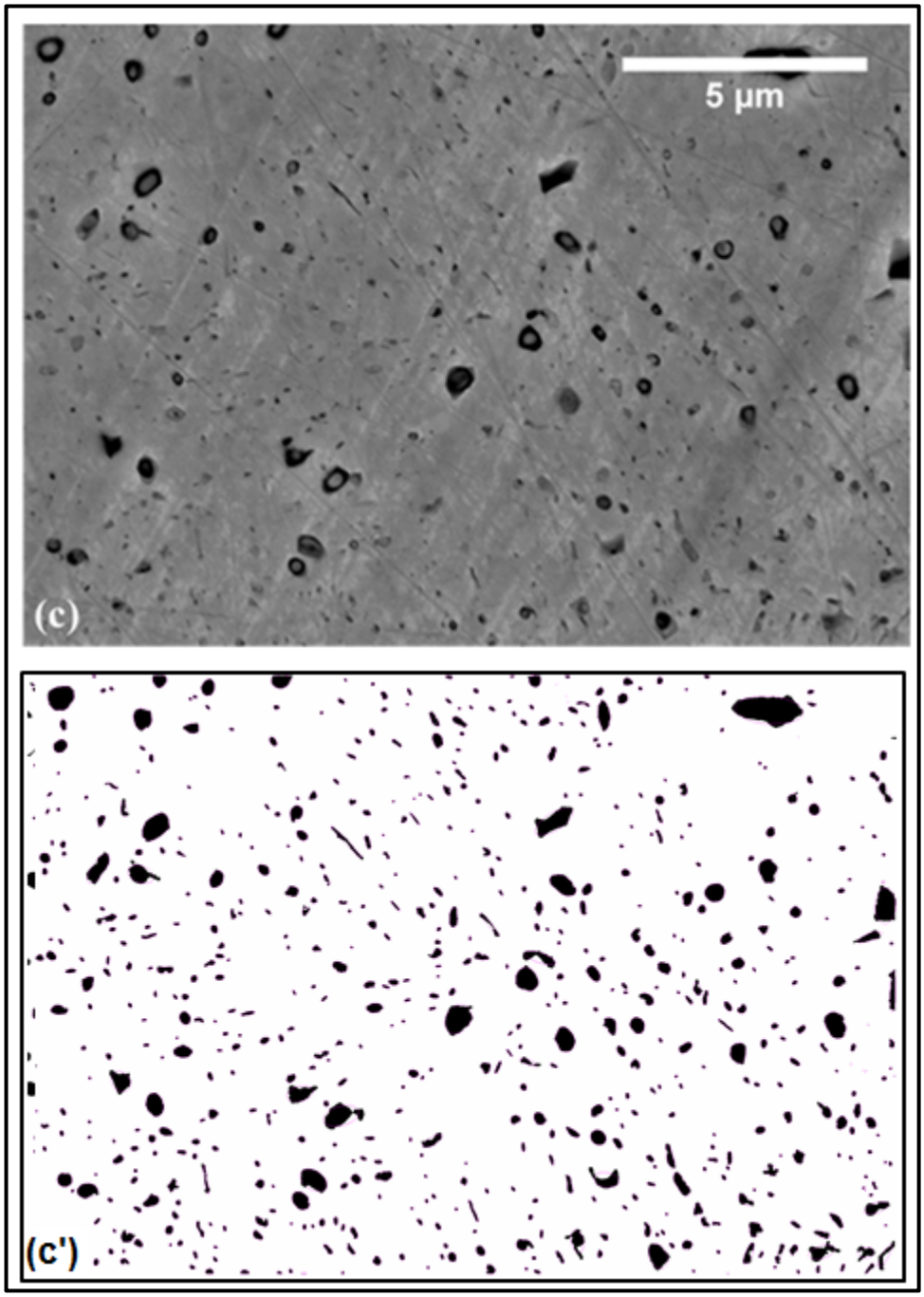

Figure 4-3 (continued) (d) (d′) at 923 K (650 °C) for 240 min
revealing by carbon replica

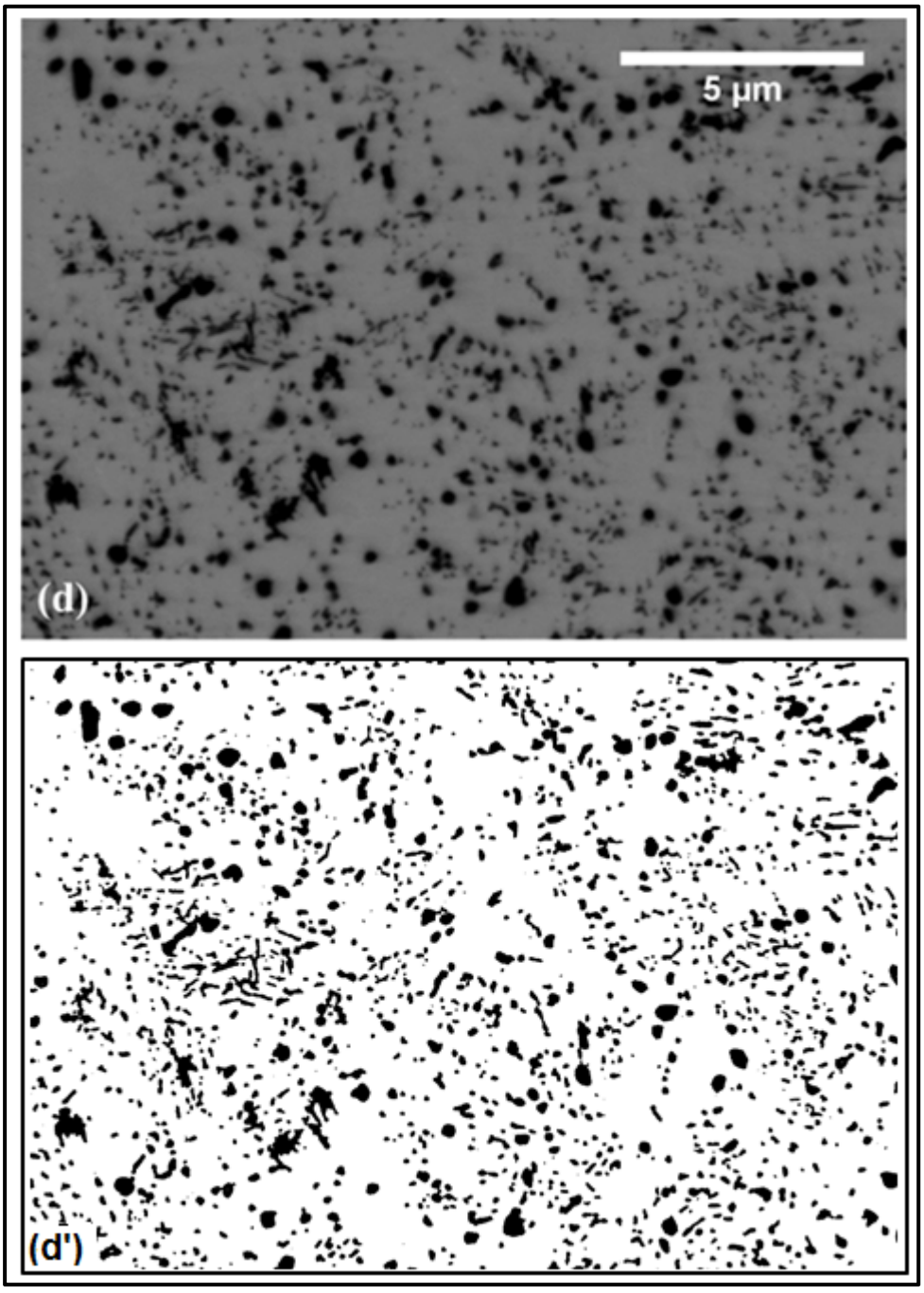

Figure 4-3 (continued) (e) (e´) at 923 K (650 °C) for 720 min revealing by carbon replica

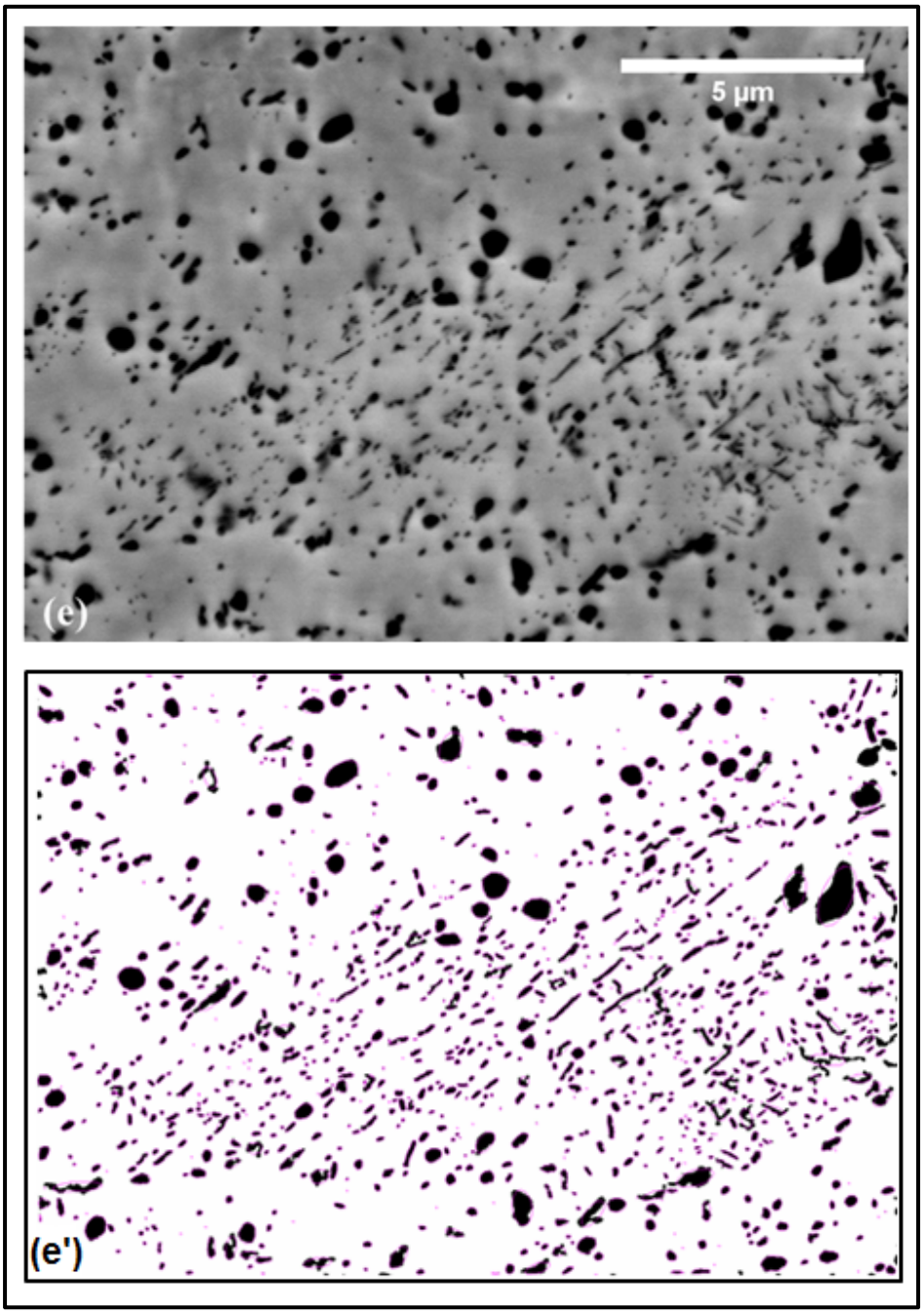

Figure 4-3 (continued) (f) (f´) at 923 K (650 °C) for 1440 min revealing by carbon replica

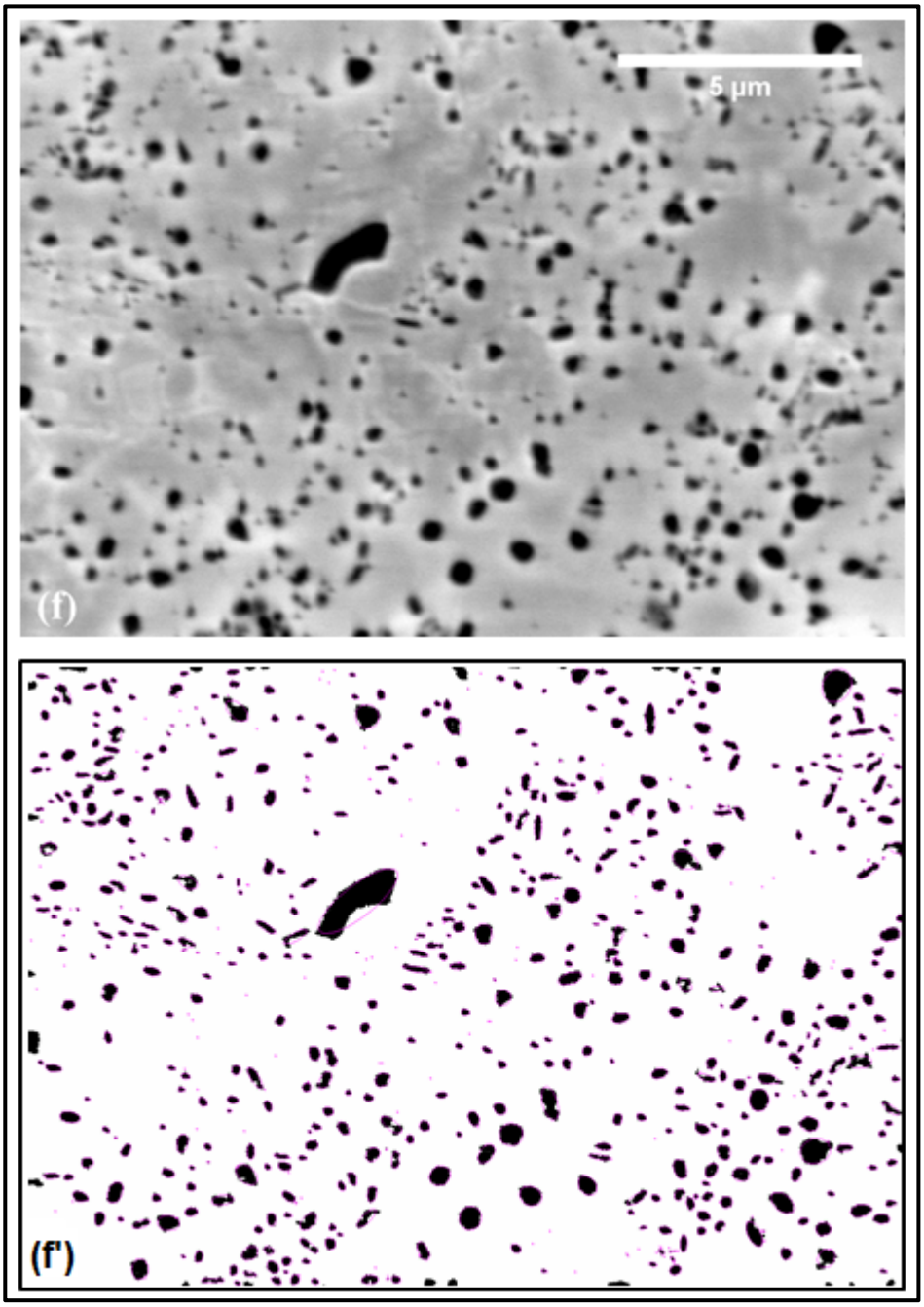

Figure 4-3 (continued) (g) (g′) at 923 K (650 °C) for 2900 min revealing by BASP etchant

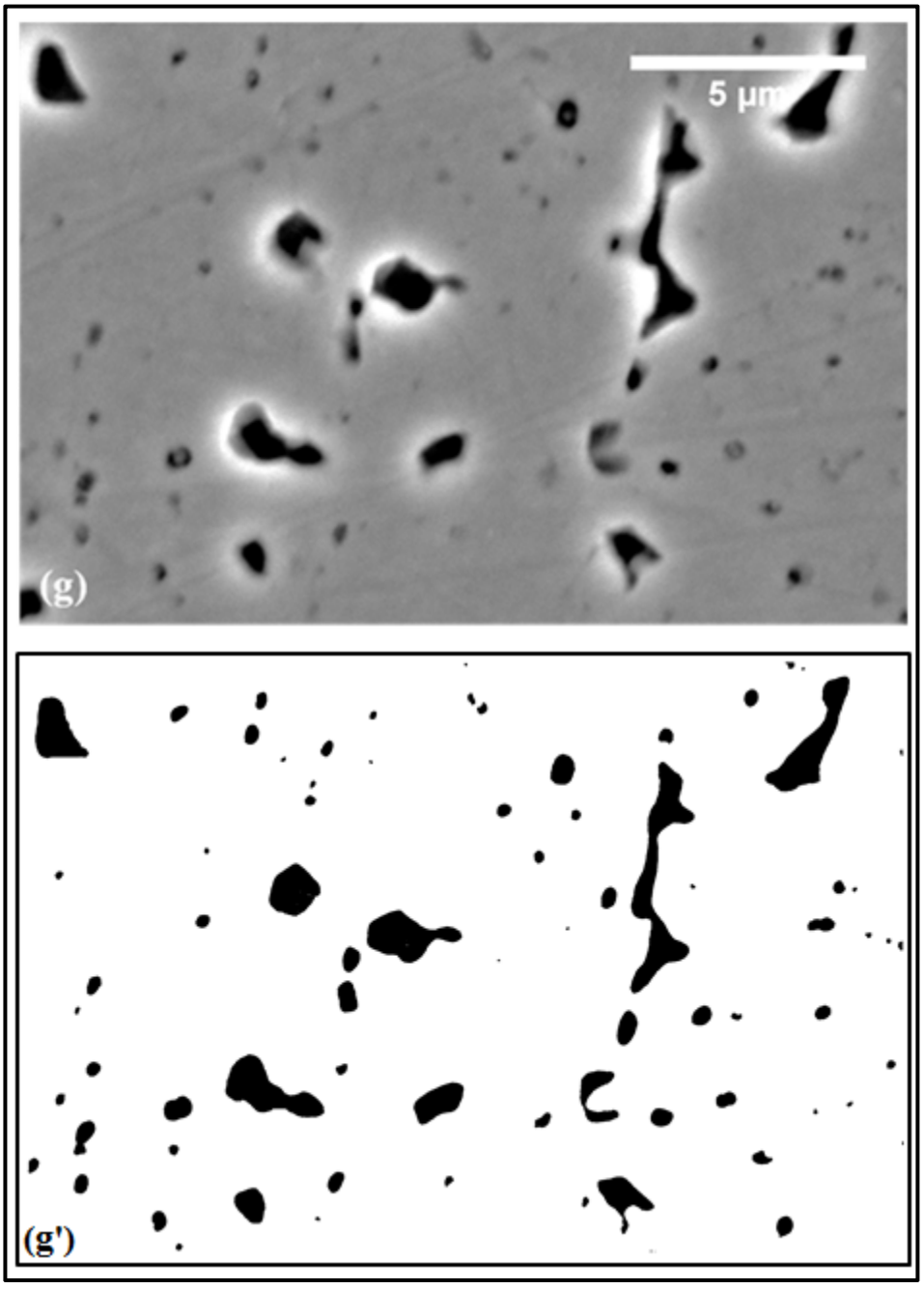

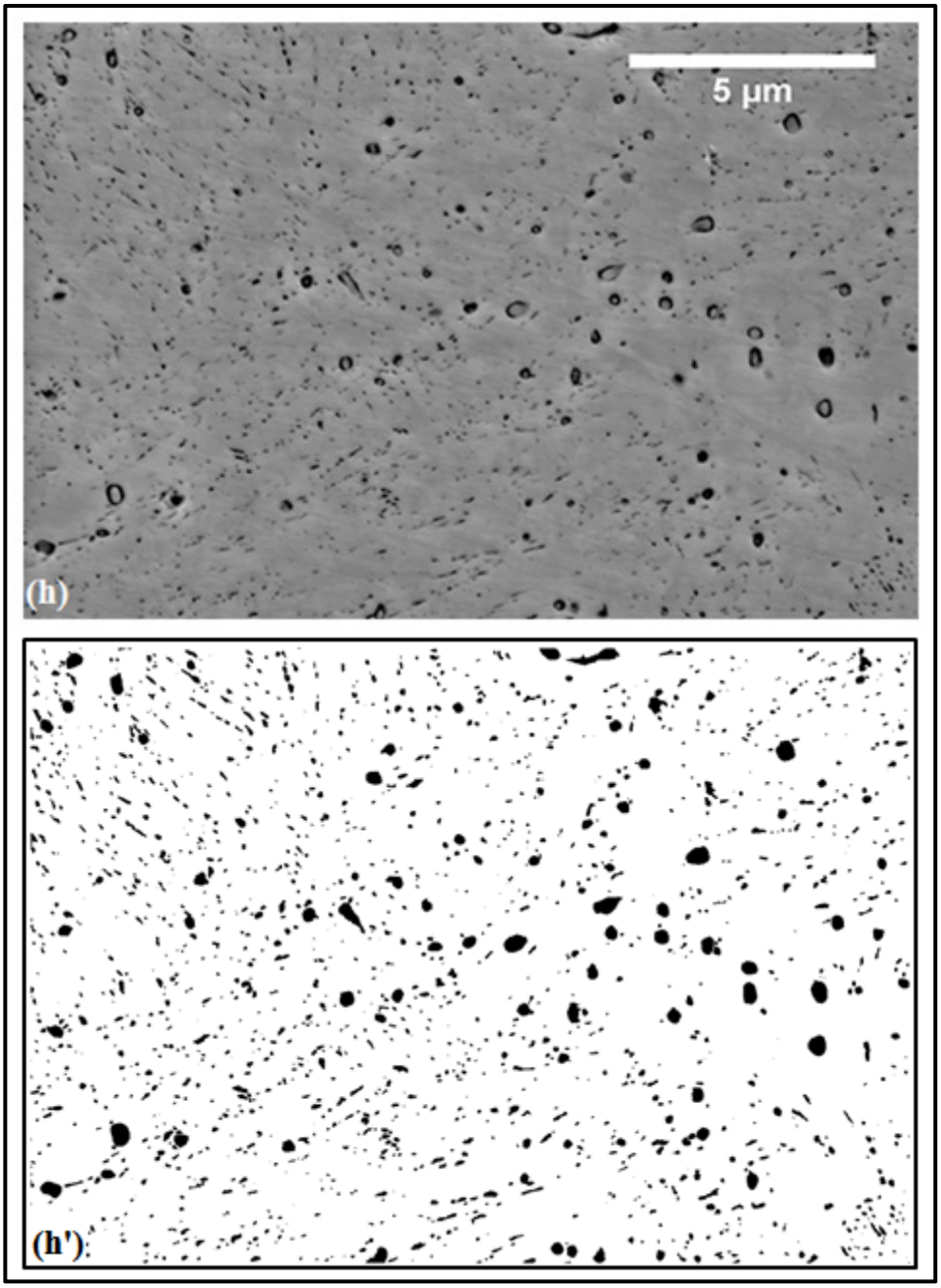

Figure 4-4 (h) SEM microstructure, and (h´) segmented black and white of tempered steel at 973 K (700 °C) and 5 min revealing by BASP etchant

Figure 4-4 (continued) (i) (i′) at 973 K (700 °C) for 12 min
revealing by BASP etchant

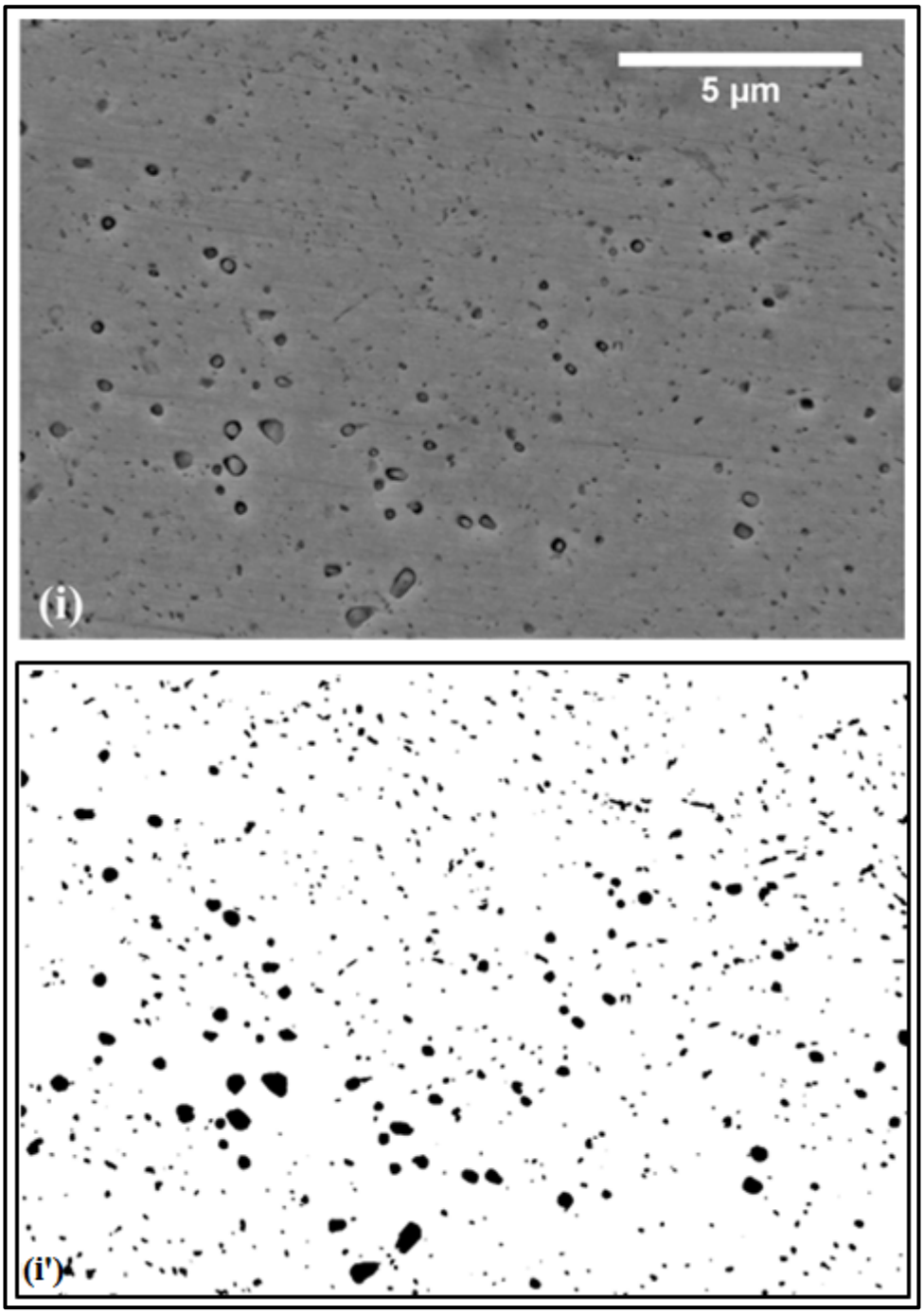

The average precipitate size increases significantly during tempering at 923 K (650 °C) as represented in Figure 4-5 (a). Similarly, the inter-particle spacing (λ) increases during tempering as shown in Figure 4-5 (b) which reduces considerably the efficiency of the precipitate as an obstacle for mobile dislocations. At a tempering temperature of 973 K (700 °C) the same phenomenon is observed during short tempering time, i.e. lower than 1000 sec. However, their variation is not significant by small steps of time duration. It means that mechanisms of strengthening loss probably operative due to limited number dissolution of smaller particles, and decrease in in-grain dislocation density, due to the recovery of dislocation substructure.

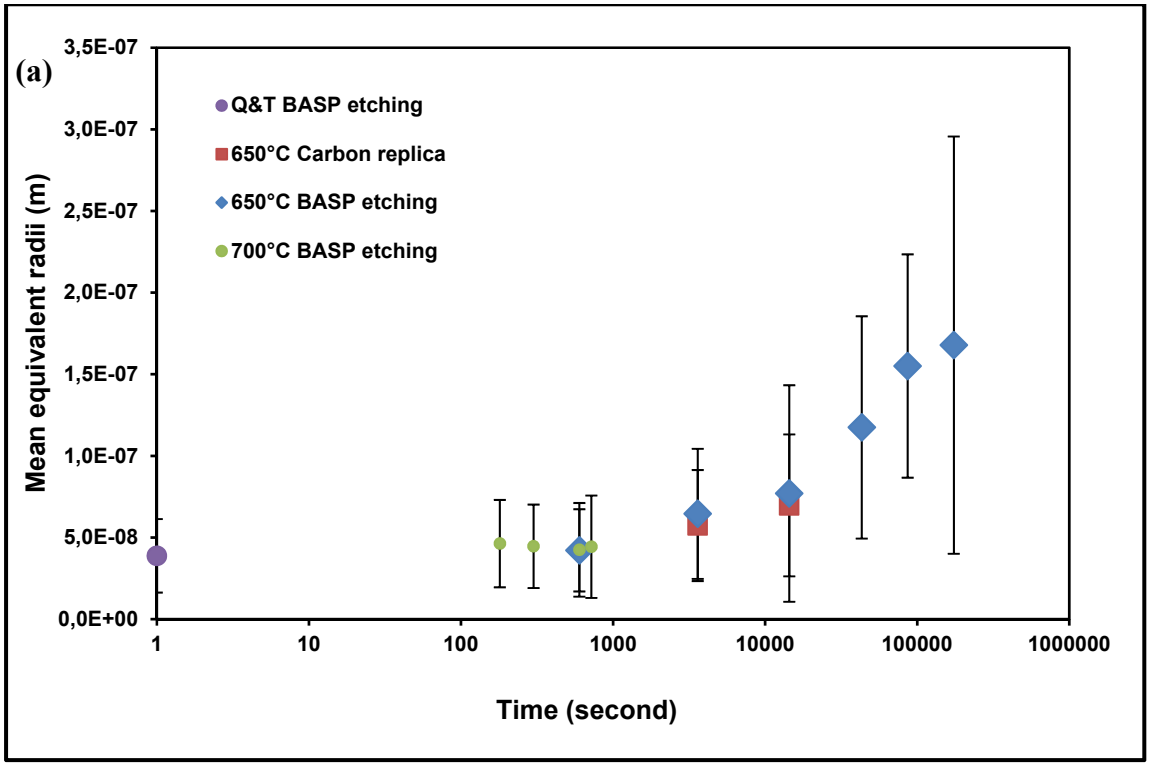

Figure 4-5 (a) The mean spherical equivalent radii evolution of precipitates, during tempering at 650 °C and 700 °C, extracted data by boiling alkaline sodium picrate (BASP) etchant and carbon replica methods.

Figure 4-5 (continued) b) inter-particle spacing λ (m)

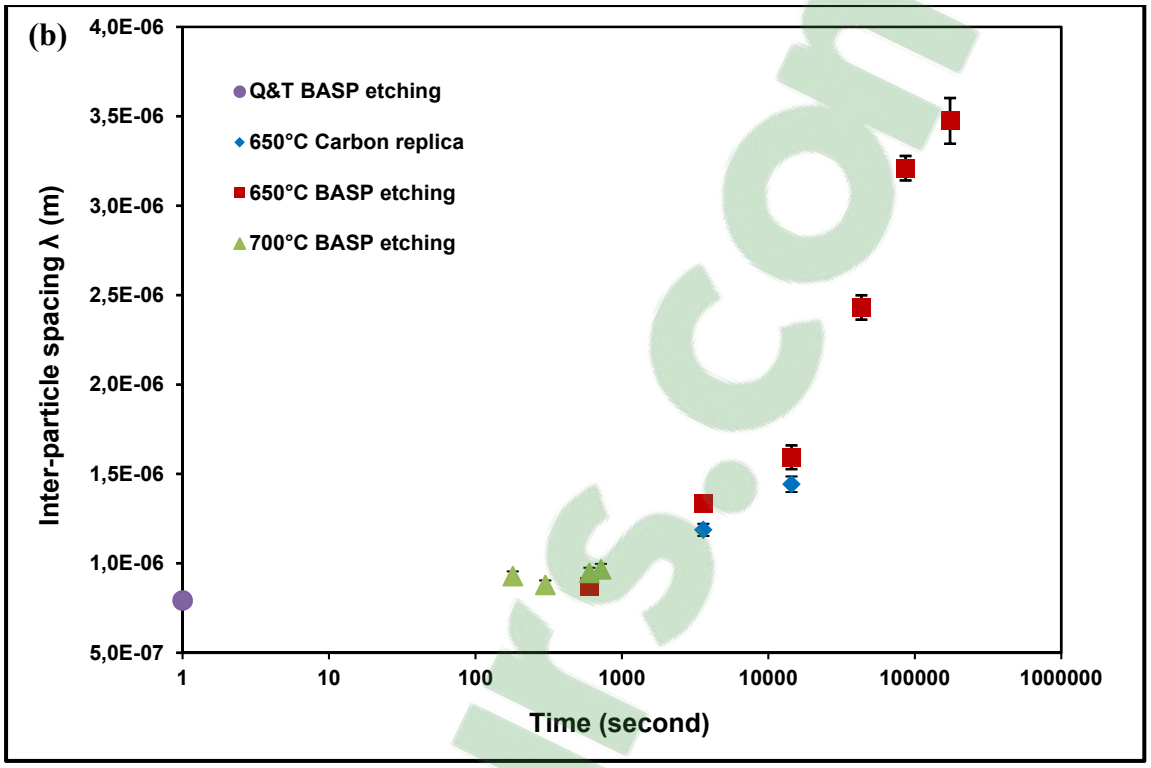

4.5 Chemical composition

Cementite extraction by electrochemical technique for dissolving the martensitic matrix was used to measure the alloying content of precipitates in substitutional elements, as they are the one driving the coarsening rate. XRD analysis confirmed that a large majority of the powder was cementite, the rest being formed by various oxides. Figure 4-6 present the spectrum XRD analysis of cementite powder after electrochemical reaction.

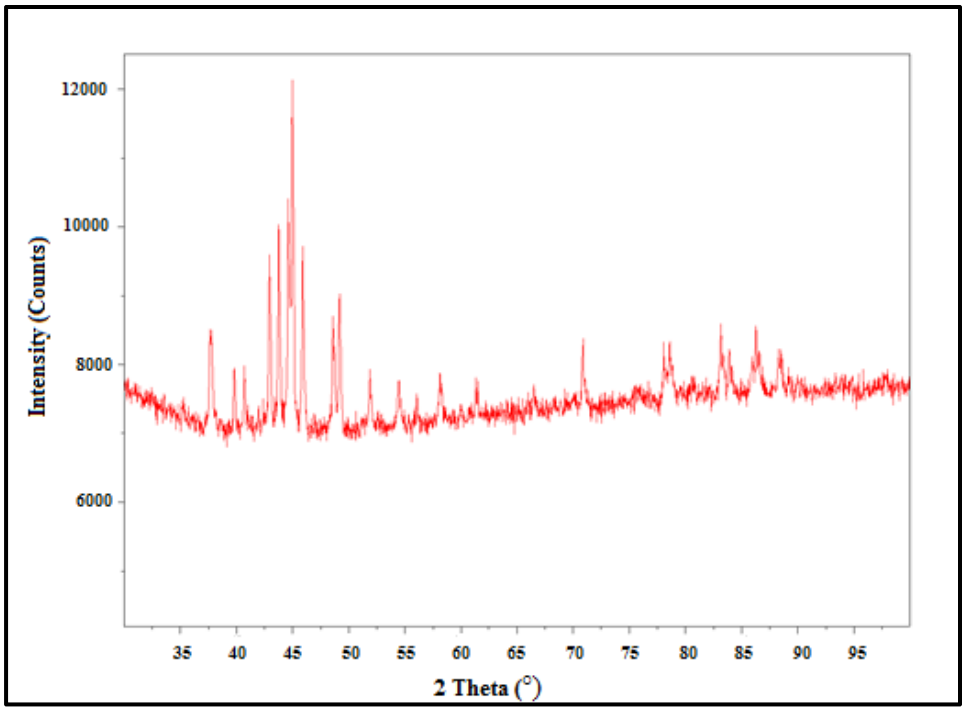

Figure 4-6 XRD analysis spectrum of 4340 steel powder after electrochemical extraction of precipitates.

The presence of alloying elements in the extracted carbides were determined on Q&T sample at 653 K (380 °C) and tempered again at 923 K (650 °C) for 10, 60, and 270 min by EDX analysis in a SEM as shown in Table 4-3. The high value of Cr, Mn, and Mo in quenched and tempered condition at 653 K (380 °C) could be because of secondary carbide forming as $M_{23}C_6$ or M_6C during austenitization, or annealing in the steel making process, which they are not soluble in austenite as well as in ferrite (Byeon and Kwun 2003). A gradual increase in cementite Cr and Mn fractions with tempering time is clearly observed. After tempering for more than 60 min, the measured fractions reach a fraction close to the equilibrium amount predicted by T-C calculations using TCFE7 database in Table 4-1, showing that thermodynamic stability have been reached in the measured precipitates. Moreover, Ni and Si could not be detected due to their low solubility in cementite. Finally, no Mo has been detected. The absence of Mo in cementite can be explained by its lower diffusion and

partition coefficient in tempered martensite compared to Cr and Mn, even at 923 K (650 °C) in this duration (Bhadeshia 1989).

Table 4-3 Illustration of chemical composition of alloying elements in different tempering condition by EDX analysis, (*) is not precise, (Δ) not detected.

Temperature, K (°C)	Time (min)	Fe	C	Cr	Mn	Mo	Ni	Si
Q & T	**-**	**71.83±3.6**	*	**10.27±0.66**	**2.49±0.22**	**11.52±0.68**	**2.97±0.23**	**0.92±0.06**
923 (650)	**10**	**90.83±1.29**	*	**6.1±0.54**	**3.06±0.25**	Δ	Δ	Δ
923 (〃)	**60**	**85.45±3.83**	*	**9.6±0.39**	**4.96±0.17**	Δ	Δ	Δ
923 (〃)	**270**	**85.08±1.6**	*	**9.89±0.43**	**5±0.12**	Δ	Δ	Δ

Furthermore, the carbon replica was used as a complementary method to confirm the existence of alloying elements partition in cementite. The spectra, shown in Figure 4-7 clearly demonstrate the presence of Cr and Mn in the precipitate composition at 923 K (650 °C) after 60 min (3600 sec). These two elements cannot diffuse on a long distance during the first tempering stage due to the lower tempering temperature 653 K (380 °C). However, they partition at 923 K (650 °C). As it will be discussed later, their partition rate plays an important role in the triggering of coarsening in AISI 4340 steel. Figure 4-8 also illustrates the element map analysis of extracted precipitates by carbon replica technique. Existence of Cr and Mn and even Mo can be evidenced in this analysis, but no detection of Ni and Si either in long time tempering as well as short time tempering were found due to their low solubility in cementite.

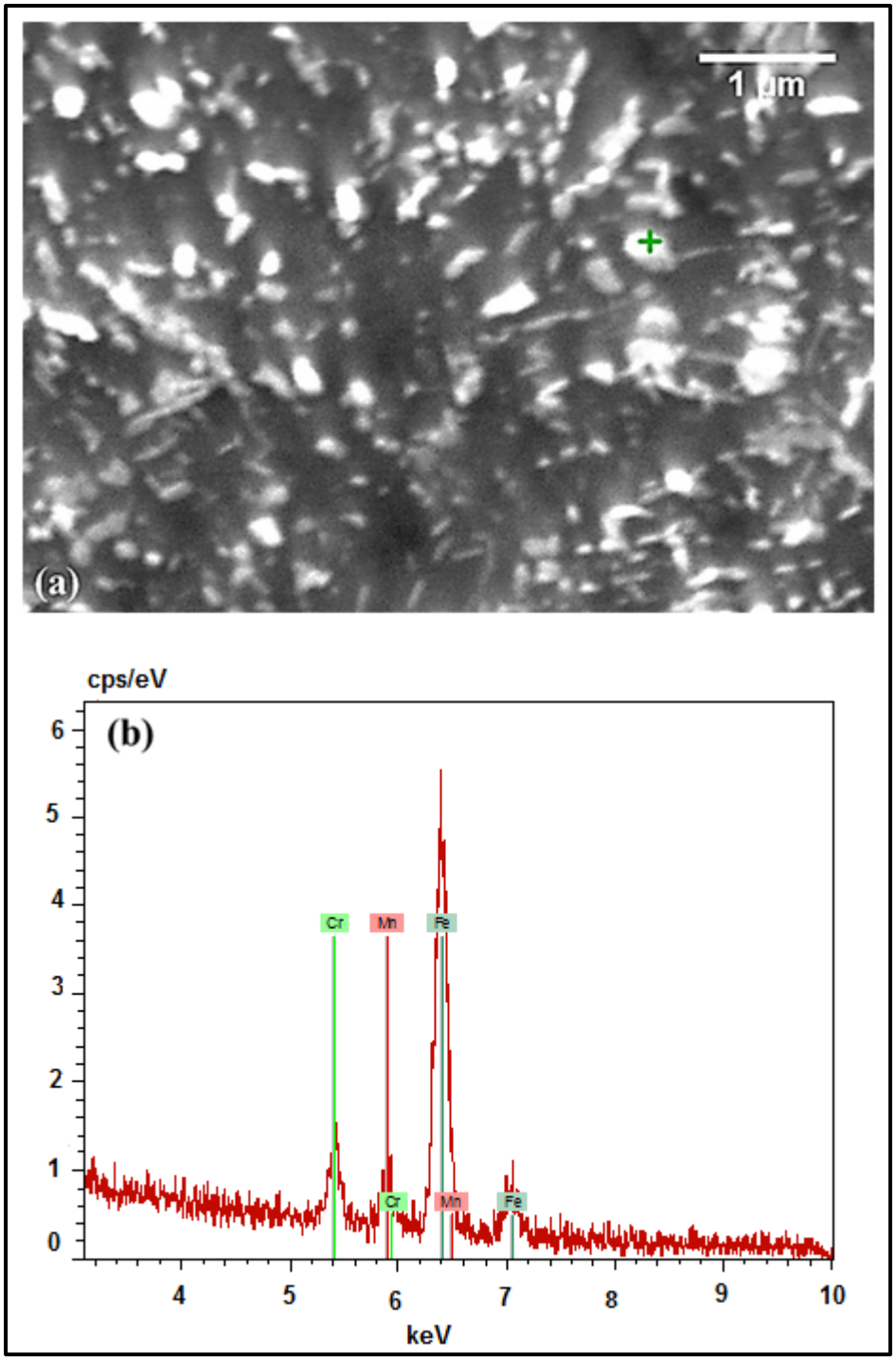

Figure 4-7 (a) SEM microstructure of extracted cementite particles by carbon replica method (bright particles) from sample tempered for 60 min at 650 °C (b) EDX spectrum

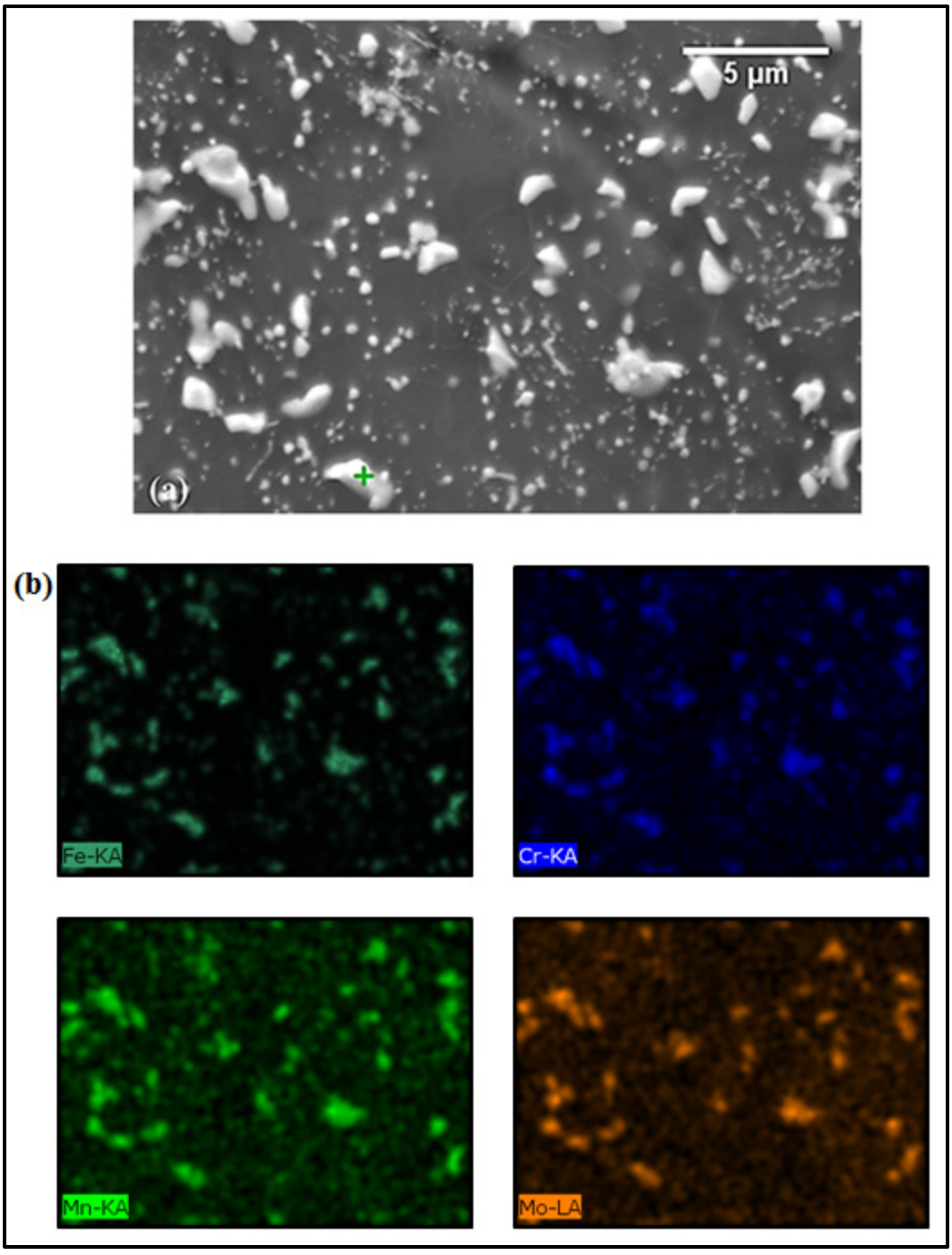

Figure 4-8 (a) SEM microstructure, and (b) map analysis of extracted cementite particles by carbon replica method (bright particles) from sample tempered for 1440 min at 650 °C

Figure 4-8 (continued)

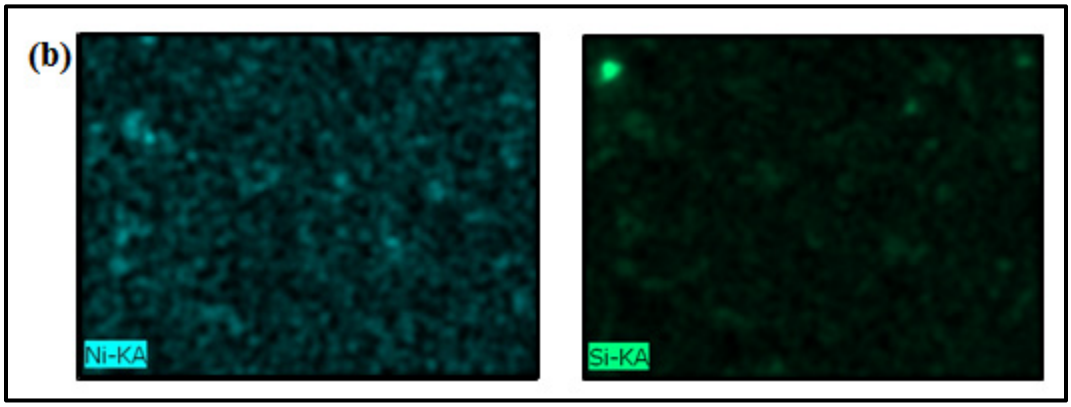

4.6 Morphology of precipitates

The extracted precipitates by replica technique and agglomerated powders of electrochemically extracted precipitates provide the morphology of cementite displayed in Figure 4-9 and Figure 4-10 respectively. The cementite morphology variation from needle to fine and then coarse spheroidal type is depicted in Figure 4-9 (a) to (d). The plate morphology is dominant among the smallest precipitates, at high magnification in Figure 4-10 (c).

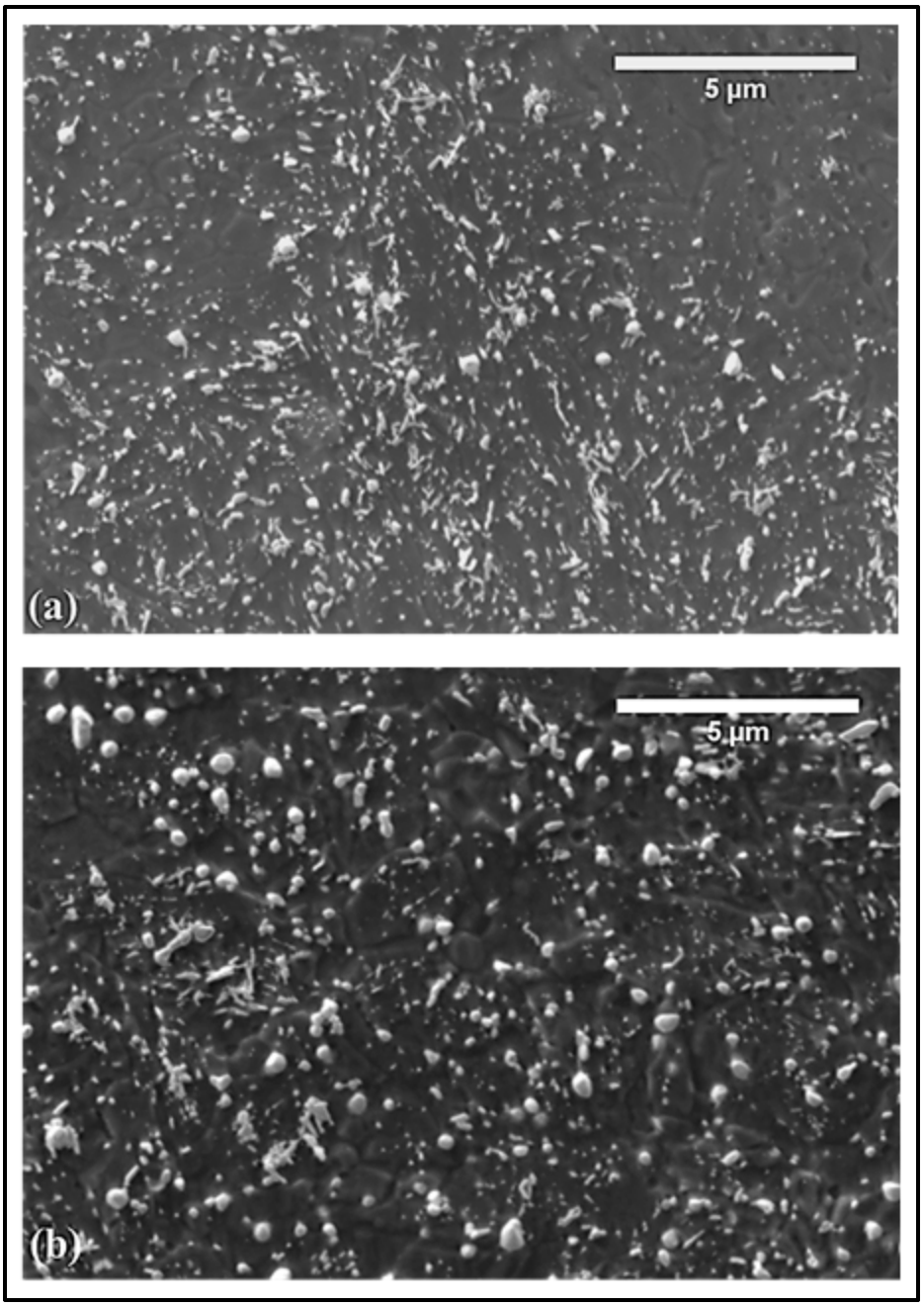

Figure 4-9 Illustration of extracted cementite particles by carbon replica technique from sample tempered at 650 °C at a) 60 min, b) 240 min

Figure 4-9 (continued) c) 720, d) 1440 min

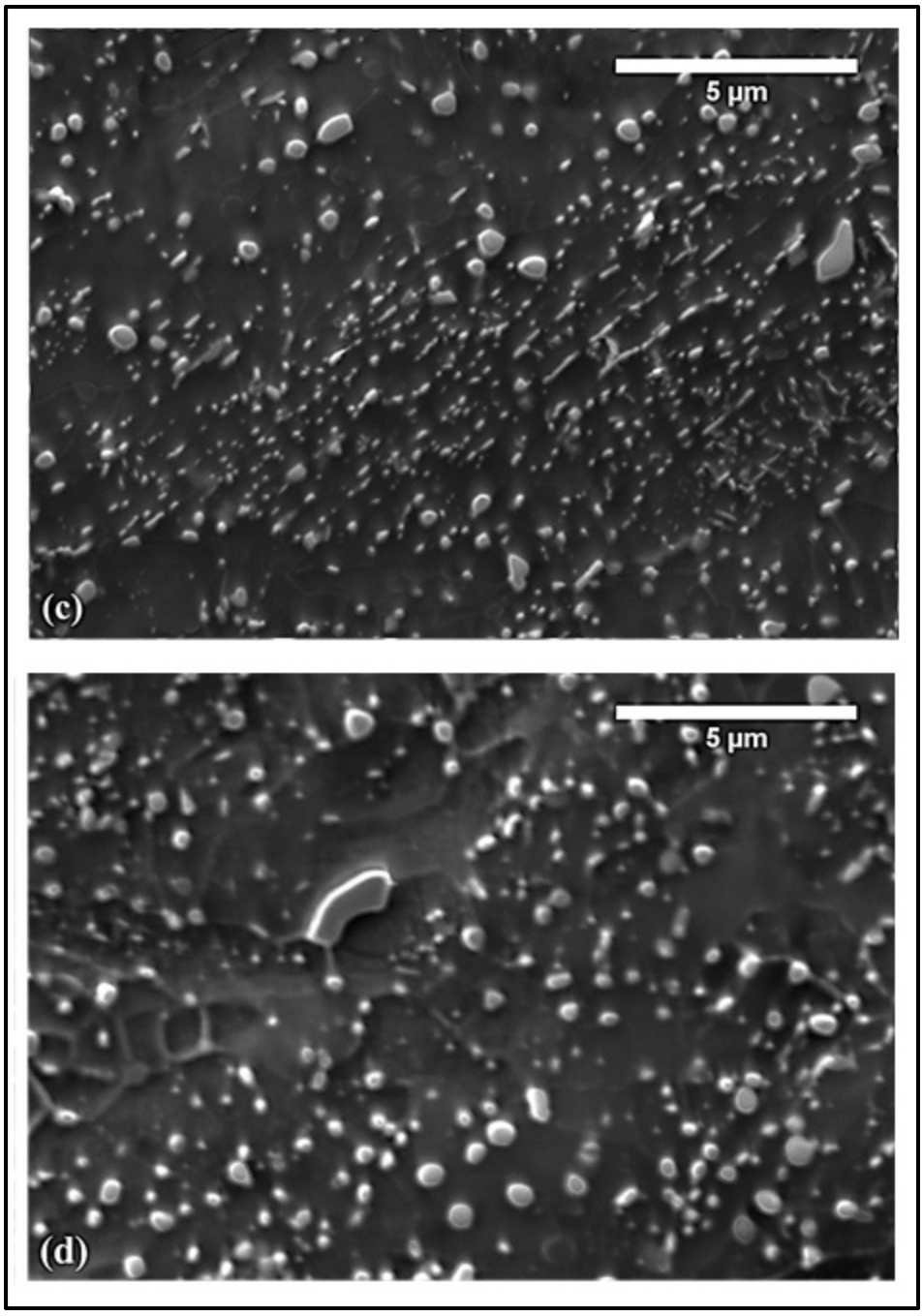

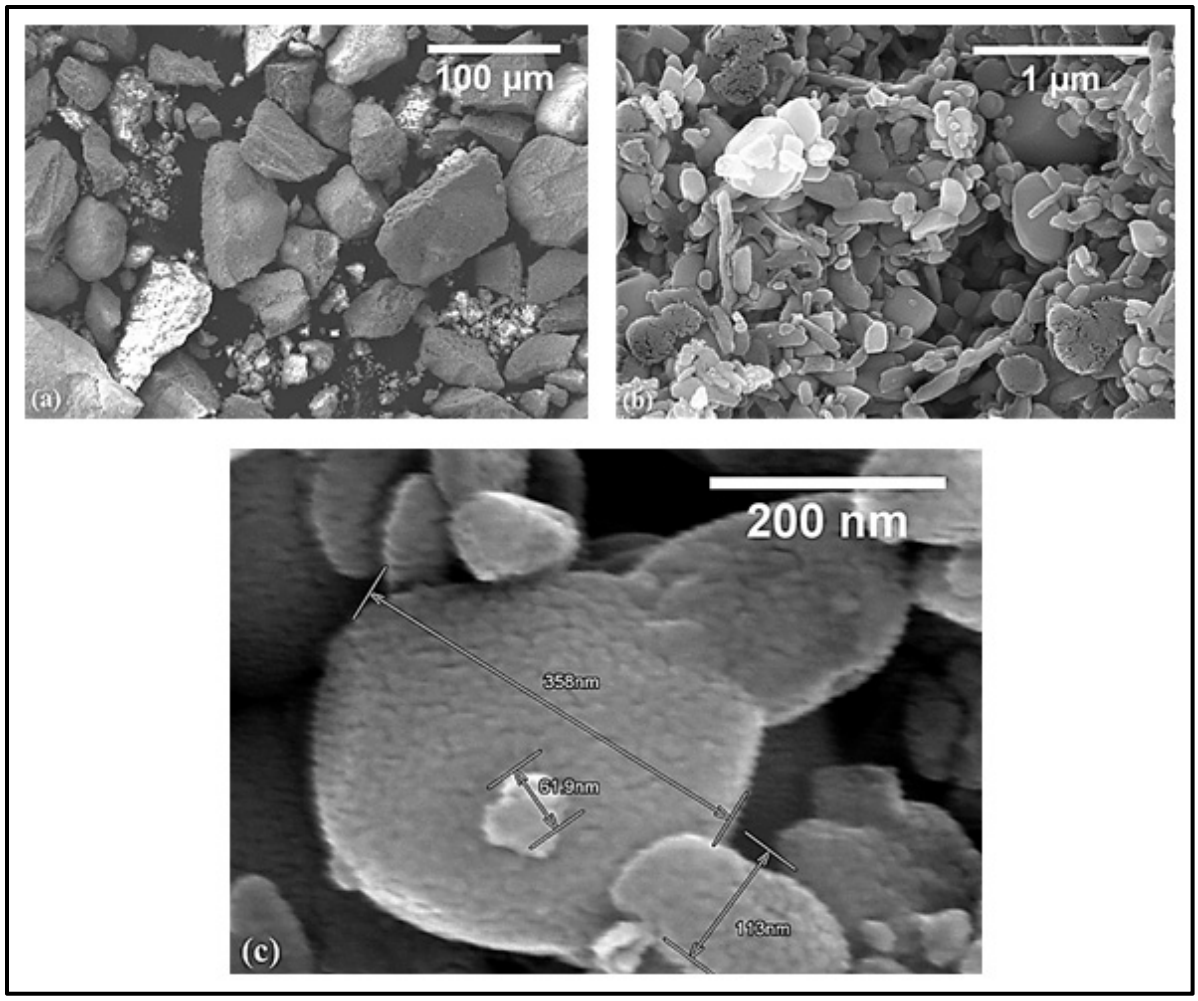

Figure 4-10 Illustration of extracted cementite particles by electrochemical reaction coated with gold from sample tempered at 650 °C and 480 min at different magnifications (a)×299, (b)×40,000 and (c)×200,000

The variation of precipitate morphology can be inferred by measuring the evolution of the average roundness of intercepted precipitates on micrographic section. Figure 4-11 displays how the roundness of precipitates changes during tempering at 923 K (650 °C) and 973 K (700 °C). At 923 K (650 °C), the measured apparent average roundnesses are almost constant (around 0.65) before 240 min (14400 sec) and increase significantly only after 720 min (43200 sec) tempering to reach values close to 0.75. It is relevant to note that carbon replica

and metallographic sections show reasonable agreement although the variations are more marked on metallographic sections.

However, after 2900 min (174000 sec) of tempering at 923 K (650 °C), the precipitates exhibit a tendency to coarsen or thicken with irregular shapes, preventing the roundness to increase to 1, that of a perfect sphere. This phenomenon was also reported by Lee and Allen (Lee and Allen 1991).

Spherical roundnesses (higher than 0.7) (Lv, Wang et al. 2013) are attained for the majority of precipitates after 240 min (14400 sec) tempering at 923 K (650 °C). This corresponds to an average critical precipitate size of about 77 nm. This critical size corresponds well to the phenomenon of substitutional species Cr and Mn reaching their solubility limit in the matrix. This is a well-described behavior of such precipitates reported first by Zener (Hillert 1986). The change in roundness is consistent with the counterpart saturation of Cr and Mn in cementite shown in Table 4-3. At 973 K (700 °C), the measured apparent average roundnesses are almost constant (around 0.65) before 10 min (600 sec) and increase only at 10 min (600 sec) tempering to reach values close to 0.7.

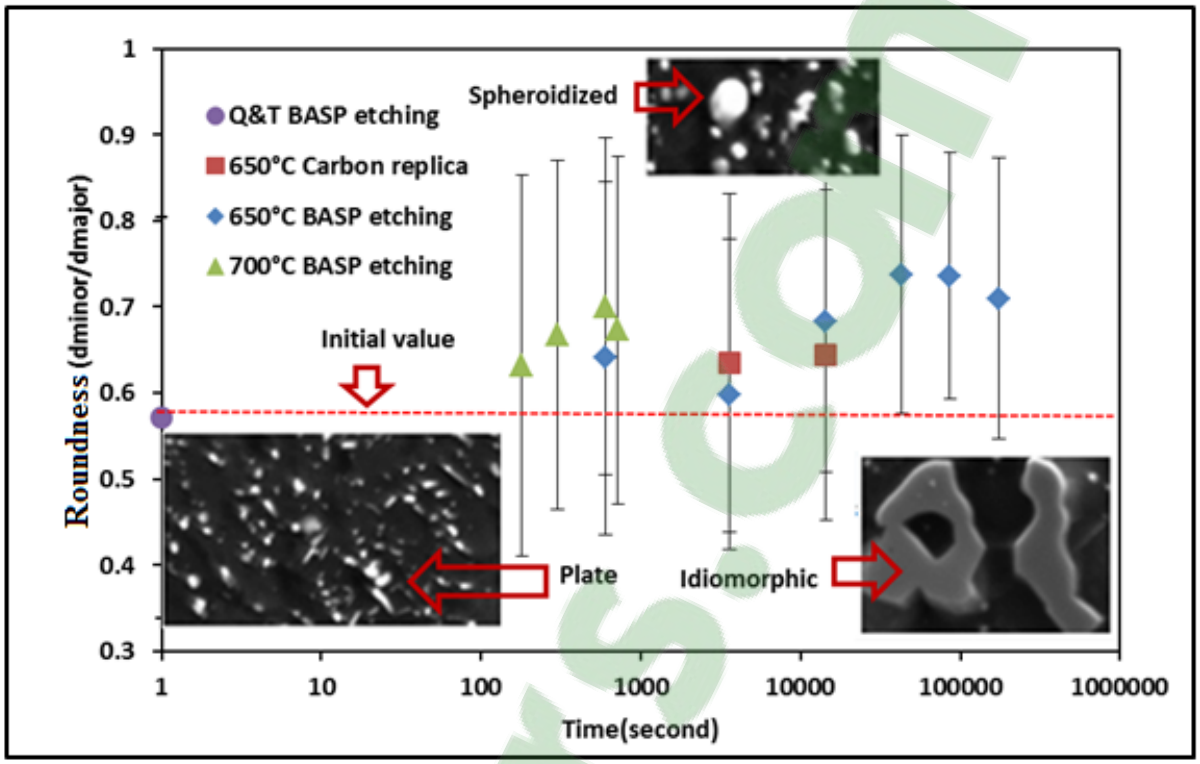

Figure 4-11 Roundness variation of precipitates extracted by BASP etching method and extraction replica during tempering at 650 °C and 700 °C.

4.7 Number density

The other important property that characterizes the microstructural evolution is the number density of precipitates. Figure 4-12 presents the overall number density evolution of precipitates with tempering time. It shows a reduction in number density with tempering. The gradual decrease in number density of precipitates at constant volume fraction during tempering is very typical of coarsening. This reduction is not significant after 60 min (3600 sec) of tempering at 923 K (650 °C), showing that AISI 4340 exhibit rather good softening resistance, until almost critical size for spheroidization is reached. The variation of number density is quite small at 973 K (700 °C) for short duration.

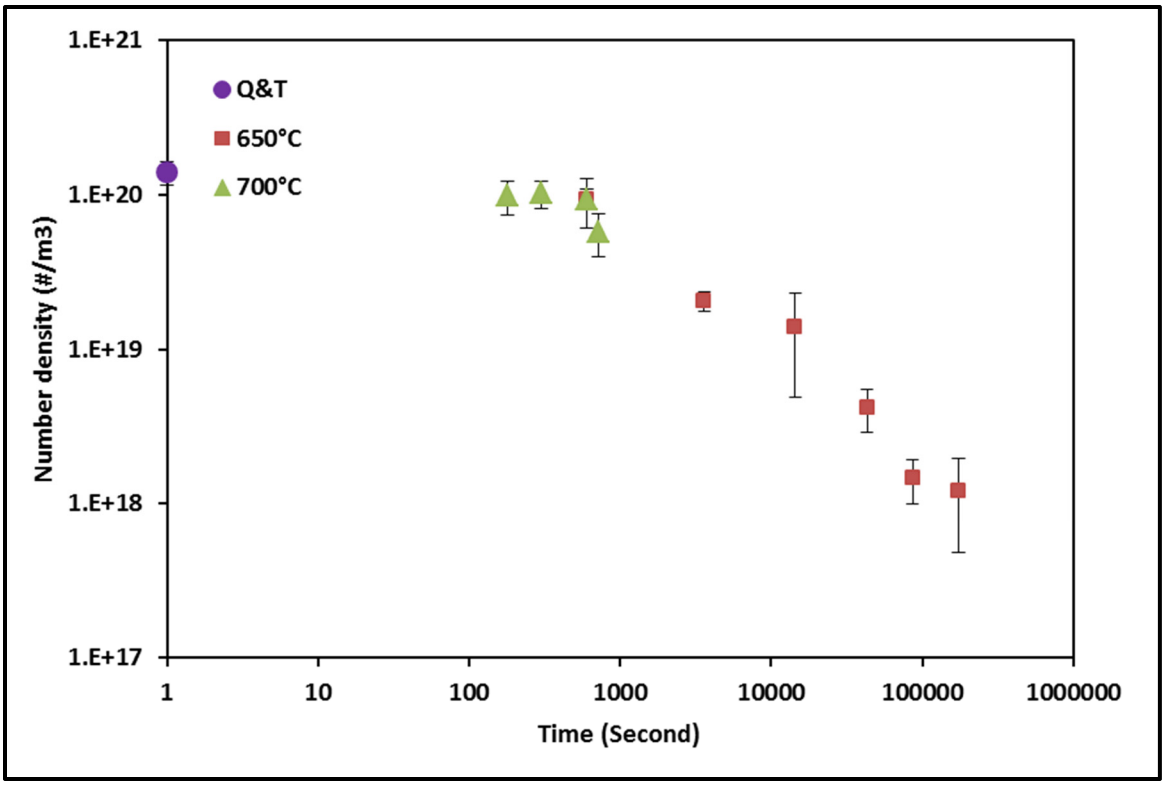

Figure 4-12 Number density variation of precipitates during tempering at 650 °C and 700 °C, extracted data by boiling alkaline sodium picrate (BASP) etchant, the error bar is calculated based on standard deviation of the mean precipitate size

4.8 LSW distribution

When Ostwald ripening is the operative mechanism for tempering, the initial precipitate size distribution in the limit of low phase fractions can classically be described by the theoretical Lifshitz-Slyozov and Wagner (LSW) steady-state distribution (Tiryakioğlu, Ökten et al. 2009). The mathematical derivation of the LSW distribution assumes negligible volume fractions. A characteristic of this distribution is that no precipitates have a size larger than 1.5 times the mean spherical radius (Lee, Allen et al. 1991). In order to derive the volume distribution from the experimental data that consists, in raw form, of surface density, the Saltykov coefficients stereological method was used. The Saltykov method allows the

volume size distributions, Nv to be calculated from the surface particle size distributions that are directly measured on sectioned metallographic sample (Underwood 1970).

It is important to note that even though the precipitates are plate shaped, a spherical equivalent radius has been assumed in order to comply with the Saltykov method prerequisites, which introduces a bias in the analysis. Figure 4-13 represents the normalized precipitate size distributions (PSD) at 923 K (650 °C) for various times of hold in order to compare with the corresponding LSW distribution function. The LSW distribution agrees with the described experimental distributions only for the average sizes (Vedula and Heckel 1970).

In all conditions, the experimental distribution presents a fraction of large particles that cannot be explained by LSW theory, although only a marginal fraction of precipitates, about 10 % overpass this limit. The assumption of spherical precipitates made in the derivation of the experimental distributions is thought to be responsible for this discrepancy, as well as the non-negligible volume fraction of cementite precipitates in martensites. However, modified LSW theories, compiled by Baldan (Baldan 2002) cannot explain the discrepancies observed here with a modest volume fraction of about 6.0%. It is expected that those discrepancies will account for slightly larger confidence intervals when comparing experimental radii to modeling data.

4.9 Coarsening constant (K)

In order to estimate the rate of coarsening K, the average volume evolution of precipitates as the function of tempering duration at 923 K (650 °C) has been plotted in Figure 4-14. Equation (1.2) has been used to model the experimental data points, and a value of 2.83 $\times 10^{-26}$ ($m^3 \times sec^{-1}$) at 923 K (650 °C) has been found for the coarsening rate K, and 66 nm for r_0 at the onset of coarsening. i.e. condition for which spheroidization is almost achieved.

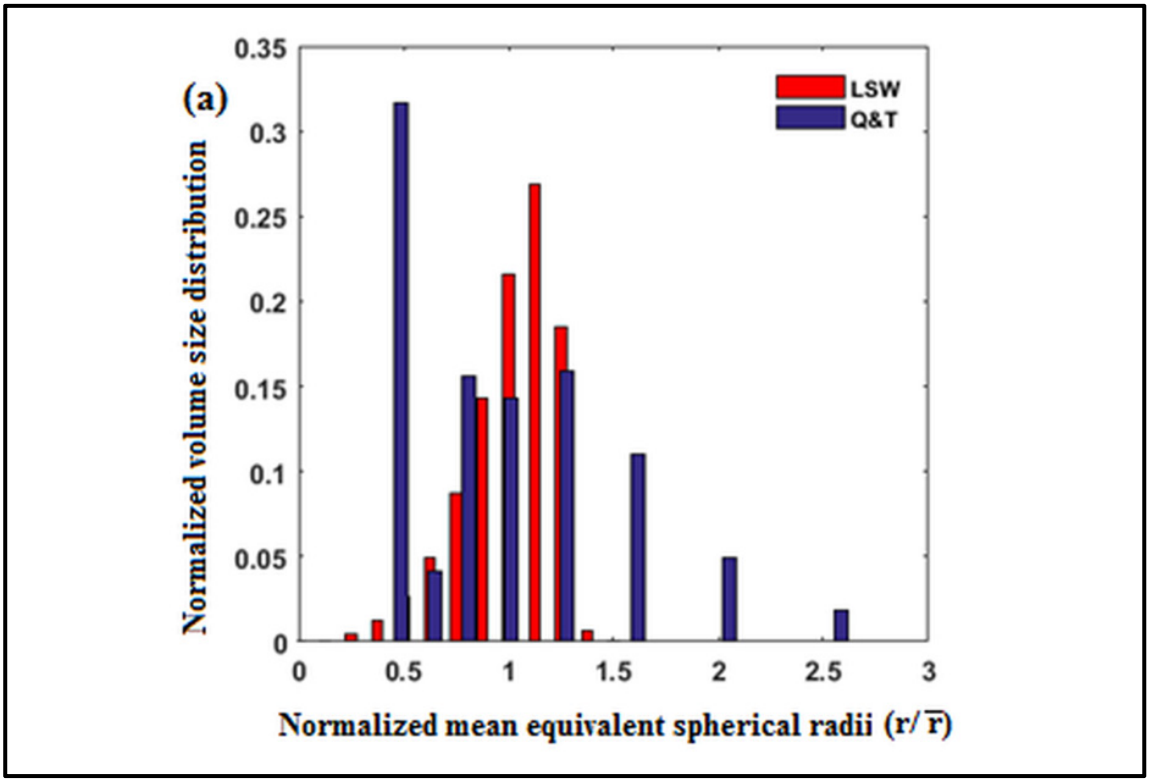

Figure 4-13 Normalized size distribution curves calculated by Saltykov methods from the experimental data assuming precipitates of spherical shapes extracted by BASP etchingof AISI 4340 steel during temperingat 650 °C, compared with the corresponding steady state size distribution predicted by Lifshitz-Slyozov and Wagner (LSW) theory a) Q&T

Figure 4-13 (continued) b) 10 c) 60

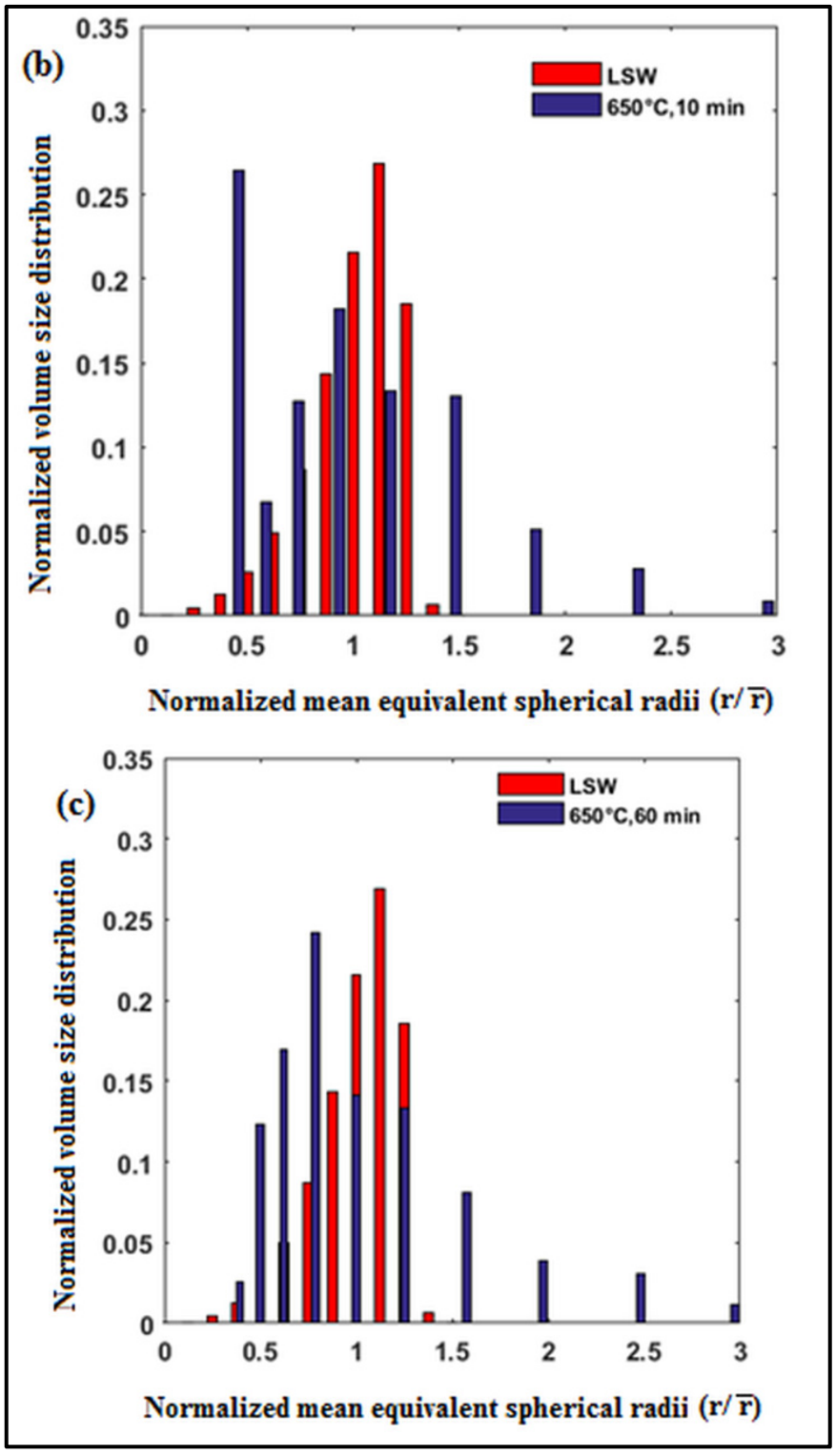

Figure 4-13 (continued) d) 240, e) 720

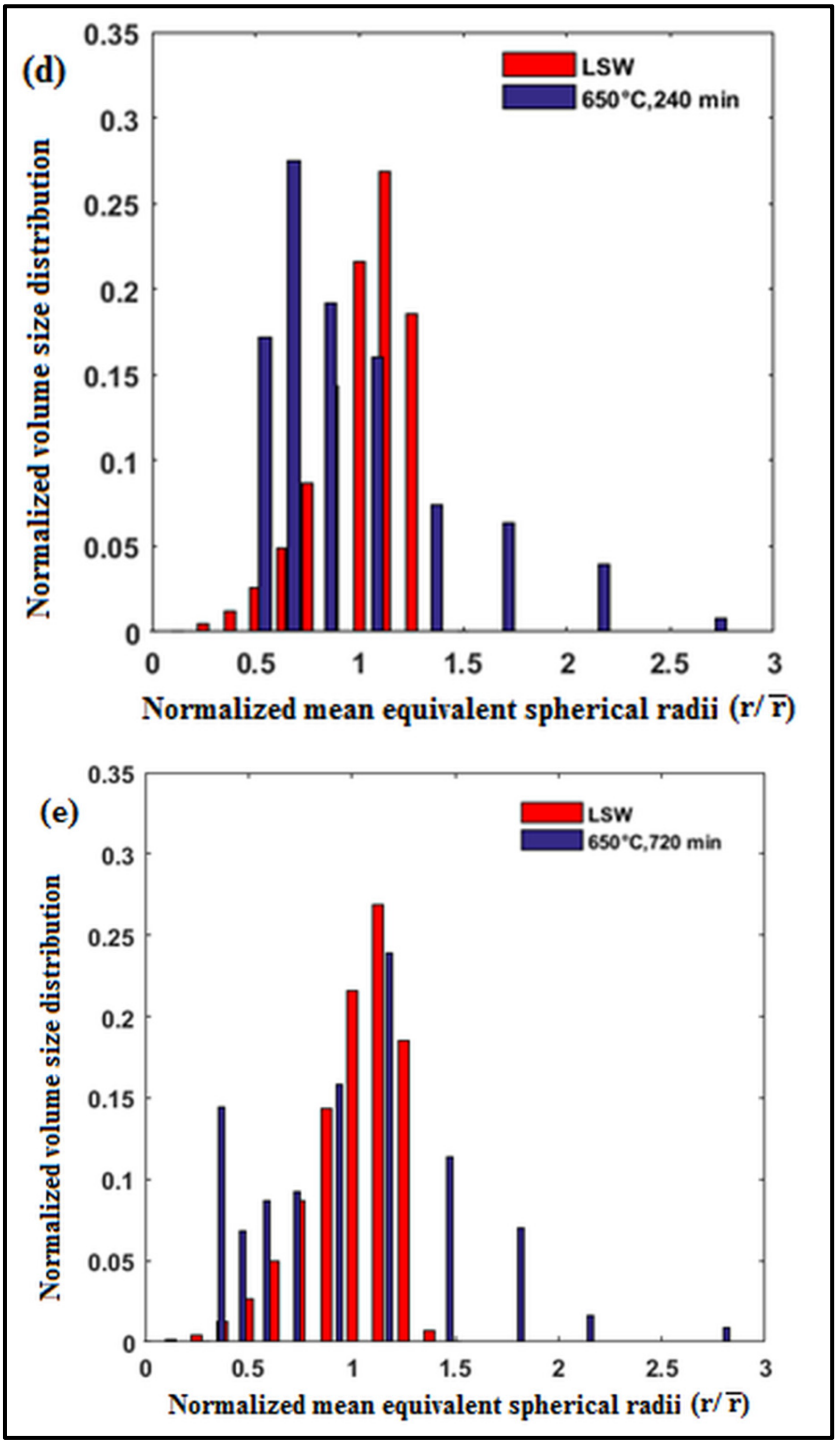

Figure 4-13 (continued) f) 1440, g) 2900 min

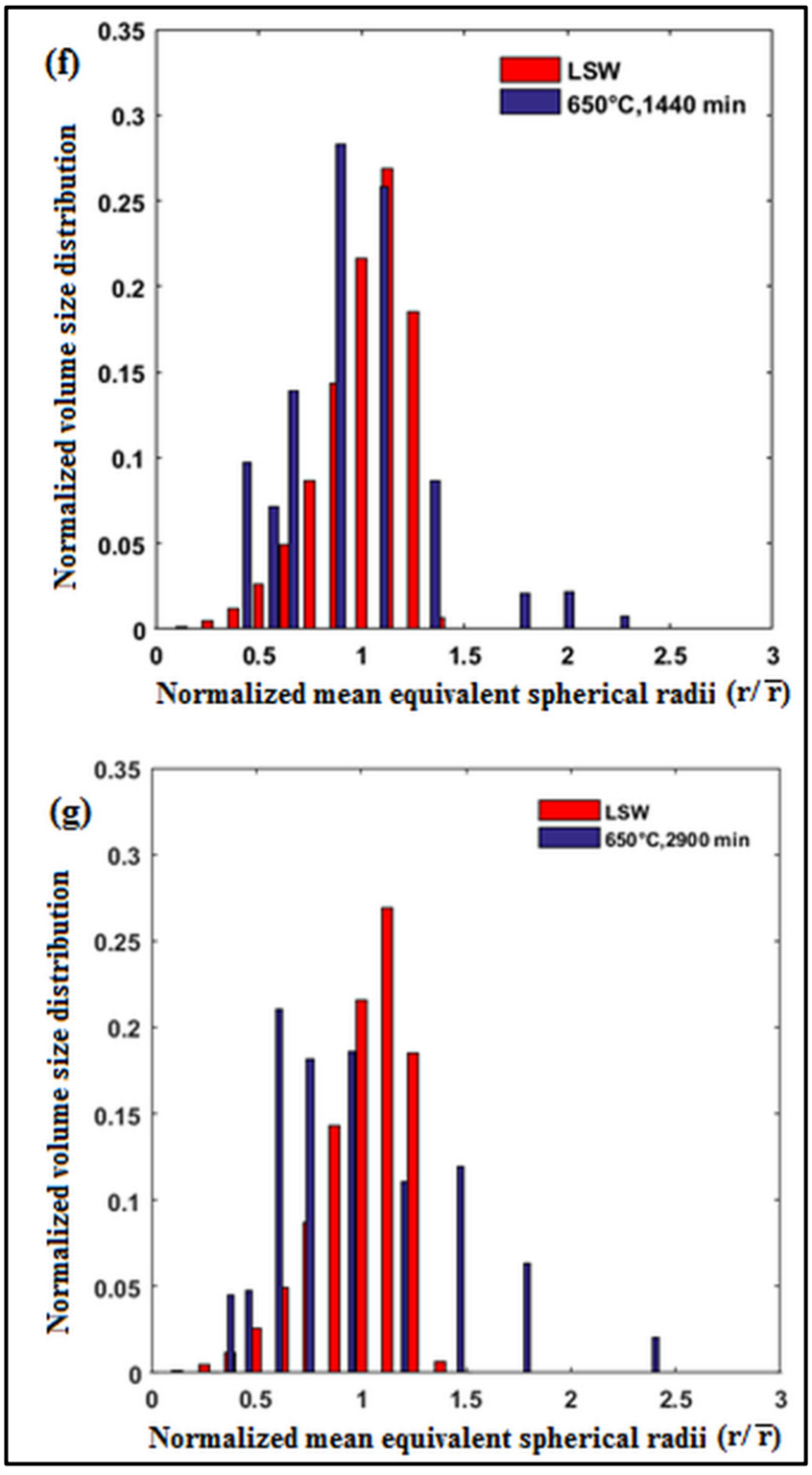

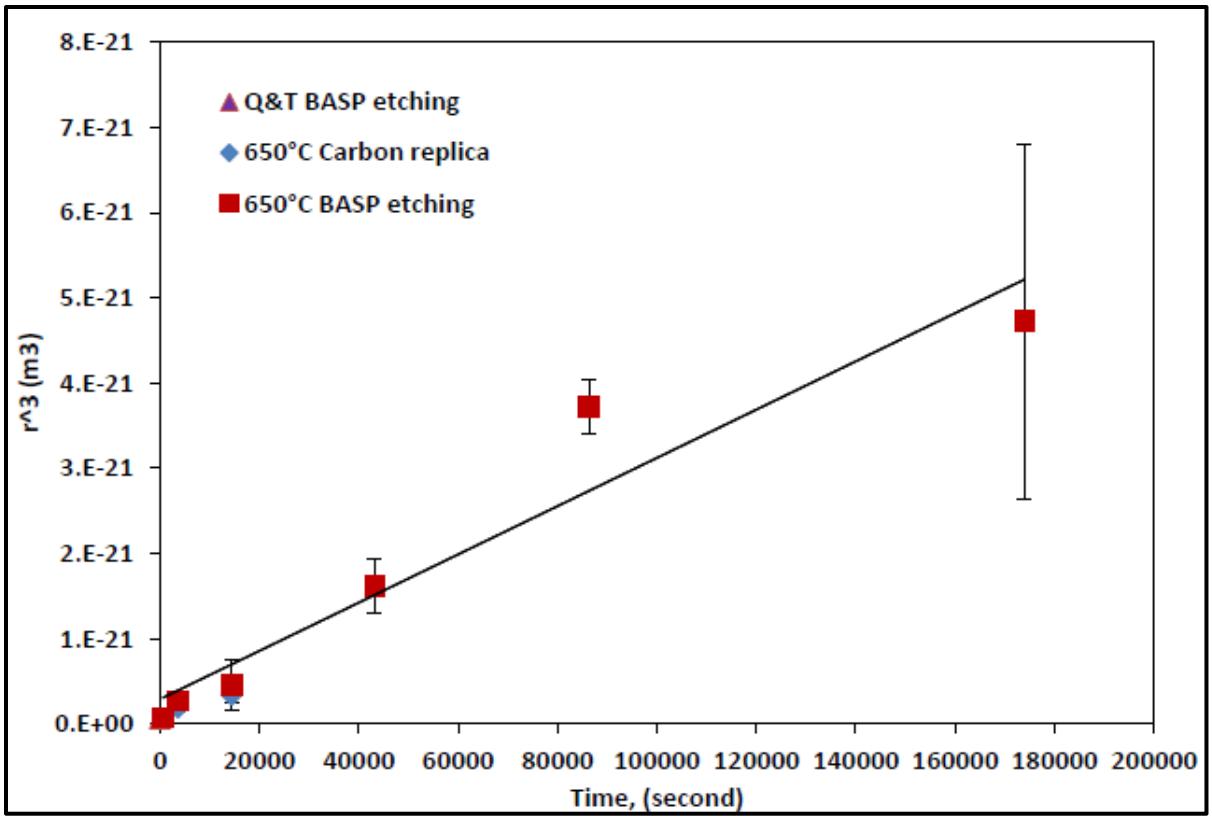

Figure 4-14 The precipitates volume evolution versus time, extracted data by boiling alkaline sodium picrate (BASP) etchant and carbon replica methods tempered at 650 °C, the equation related to the best linear fit is $\boldsymbol{r^3 = 2.83 \times 10^{-26} \times t + 2.91 \times 10^{-22}}$

4.10 Ardell method evaluation

According to the work of Ardell, in the condition of LSW assumption, further insights on the precipitation process can be gained from plotting $N_V \times t^{\frac{4}{3}}$ against $t^{\frac{1}{3}}$ and a linear relationship is expected as a consequence of the three dimensional nature of the precipitate growth and the diffusion field (Ardell 1997). The slope (A) and the intercept (B) of the regressed line were found to be $A_{exp} = 2.151 \times 10^{23} \pm 1.063 \times 10^{23}$ $(\#m^{-3}\text{sec})$ and $B_{exp} = -1.53 \times 10^{24} \pm 4 \times 10^{24}$ $(\#m^{-3}sec^{\frac{4}{3}})$ as displayed in Figure 4-15. The A_{exp} value can be compared with its theoretical expression provided in Eq.10 from ref (Ardell 1997).

Using the present Thermo-Calc values A_{th}=4.52×10^{23} ($\#m^{-3}$sec) and is within the same order of magnitude but out of the experimental confidence internal. This still provides a relatively good agreement between the theory and experimental data (Ardell 1997). The evaluation of the B_{th} value using Eq.11 from ref (Ardell 1997) is not straightforward and will not be developed here, furthermore as the confidence interval obtained experimentally is rather large.

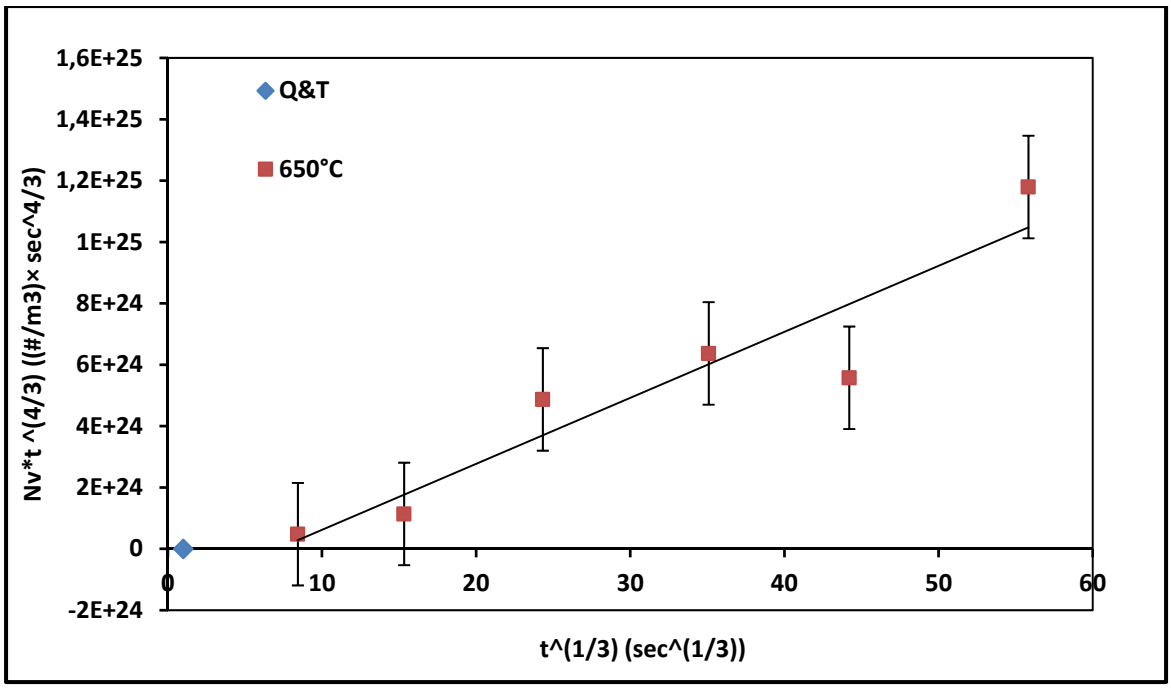

Figure 4-15 Evolution of the volume density with tempering duration, see reference (Ardell 1997) for further details, the standard error of data are indicated as error bar. The equation related to solid line represent the best linear fit is

$$N_V \times t^{\frac{4}{3}} = 2.151 \times 10^{23} \times t^{\frac{1}{3}} - 1.53 \times 10^{24}$$

4.11 **Summary**

In summary, the hardness property of representative samples is measured. The chemical composition of cementite and matrix are calculated by Thermo-Calc software. The microstructural investigation is performed to yield measurement such as the average precipitate radii, volume fraction, roundness, as well as quantities derived from the former mean inter-particle distance, number density, and size distribution of cementite particles. The chemical composition and morphology of cementite are investigated by different techniques. The rate of cementite coarsening during tempering at 923K (650 °C) is estimated by using linear fit with experimental data.

CHAPTER 5

MODELING THE KINETICS COARSENING OF CEMENTITE

5.1 Introduction

Modeling the kinetics coarsening of cementite based on thermodynamics and kinetics aspect for multicomponent alloyed AISI 4340 steel by Thermo-Calc and DICTRA software is the main concern of this chapter. The extension of Björklund model is also used to validate DICTRA model result. At the end, the hardness of samples representing over-tempered area is calculated by using microstructural features.

5.2 Background

The theory of coarsening due to diffusive interaction in alloy system, also called Ostwald ripening, has been established for several decades. However obtaining reliable predictions for multicomponent systems remains a quantitatively complex process (Martin, Doherty et al. 1997). Difficulties arise mainly from the non-ideality of actual alloy system, especially martensitic steels that contain a large variety of nucleation sites for precipitates, a large number of species that partitions to cementite with different rates, notwithstanding the fact that cementite undergoes shape changes associated with coarsening (spheroidization). In addition, due to the high density of dislocations resulting from lath martensite formation, dislocation hardening forms a secondary source of hardness. The recovery of the dislocation substructure may thus play a secondary role on hardness loss, however this study focuses only on the over-tempering effect of tempered martensite through the precipitates coarsening. In the simplest (for instance binary) alloy systems the rate of diffusion controlled coarsening of spherical cementite can be described by the following equation (5.1) (Lee and Allen 1991) (Porter and Easterling 1992):

$$\overline{r^3} - \overline{r_o'^3} = K.t \qquad (5.1)$$

where r is current mean radius and r_o is the initial mean radius at the onset of precipitate coarsening, assumed spherical, t is the holding tempering time at the temperature T, and K(T) is the coarsening rate constant defined in equation (5.2) as:

$$K = \frac{8\sigma V_m^{\theta}}{9RT} D C_e \tag{5.2}$$

where σ is the martensite-cementite interfacial energy, V_m^{θ} is the molar volume of the growing phase, C_e is the equilibrium solute concentration (here, carbon), D is the diffusion coefficient of the species controlling the growth rate and R the universal gas constant (Björklund, Donaghey et al. 1972) (Porter and Easterling 1992).

In the case of multicomponent systems, the rate constant equation must be modified to include the influence of all alloying additions. Björklund et al. 1972 suggested that when r reaches large values (i.e. for large precipitate sizes), slow diffusing substitutional alloying elements control the coarsening rate and determine the value of the rate constant in the coarsening equation. The rate constant will then be proportional to the quantity $(k_i - 1)^{-2}$, where k_i is the partition coefficient of species i between the precipitating cementite (θ) and the matrix phase (α) i.e. $(k_i = \frac{C_i^{\theta}}{C_i^{\alpha}})$

However, Björklund et al. equation is restricted to dilute solutions and they did not take into account the effect of the interfacial curvature on matrix compositions (Lee, Allen et al. 1991, Kuehmann and Voorhees 1996). i.e. the Gibbs-Thomson effect. A refined approach by Umantsev and Olson 1993 for multicomponent system takes into account concentrated solutions (non-dilute), but considers the effect of precipitate interfacial curvature as negligible. Voorhees et al. 1996 built-up a theory valid for chemically non-ideal and non-dilute ternary alloys that includes capillarity. For ternary systems, the influence of substitutional alloying element A on the coarsening rate constant can be described by equation (5.3) considering partition process effect:

$$K = \frac{8\sigma V_m^{\theta}}{9RT} \left(\frac{C_A^{\alpha}(1-k_A)^2}{D_A} + \frac{C_B^{\alpha}(1-k_B)^2}{D_B} \right)^{-1} \tag{5.3}$$

Adding other alloying elements influences the coarsening rate of the precipitate distribution through its partition coefficient, as well as its diffusivity. Therefore, if an alloying addition has a significantly lower diffusivity compared to carbon (for example substitutional elements like Cr, Mn, Mo, Ni, Si), even small additions of the later can yield significant differences in the rate constant. On the other hand, if the element does not partition preferentially in either the matrix or the precipitates, i.e. $k_B \rightarrow 1$, little influence on the coarsening kinetics is to be expected (Kuehmann and Voorhees 1996). It is thus a rather complex interplay between the thermodynamics of solution and kinetic processes that determines ferrous martensites coarsening resistance.

In a generalized multicomponent alloy system, the overall coarsening rate constant K results from the consideration of various solute additions. Equation (5.3) can be generalized using the concept of overall coarsening resistance (1/K) which is the result of summing over individual coarsening resistances due to individual alloying additions as follows from equation (5.4):

$$\frac{1}{K} = \sum_i \frac{1}{K_i} \tag{5.4}$$

where i represent the elements entering composition; then equation (5.5) can achieve for AISI 4340:

$$\frac{1}{K} = \frac{1}{K_{Cr}} + \frac{1}{K_{Mn}} + \frac{1}{K_{Mo}} + \frac{1}{K_{Ni}} + \frac{1}{K_{Si}} \tag{5.5}$$

In plain carbon steels, cementite dispersion coarsening rate is high because fast diffusing interstitial carbon controls the process at all temperatures. Substitutional alloying additions, due to their much lower diffusivity, decrease the coarsening rate of cementite during tempering; and this occurs even when partition happens preferentially in the matrix rather than in the precipitates (Lee, Allen et al. 1991).

As shown above in equation (5.3), thermodynamic parameters such as the solubility of the alloying element in the precipitates or in the matrix may play an important role in controlling

the coarsening rate and must be taken into account for accurate predictions. Equations (5.3) to (5.5) have been derived for more general cases than presented here (Morral and Purdy 1994) (Morral and Purdy 1995). These papers give equivalent expressions for equation (5.3) in the case of multicomponent alloys and multiphase alloys (Hoyt 1998), with a non-diagonal diffusivity matrix. Ardell also derived a mean-field theory of multicomponent precipitates coarsening in the case of diffuse interfaces (Ardell 2013). Finally, Philippe and Voorhees have proposed a complete formulation of the mean-field theory in the adequate formalism (Philippe and Voorhees 2013). Their paper includes a derivation of the asymptotic formula for the equation of the coarsening rate at large times in the multicomponent case, with a full diffusivity matrix. Their formula is valid for the case of a diagonal mobility matrix (equation (47) in reference (Philippe and Voorhees 2013) and is completely equivalent to equation (5.3) given here.

In this chapter, the retarding effect of alloying elements in AISI 4340 have been modeled with DICTRA (DIffusion Controlled TRAnsformations) 27 Software and Thermo-Calc 3.1, Thermo-Calc Software TCFE7 Steels/Fe-alloys database version 7, multi-component thermodynamics database, and Thermo-Calc Software MOBFE2 Steels and Fe-Database, v2 mobility database (Andersson, Höglund et al. 1990). The coarsening of precipitates that have initial plates shape was modeled (Krauss 2005) (Jönsson 1995).

Precipitation sequence at 923 K (650 °C) have been investigated in detail to understand the mechanism of cementite dispersion coarsening, and to set-up the initial conditions for DICTRA calculations. Experiments and modeling using CALPHAD method are complementary to this research in order to better understand the coarsening resistance of this steel composition during induction hardening processing.

5.3 Modeling multicomponent cementite coarsening

An extended LSW theory for multicomponent alloy has been used to model the precipitation sequence in this steel based on CALPHAD modeling. The growth and coarsening kinetics of cementite at 923 K (650 °C) is modeled using DICTRA software package (2013) (Hu, Li et al. 2006) (Andersson, Helander et al. 2002). The numerical procedure behind DICTRA aims to solve the multicomponent diffusion problem at a moving interface, or Stefan problem

(Andersson, Helander et al. 2002). The thermodynamics database TCFE version 7 (2013) is both used to calculate the diffusivity of matrix, that has a thermodynamic component (Andersson and Ågren 1992), as well as determining the flux balances, or local equilibrium conditions that prevail at the interface. The mobility database MOBFE version 2 (2011) have been used to provide assessed mobilities for all species in both the matrix and cementite. The two databases have been developed by the Foundation of Computational Thermodynamics in Stockholm Sweden to fully comply with each other, and are therefore complementary. Both TCFE7 and MOBFE2 are commercial databases specialized for steels and iron alloys, and licensed by Thermo-Calc Software Company (Guide 2013).

The region controlling the reaction rate is at the interphase between cementite and martensite, therefore modeling is carried out under, local equilibrium conditions at a temperature that allows complete partitioning of the substitutional elements between two phases at the θ/α interface. This kinetic regime is often called Local Equilibrium with Partition (PLE) (Ghosh and Olson 2002). In the PLE regime, the kinetic is controlled by the slow diffusion of substitutional elements in the matrix as described by Coates for ternary systems when one species diffuses much faster than the others (Coates 1972) (Coates 1973) (Coates 1973). In a system with n elements, local equilibrium kinetics is modeled using flux balances, that must be obeyed at the precipitate matrix interface as described by the set of equation (5.6):

$$v^{\alpha} C_i^{\alpha} - v^{\theta} C_i^{\theta} = J_i^{\alpha} - J_i^{\theta} \qquad i = 1,2..,n \tag{5.6}$$

where v^{α} and v^{θ} are the migration rates of the interface in local frame of reference in the matrix and cementite phases respectively, C_i^{α} and C_i^{θ} are the concentrations of the components i in matrix and cementite adjacent to interface respectively, and J_i^{α} and J_i^{θ} are the diffusive fluxes of the different species on both side of the interface (Andersson, Höglund et al. 1990).

Moreover, the mass conservation in the whole system can be described by the continuity equation (5.7):

$$\frac{\partial c_i}{\partial t} = -div(J_i) \tag{5.7}$$

where C_i is the concentration in moles per volume, div is divergence operator, and J_i is the flux of component in the multicomponent system i. It can be calculated by the Fick Onsager equation (5.8):

$$J_i = -\sum_{j=1}^{n-1} D_{ij}^{n} \nabla c_j \tag{5.8}$$

where n denotes the dependent species or solvent phases, D_{ij}^{n} is the intrinsic inter diffusion coefficient describing the interaction of element i with the jth concentration gradient in a matrix rich in solvent n, ∇c_j would be the concentration gradient of component j. The intrinsic diffusion coefficients form a matrix, where the diagonal represents interaction of one species with its own gradient, and the off-diagonal terms represent the interactions among different fluxes. The interactions among concentration gradients originate from interactions among chemical fluxes, which are the true driving forces for diffusion in heterogeneous systems (Jönsson 1994) (Jönsson 1992). Moving from one representation to another is equivalent to a transformation from the lattice frame of reference to the laboratory frame of reference, and is accomplished numerically in DICTRA by a set of transformation as explained in (Andersson and Ågren 1992).

The kinetic equations formed by equations (5.6) and (5.7), substituting (5.8) for the fluxes are solved numerically simultaneously by the DICTRA software package, for cementite growth under coarsening condition (2013) (Andersson, Höglund et al. 1990).

5.4 Initial condition

5.4.1 Chemical composition

In order to model the Q&T initial condition, the chemical compositions in cementite and ferrite have been calculated under paraequilibrium (PE) conditions at 653 K (380 °C) using Thermo-Calc appendices II and III. In PE regime, it is assumed that, due to the low tempering temperature, the large difference in diffusion rates, and the somewhat short tempering times involved, the cementite found in Q&T conditions was essentially Fe_3C, or that "frozen-in" conditions prevailed for all substitutional alloying elements (Liu and Agren 1989) (Zhu, Xiong et al. 2007) (Hillert 2008). This assumption has been shown to be verified in AISI 4340 steel after tempering at 598K (325 °C) for 2h by Clarke et al. (Clarke, Miller et al. 2014).

In DICTRA simulations, the average chemical composition of the AISI 4340 steel has been assumed except for Mo, called CMNS[1], for the sole purpose of saving computing load as large system of equations are slow, and often difficult to solve. Molybdenum, indeed is alloyed to rather low quantities and is expected to diffuses slowly in ferrite (Bhadeshia 1989). Hence its influence would be only sensible after longer tempering times than the ones experimentally investigated in this study. However Mo importance in retarding the coarsening of cementite in 4340 steels at late stages must not be overlooked (Bhadeshia 1989) (Clarke, Miller et al. 2014), as atom-probe "proximity histograms" at cementite/ferrite interface in AISI 4340 steel have clearly show that Mo segregation to interlath cementite (Bhadeshia 1989) (Clarke, Miller et al. 2014) before long tempering times at 575 °C.

In DICTRA next simulation, the average chemical composition of the AISI 4340 steel has been assumed except for Si, called CMMN[2], also for the sole purpose of saving computing load as large system of equations are slow, and often difficult to solve. Silicon, indeed is also alloyed to rather low quantities. However, the importance of Si which acts as a barrier role

[1] Cr-Mn-Ni-Si
[2] Cr-Mn-Mo-Ni

for further growth should not be ignored after long time tempering at 650 °C (Kozeschnik and Bhadeshia 2008) (Kim, Celada et al. 2013) (Kim, Boucard et al. 2014) (Ghosh 2010).

5.4.2 **Geometry of the computational cell**

Computations have been based on assuming that the two regions corresponding to cementite (inner) and tempered martensite (outer) have both spherical geometries, see Figure 5-1. They constitute one cell with two moving boundaries. The inner moving boundary is the cementite-matrix interface with equation (5.6) defining the interface movement. The outer is a "free moving boundary" where constant chemical potential conditions have been fixed to their value at equilibrium, simulating the conditions prevailing during Ostwald ripening far from the precipitates, at the impingement volumes boundaries (Martin, Doherty et al. 1997).

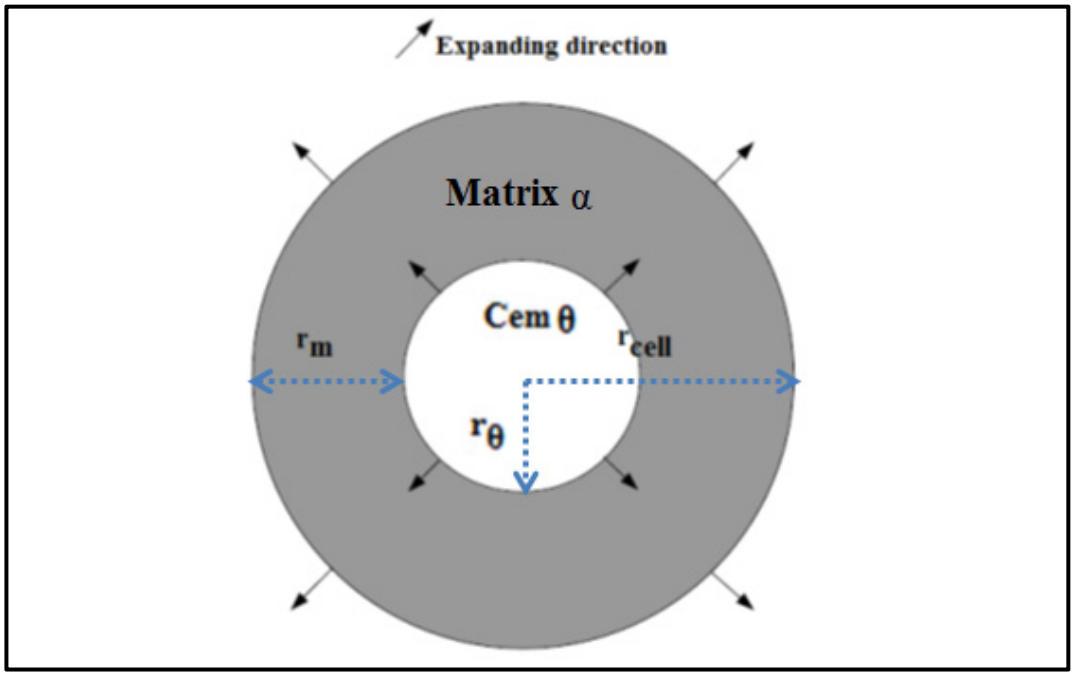

Figure 5-1 The 2D schematic picture of one cell in a DICTRA coarsening model displayingcementite in the center of tempered martensite (ferrite) matrix (Hu, Li et al. 2006).

The initial radius of the cell can be calculated by equation (5.9):

$$V_f^{\theta} = \frac{V_{\theta}}{V_{cell}} = \frac{r_{\theta}^3}{r_{cell}^3} \tag{5.9}$$

where V_f^{θ} is the volume fraction of cementite derived by T-C calculation at 653 K (380 °C) equal to 6.13 %, (which corresponds roughly to experimental data). r_{θ} is the average radius of cementite particle distribution. Multiplying r_{θ} by 1.5 yields 5.82×10^{-8} m, which is the largest precipitate, therefore the only class that will never dissolve under the LSW coarsening regime, and r_{cell} is the radius of the cell (Hu, Li et al. 2006, Ghosh 2010).

5.4.3 **Particle size distribution**

A steady state distribution of precipitates, typical of the classical coarsening theory LSW steady-state particle size distribution (PSD) is implicitly assumed by DICTRA for modeling cases where growth and dissolution rates are influenced by nearest neighbors particles (Greenwood 1956).

DICTRA assumes indeed that the overall kinetics can be calculated considering a single particle having the maximum particle size given by the coarsening steady-state distribution. This particle is 1.5 times as large as the average precipitate size (Hu, Li et al. 2006). Because it corresponds to the largest precipitate size, according to LSW theory, a precipitates with this size at the onset of coarsening will never dissolve. Therefore, the evolution of the PSD under LSW kinetics is reduced to computing the growth of a unique precipitate.

5.4.4 **Coarsening term**

To further simulate Ostwald ripening, DICTRA adds a Gibbs-Thomson capillarity term ΔG_m to the average chemical driving force (or chemical potentials). This term is simply calculated according to relation (5.10):

$$\Delta G_m = \frac{2\sigma V_m^{\theta}}{r} \quad (5.10)$$

where V_m^{θ} is molar volume of cementite that has been taken to be 2.4×10^{-5} m^3/mol (Björklund, Donaghey et al. 1972). The particle radius, r is, automatically updated by DICTRA during the computations using the θ/bcc interface position at time t. The cementite interfacial energy σ has been adjusted from DICTRA simulations using experimental precipitation sequences by a data fitting process to experimental results, using the mean spherical equivalent radius, corrected using Saltykov method as the radius statistic. To allow direct comparison, radius r provided by DICTRA must thus be divided by 3/2.

5.5 Pure growth at 923 K (650 °C)

5.5.1 Chemical composition Cr-Mn-Ni-Si

Pure growth or growth without impingement of the diffusion field for each particle should be considered as the primary mechanism controlling the growth behaviour of the cementite precipitates. It will eventually introduce a delayed time for the start of coarsening. During this first stage, despite the changes in chemical composition of alloying elements in the cementite and matrix, there is a limited number dissolution of smaller particles and few overlapping of diffusion fields among precipitates. Movement of alloying elements in both regions is activated to dissipate free energy, in other word to reduce the chemical potentials in the system. Therefore, the intermediate chemical composition of cementite and matrix after paraequilibrium condition for specific time should be determined, when pure growth is finishing and coarsening begins.

To do so, the pure growth model is run by DICTRA in appendices (IV), (VI), and (VII). The initial para equilibrium chemical composition is used as starting point for this stage by considering LSW distribution of spherical particles (no Gibbs-Thomson effect). The changes in chemical composition of different alloying elements as a function of time are then calculated.

In Figure 5-2 (a) to (d), curve #1 represent, as a function of time, the variations of element concentrations at the interface between the two phases from the matrix side, while curve #2 is the same variation in the matrix only. These results show that a minimum of 200 sec is necessary for the mole fractions to start decreasing from their initial value. This time is considered to be the moment when the matrix starts to be depleted from alloying elements at the beginning of the coarsening. This is illustrated also on the curve #2 in these figures as during for short time ($t < 200$ sec) the chemical composition averages in matrix decrease gradually for partitioning alloying elements, and increase for non-partitioning one.

The variations of chemical composition for the cementite and matrix region versus distance obtained at the end of the pure growth stage (as calculated after 200 sec) are then introduced into the coarsening model. A more accurate interface position can be determined for cementite and carbide cell size. The consideration of the initial pure growth stage introduces corrections on the initial state of the system for coarsening, reducing the error between the developed model and experimental results.

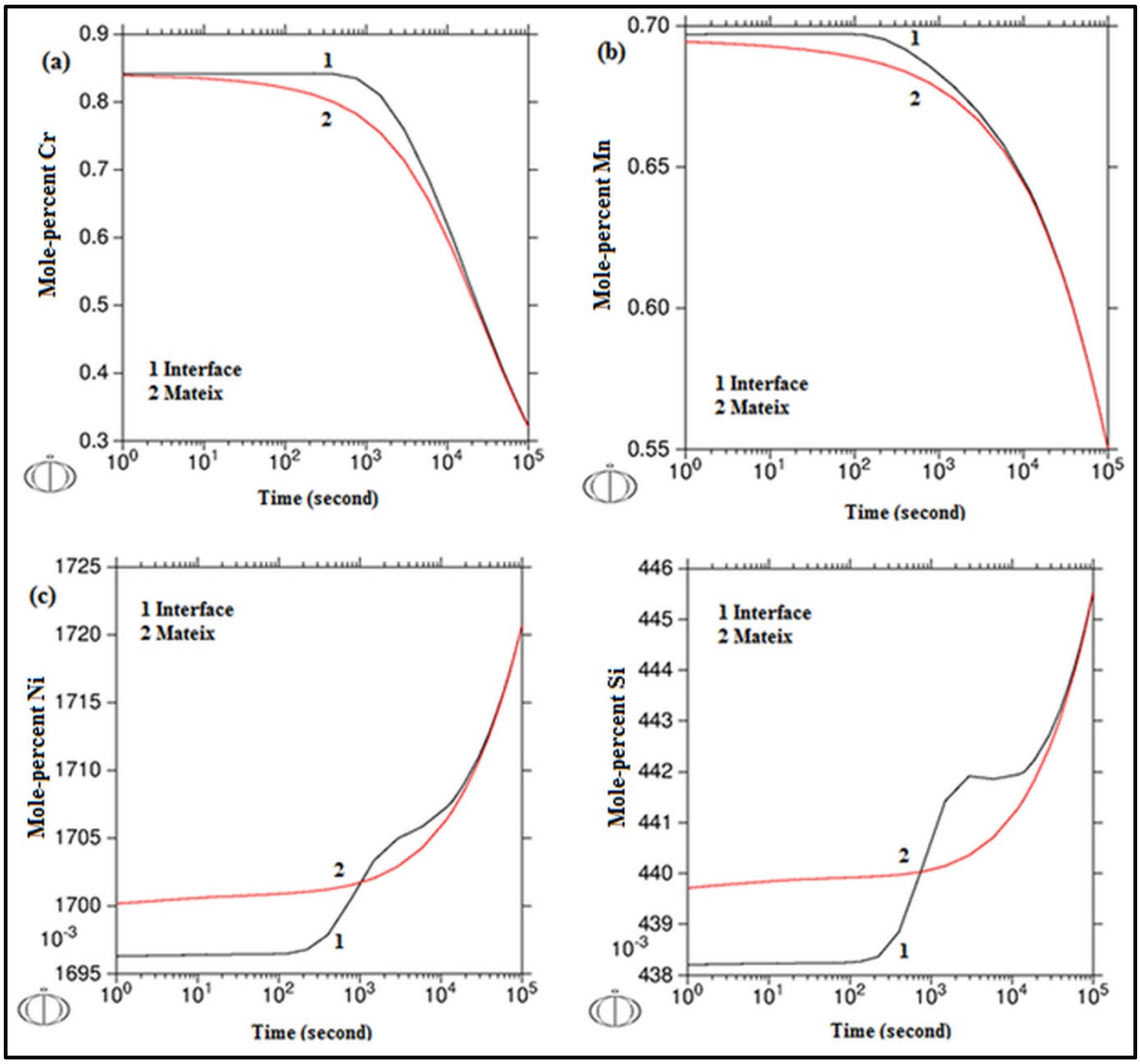

Figure 5-2 Variations of alloying elements profile in the interface of cementite and matrix versus time at 650 °C during pure growth stage, a) Cr, b) Mn, c) Ni, d) Si

5.5.2 **Chemical composition Cr-Mn-Mo-Ni**

Pure growth has been also considered for taking into account the effect of Mo in multicomponent system during tempering procedure. The same procedure was done to determine the variations of alloying elements profiles at the interface and into the matrix in

appendices (V) and (VI) and (VII). The results are illustrated in Figure 5-3 (a) to (d). Curve #1 represent, as a function of time, the variations of element concentrations at the interface between the two phases from the matrix side, while curve #2 is the same variation in the matrix only. These results show that a minimum of 200 sec is necessary for the mole fractions to start decreasing from their initial value. This time is considered to be the moment when the matrix starts to be depleted from alloying elements at the beginning of the coarsening. This is illustrated on the curve #2 in these figures as during for short time ($t < 200$ sec) the chemical composition averages in matrix decrease gradually for partitioning alloying elements, and increase for non-partitioning one.

The variations of chemical composition for the cementite and matrix region versus distance obtained at the end of the pure growth stage (as calculated after 200 sec) are then introduced into the coarsening model. A more accurate interface position can be determined for cementite and carbide cell size. The consideration of the initial pure growth stage introduces corrections on the initial state of the system for coarsening, reducing the error between the developed model and experimental result.

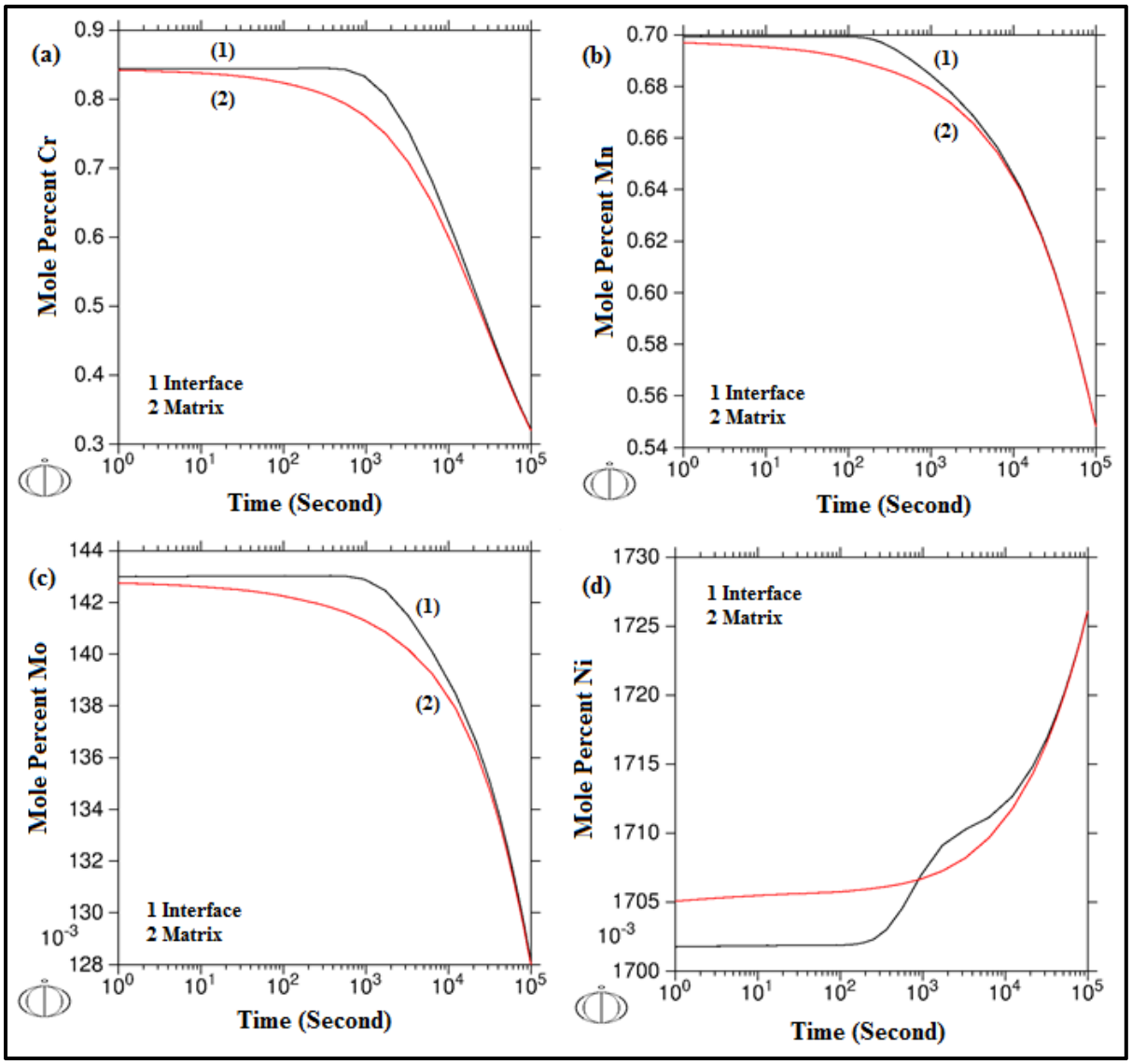

Figure 5-3 Variations of alloying elements profile in the interface of cementite and matrix versus time at 650 °C during pure growth stage, a) Cr, b) Mn, c) Mo, d) Ni

5.6 Coarsening at 923K (650 °C)

5.6.1 Chemical composition Cr-Mn-Ni-Si

Coarsening of precipitates when diffusion fields around particles overlap has been modeled in this stage by considering the Gibbs-Thomson effect as the driving force of the system in appendices (VIII) and (X). In Figure 5-4, coarsening curve simulated with DICTRA is compared to experimental data. The interfacial energy was adjusted by fitting data with the experimental precipitation sequences and the optimal value was found to be 0.35 Jm^{-2}. Figure 5-4 shows how by choosing different interfacial energy from 0.3 to 0.55 Jm^{-2} the best fit could be selected for this system. The optimal value was found to be 0.35 Jm^{-2} that is in the range of previous research Table 1-1 (Pandit 2011).

Discrepancies observed between experiment and model could be due to the special assumptions in the model, and the spheroidization of initial plate precipitates happening prior to coarsening, see Figure 5-5 (a).

The coarsening constant K in equation (5.1) can be estimated from the model equal 8.63×10^{-26} m^3s^{-1}, while the one derived from experimental data is 2.83×10^{-26} m^3s^{-1}, showing a similar order of magnitude. However the coarsening rate modeled by DICTRA is not constant, but varies due to the partition of elements as seen in equations (5.2) and (5.3). Changes in K are due to changes in the matrix composition of Cr, Mn, Ni and Si and will be discussed in section 5.8. The rather good agreement on the values of the interfacial energy for cementite and that of the coarsening rate, does not only validates the assumptions made in the derivation of the model, including neglecting the important element Mo (Clarke, Miller et al. 2014), but also demonstrates the predictive power of CALPHAD assessed databases TCFE7 and MOBFE2 for studying the coarsening of cementite in multicomponent engineering steels.

5.6.2 Chemical composition Cr-Mn-Mo-Ni

The behavior of cementite during coarsening procedure is simulated by using the same procedure for the chemical composition with Mo in appendices (IX) and (X). Likewise, 0.35 Jm^{-2} is used as the best fit for interfacial energy. Figure 5-5 (b) is shown the variation of cube mean radius of cementite versus time.

The coarsening constant K in equation (5.1) can be estimated from the curve for multicomponent system with the Mo effect equal 3.34×10^{-25} m^3s^{-1}. By comparing it with the one derived from experimental data 2.83×10^{-26} m^3s^{-1}, it shows a much faster trend of almost 12 times. As Si is removed from the chemical composition, this could be explained by not having the resistance coarsening due to this element for long tempering time.

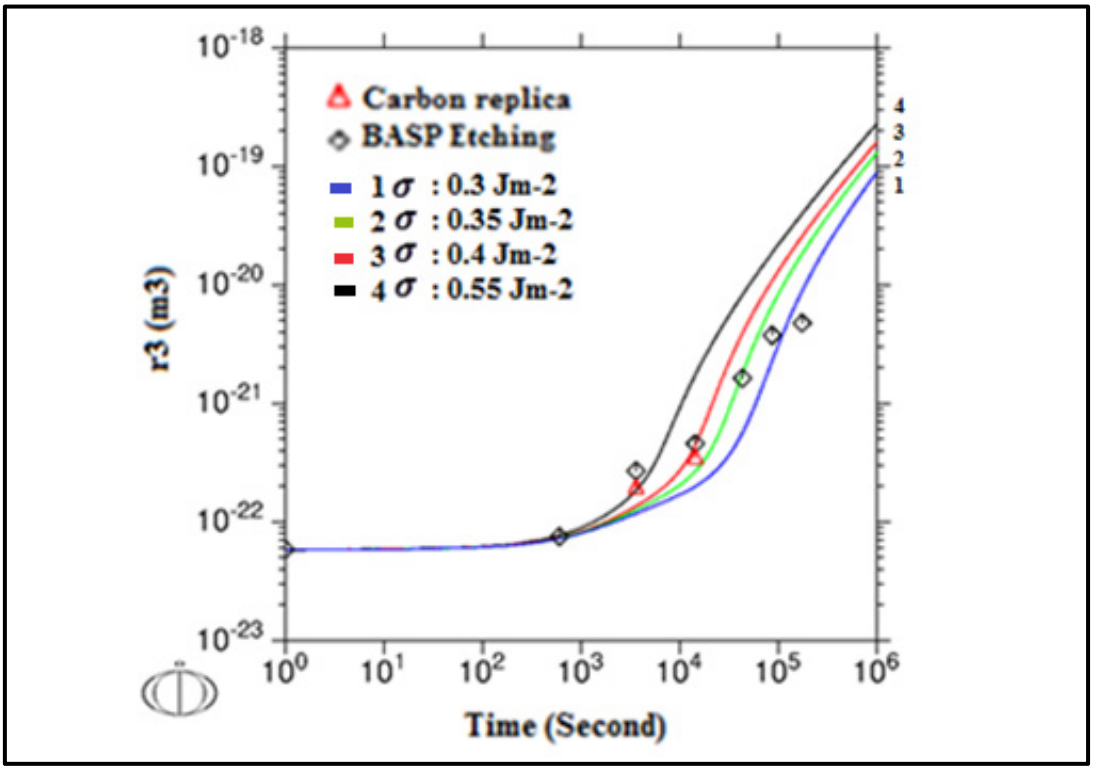

Figure 5-4 Data fitting procedure with experimental data to define the best fit of interfacial energy with coarsening curve at 650 °C.

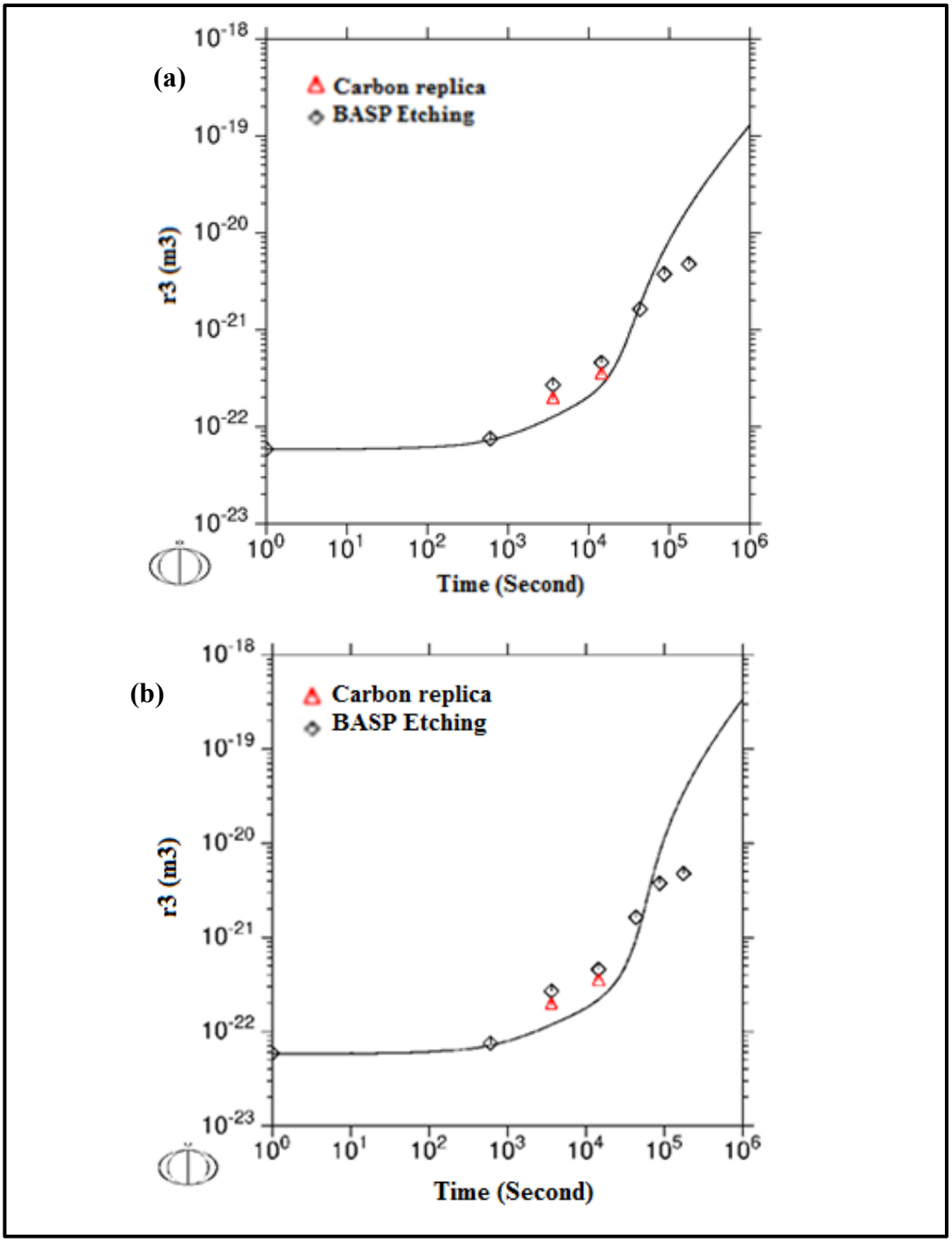

Figure 5-5 Ilustration of cementite cube radius versus time during tempering at 650 °C by DICTRA modeling in compare with experimental data by consideringthe impingement effect around particles in cementite and ferrite a) Cr-Mn-Ni-Si, b) Cr-Mn-Mo-Si

5.7 Evaluation of carbon and alloying elements after tempering

5.7.1 Evaluation of carbon after tempering

In order to relate the cementite coarsening and the diffusion of interstitial and substitutional alloying elements in cementite and matrix, the profile variation of carbon and alloying elements in the cell at different tempering time were examined. Figure 5-6 (a) and (b) displays the variations of carbon mole percent versus cell distance at different tempering times and chemical composition. A steep slope of carbon concentration is found in the matrix in front of interface after 10 min of tempering. This peak disappears after 60 min tempering, generating a matrix of rather with a uniform concentration. A corresponding bump can be observed on Cr and Mn profiles Figure 5-7 (a) and (b) and Figure 5-8 (a) and (b).

This bump can be recognized in Mo profile even after 60 min tempering in Figure 5-8 (c). It can be observed as well as inverted, through on Ni and Si profiles after 10 min tempering Figure 5-9 (a) and (b) and Figure 5-10. The strong correlation between C and substitutional elements (Coates 1972) (Coates 1973) (Coates 1973), can be understood solely through interactions with substitutional alloying element via the inter-diffusion coefficient matrix equation (5.7) as C high diffusivity should lead to fast homogenization of its composition in the matrix. Within the diffusion matrix, off-diagonal coefficients that represent interactions among carbon and the substitutional are non negligible (Coates 1973). DICTRA computation predict a slow but steady decrease in residual matrix carbon content after long time of tempering, indicative of the system approaching equilibrium. Therefore, carbon diffusion field in the matrix, as it is strongly coupled to substitutional elements partitioning behavior as explained by equation (5.3), is a mere indicative of the overall diffusion field existing in the system during coarsening (Umantsev and Olson 1993). As expected, because most of the C has already partitioned into cementite at the very beginning, before the computations, the fluxes are merely controlled by the substitutional, slowly diffusing elements. The change in chemical composition of system has significant influence on the precipitate and matrix size in Figure 5-6 (a) and (b). The cementite interface has more progress in matrix, and matrix is larger by adding Mo, and removing Si from system.

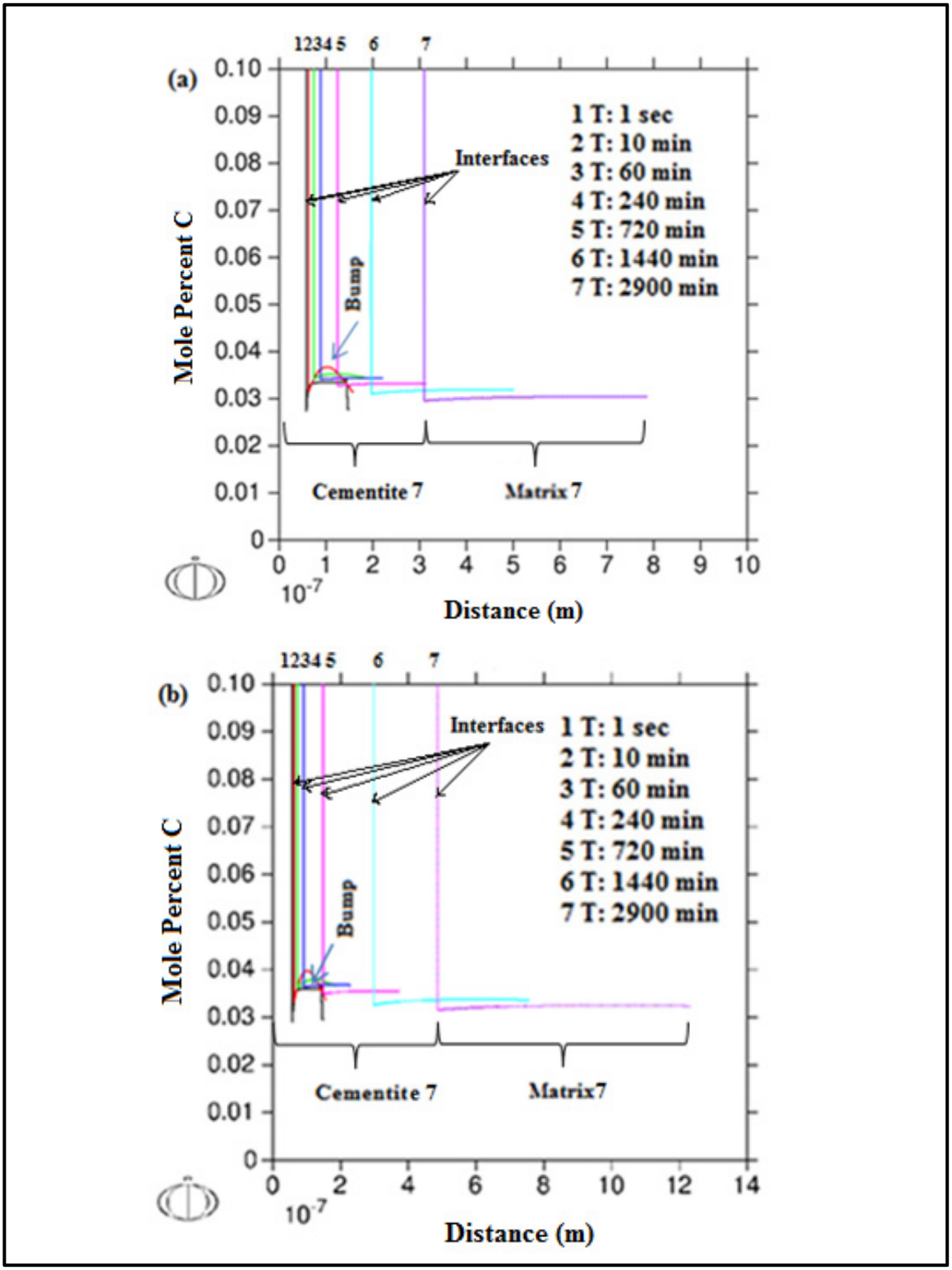

Figure 5-6 Variation of carbon mole percent profile versus cell distance at 650 °C and different times during coarsening stage chemical composition, a) Cr-Mn-Ni-Si, b) Cr-Mn-Mo-Ni. Interfaces moves to the right as a function of time.

5.7.2 Evaluation of Cr and Mn after tempering in CMNS

Chromium and Manganese concentration profiles are depicted on Figure 5-7 (a) and (b). When computation starts, i.e. coarsening starts, amounts of Cr and Mn in Q&T condition 653 K (380 °C) are equal in cementite and matrix. This is due to the paraequilibrium conditions and the relative immobility of the substitutional elements in the interface due to very low temperature of the tempering (Schneider and Inden 2005). At very short tempering times a spike is visible in the immediate vicinity of the interface. This spike resembles negligible partition local equilibrium (NPLE) conditions, that are a way to adjust negligible diffusivity with the strong tendency for phase transformation. However, here, the spike is only transitory and likely due to the very slow diffusivity of Cr and Mn in cementite compared to that in the matrix, as result, Cr and Mn accumulate at the interface, at the cementite side to balance the fluxes equation (5.6). As already mentioned for carbon profiles, a bump is observed between 1 sec to 10 min tempering. This “bump” results from interfacial conditions at the matrix-precipitate interface from the matrix side, showing depletion compared to the average matrix content, coupled with a similar behavior at the outer free boundary due to the enforcement of coarsening conditions by DICTRA. With further tempering the spike enlarges and decreases in amplitude due to solutes slowly diffusing through cementite, with a slightly highest rate for chromium. Accordingly, the Cr and Mn contents of the martensitic matrix decreases rapidly allowing to the rate of coarsening increase.

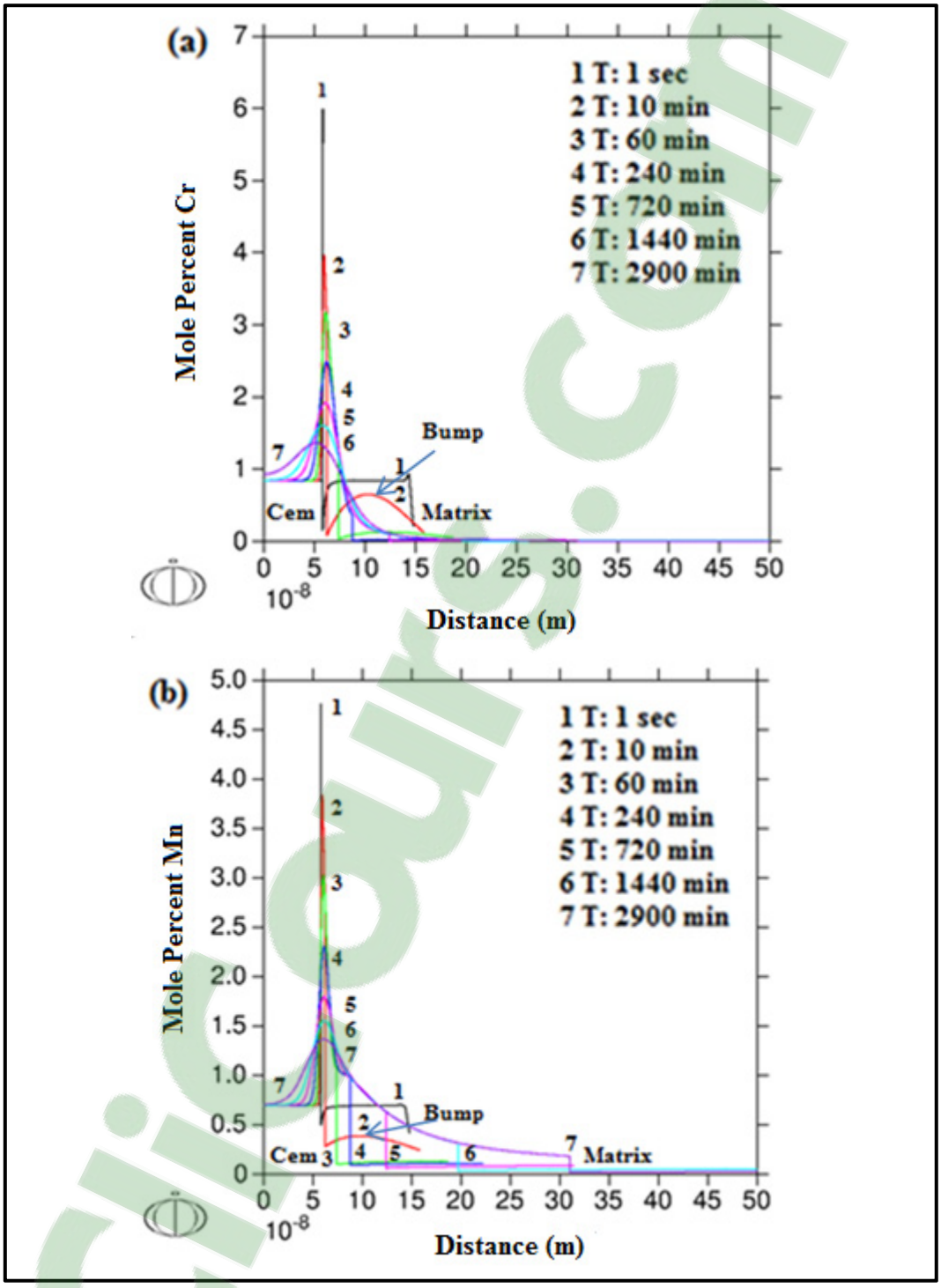

Figure 5-7 Variations of a) Cr b) Mn mole percent profiles versus cell distance for different tempering time at 650 °C with chemical composition Cr-Mn-Ni-Si

5.7.3 Evaluation of Cr, Mn, and Mo after tempering in CMMN

Chromium, Manganese, and Molybdenum concentration profiles are depicted on Figure 5-8 (a), (b), and (c). When computation starts, i.e. coarsening starts, amounts of Cr, Mn, and Mo in Q&T condition 653 K (380 °C) are equal in cementite and matrix. This is due to the paraequilibrium conditions and the relative immobility of the substitutional elements in the interface due to very low temperature of the tempering (Schneider and Inden 2005). At very short tempering times a spike is visible in the immediate vicinity of the interface. This spike resembles negligible partition local equilibrium (NPLE) conditions, that are a way to adjust negligible diffusivity with the strong tendency for phase transformation. However, here, the spike is only transitory and likely due to the very slow diffusivity of Cr, Mn, and Mo in cementite compared to that in the matrix, as result, Cr, Mn, and Mo accumulate at the interface, at the cementite side to balance the fluxes equation (5.6). As already mentioned for carbon profiles, a bump is observed between 1 sec to 10 min tempering for Cr and Mn. This bump can be recognized for Mo even for 60 min tempering due to its lower diffusion rate. This “bump” results from interfacial conditions at the matrix-precipitate interface from the matrix side, showing depletion compared to the average matrix content, coupled with a similar behavior at the outer free boundary due to the enforcement of coarsening conditions by DICTRA. With further tempering the spike enlarges and decreases in amplitude due to solutes slowly diffusing through cementite, with a slightly highest rate for chromium, and lowest rate for Molybdenum. Accordingly, the Cr, Mn, and Mo contents of the martensitic matrix decreases rapidly allowing to the rate of coarsening increase.

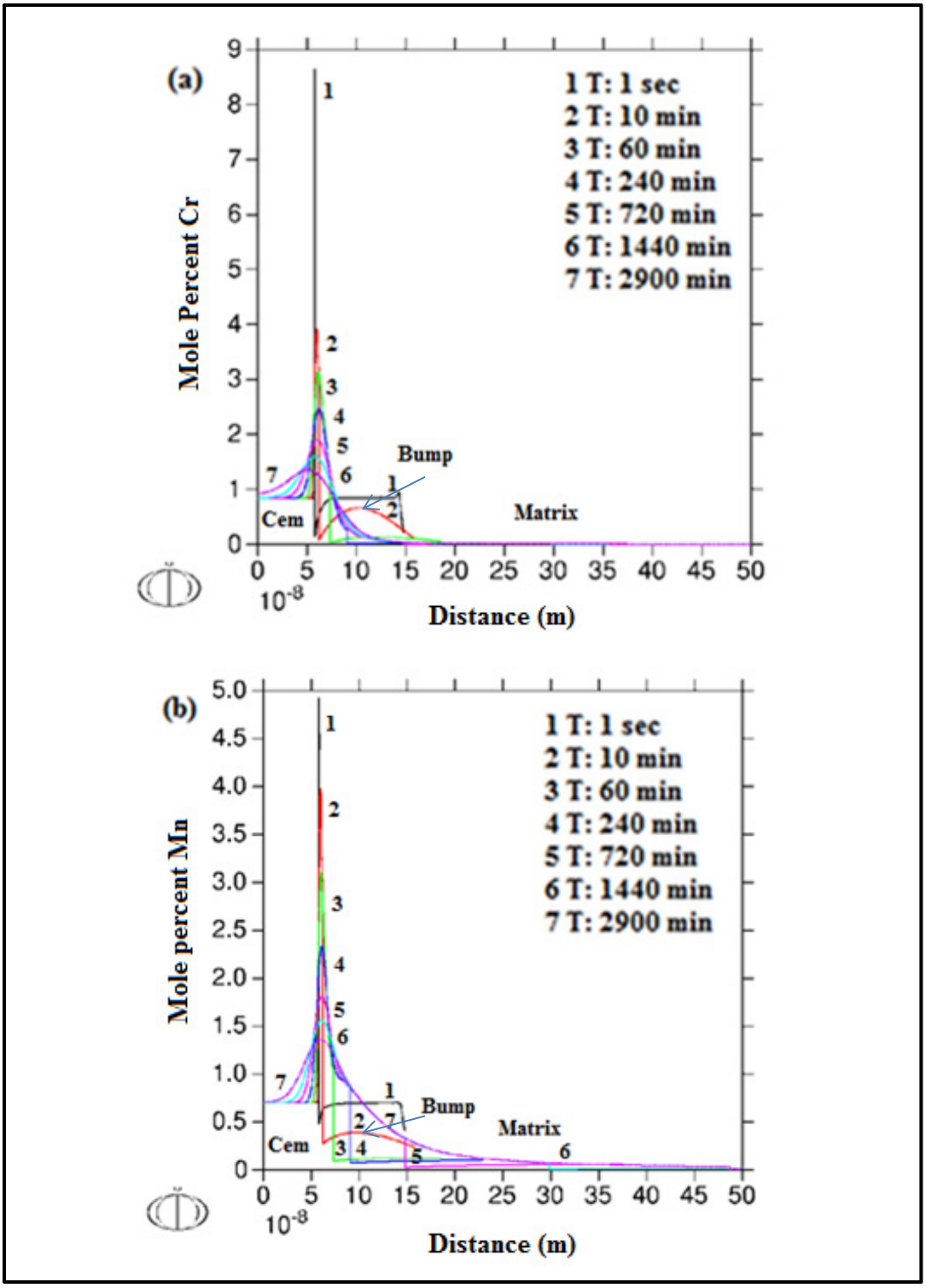

Figure 5-8 Variations of a) Cr, b) Mn mole percent profiles versus cell distance for different tempering time at 650 °C with chemical composition Cr-Mn-Mo-Ni.

Figure 5-8 (continued) c) Mo

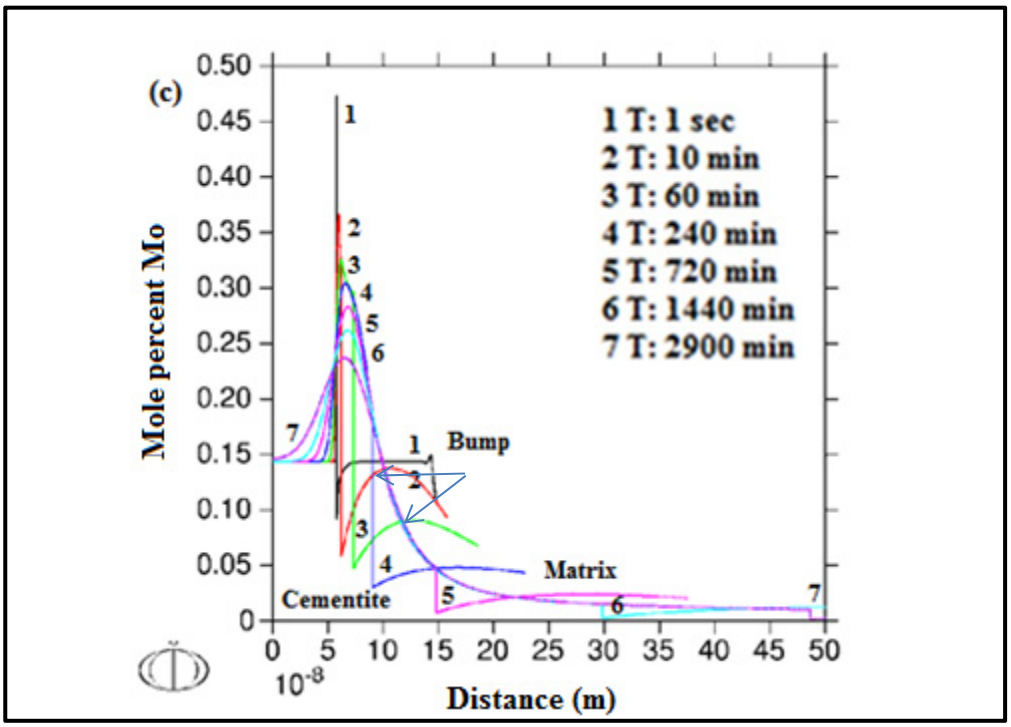

5.7.4 Evaluation of Ni and Si after tempering in CMNS

The chemical composition profiles of Ni and Si are shown in Figure 5-9 (a) and (b). They display a different behavior from Cr and Mn as they both tend to partition in the matrix rather than in the precipitates. Their initial chemical contributions to the cementite partition are not significant, as shown in Figure 5-9, as well as in Table 4-1. Due to their low solubility in cementite, they show slight pile up at the interface from the matrix side; at least at the beginning of the tempering. Then, the slow diffusion of substitutional atoms in matrix phase prevents the rapid coarsening of the cementite. In particular, the localized Ni and Si enriched area adjacent to the cementite interphase plays a kinetic barrier role for the subsequent growth of cementite (Schneider and Inden 2005). Moreover, the Si enriched area around the cementite decelerates the transferring of Si from cementite to matrix; therefore the initial cementite still has significant quantity of this element which reduces the stability of the precipitates as non-carbide forming elements (Chang and Smith 1984). It is thus clear, from

these figures that, both Ni and Si play a significant role in preventing fast growth of precipitates at late stages of coarsening, when the retardation effect due to partition of Cr and Mn in cementite reaches a state close to completion.

5.7.5 **Evaluation of Ni after tempering in CMMN**

The chemical composition profile of Ni is shown in Figure 5-10. It displays a different behavior from partitioning alloying elements Cr, Mn, and Mo as it tends to partition in the matrix rather than in the precipitates. Its initial chemical contribution to the cementite partition is not significant, as shown in Figure 5-10, as well as in Table 4-1. Due to its low solubility in cementite, it shows slight pile up at the interface from the matrix side; at least at the beginning of the tempering. Then, the slow diffusion of substitutional atom in matrix phase prevents the rapid coarsening of the cementite. In particular, the localized Ni enriched area adjacent to the cementite interphase plays a kinetic barrier role for the subsequent growth of cementite (Schneider and Inden 2005). It is thus clear, from this figure that, Ni play a significant role in preventing fast growth of precipitates at late stages of coarsening, when the retardation effect due to partition alloys Cr, Mn, and Mo in cementite reaches a state close to completion.

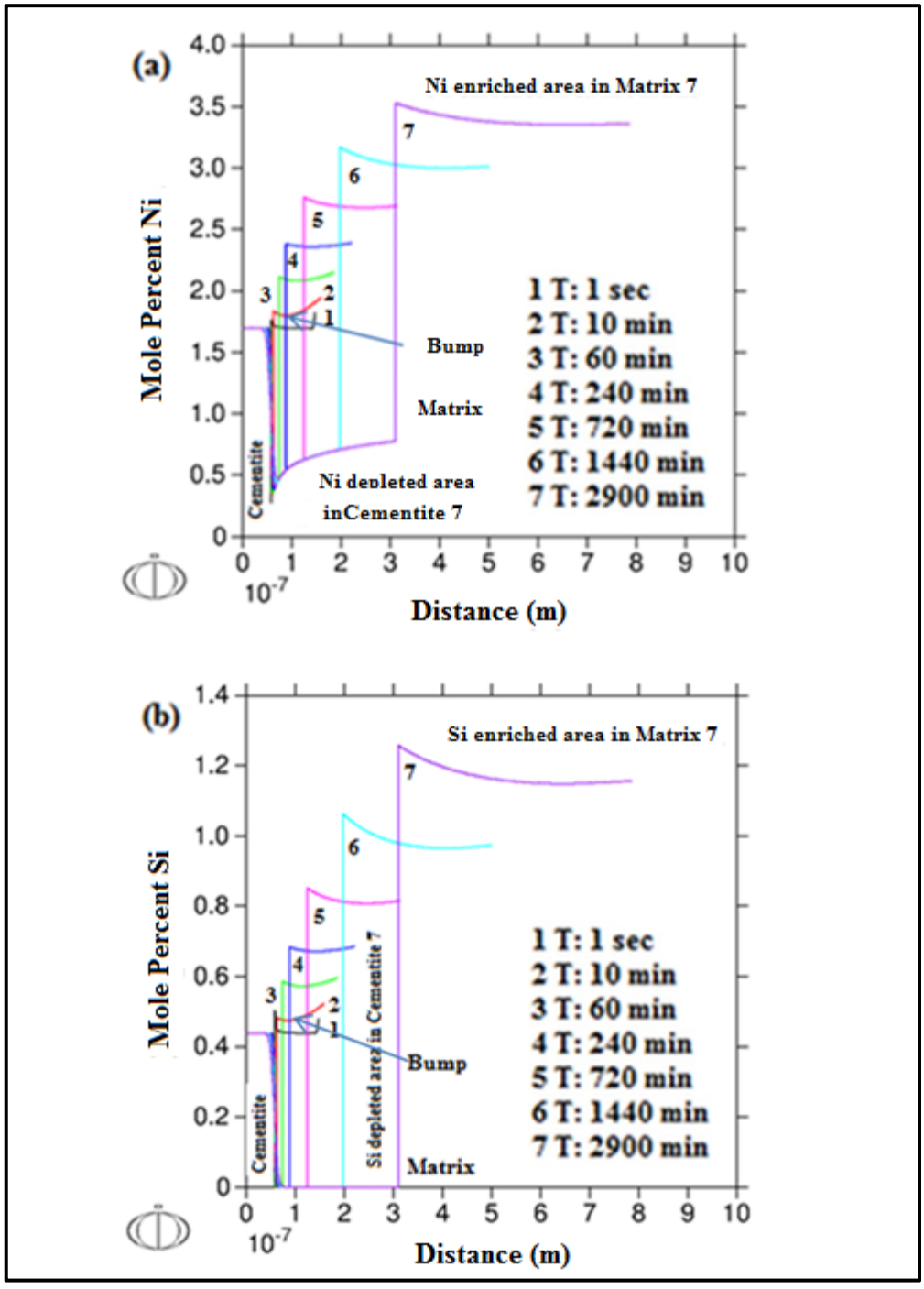

Figure 5-9 Variations of a) Ni and b) Si mole percent profiles versu cell distance for different tempering time at 650 °C with chemical composition Cr-Mn-Ni-Si.

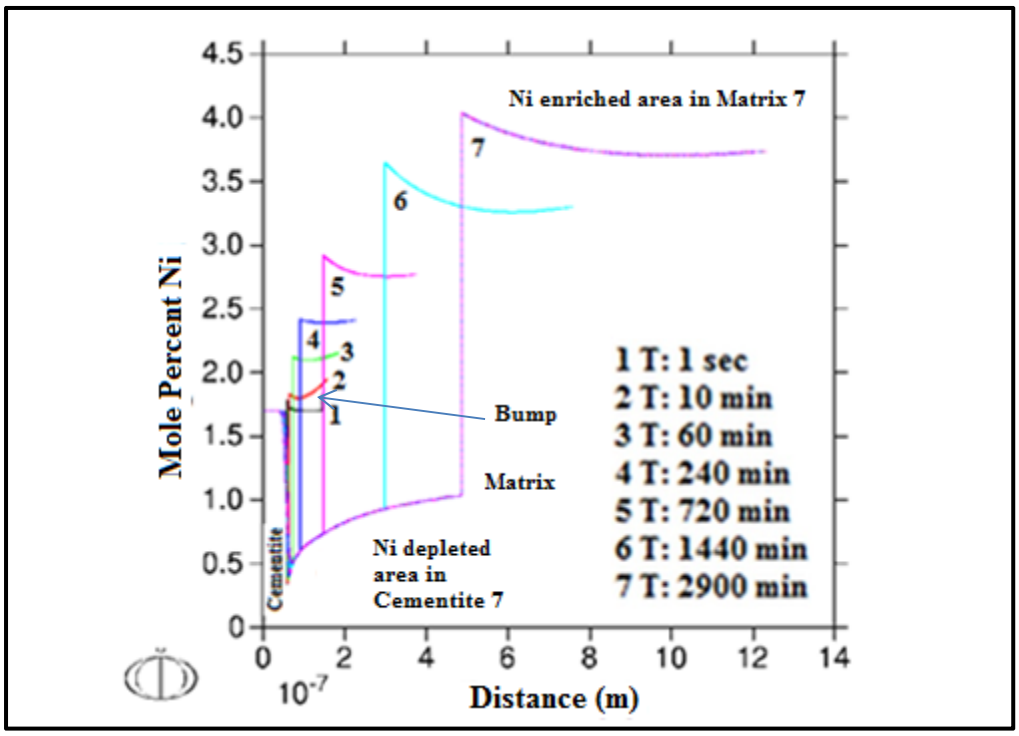

Figure 5-10 Variations of Ni mole percent profiles versus cell distance for different tempering time at 650 °C with chemical composition Cr-Mn-Mo-Ni.

5.8 Far-field concentration evolution and coarsening rate

5.8.1 Chemical composition CMNS

From DICTRA concentration profiles, it is possible to visualize how the rate of partitioning of alloying elements from the matrix into cementite precipitates affects the coarsening rate at 923 K (650 °C), through equations (5.2) and (5.3). The chemical composition changes in the matrix far from the growing phase cementite have been monitored using DICTRA and shown in Figure 5-11 (a) and (b). The accumulation of alloying elements Ni and Si, and the depletion in Cr and Mn from the matrix after prolonged tempering can be seen. Although Cr and Mn contents monotonously decrease on a logarithm time line, Si and Ni increase rapidly after an initial plateau. The initial plateaus account for the coarsening resistance of these elements (C_i^{α} are all almost constant in equation (5.2) making K small). However after some

time, varying far-field concentrations account for an increase in coarsening rate, that is however partly compensated by an increase in C_{Ni}^{α} and C_{si}^{α}. The far-field concentration evolutions in Figure 5-11 allow attributing the coarsening resistance of 4340 not only to carbide former elements Cr and Mn, but also to Ni and Si, especially at later stages since Ni diffuses rather slowly. In fact, at this moment, Cr and Mn are depleted in the matrix. Si, on the other hand, plays a role mostly through the anisotropy of interface gradients, discussed in previous section.

Finally, it is also expected that another plateau will be reached at even longer times, due to matrix compositions reaching their equilibrium phase diagram value-corrected by the Gibbs-Thomson effect. This can already be seen for Cr only on Figure 5-11 (a).

5.8.2 **Chemical composition CMMN**

The chemical composition changes in the matrix far from the growing phase cementite have been monitored using DICTRA and shown in Figure 5-12 (a) and (b). The accumulation of alloying elements Ni and the depletion in Cr, Mn, and Mo from the matrix after prolonged tempering can be seen. Although Cr, Mn, and Mo contents monotonously decrease on a logarithm time line, Ni increases rapidly after an initial plateau. The initial plateaus account for the coarsening resistance of these elements (C_i^{α} are all almost constant in equation (5.2) making K small). However after some time, varying far-field concentrations account for an increase in coarsening rate, that is however partly compensated by an increase in C_{Ni}^{α}. The far-field concentration evolutions in Figure 5-12 allow attributing the coarsening resistance of 4340 not only to carbide former elements Cr, Mn, and Mo but also to Ni, especially at later stages since Ni diffuses rather slowly. In fact, at this moment, Cr and Mn are depleted in the matrix.

Finally, it is also expected that another plateau will be reached at even longer times, due to matrix compositions reaching their equilibrium phase diagram value-corrected by the Gibbs-Thomson effect. This can already be seen for Cr only on Figure 5-12 (a).

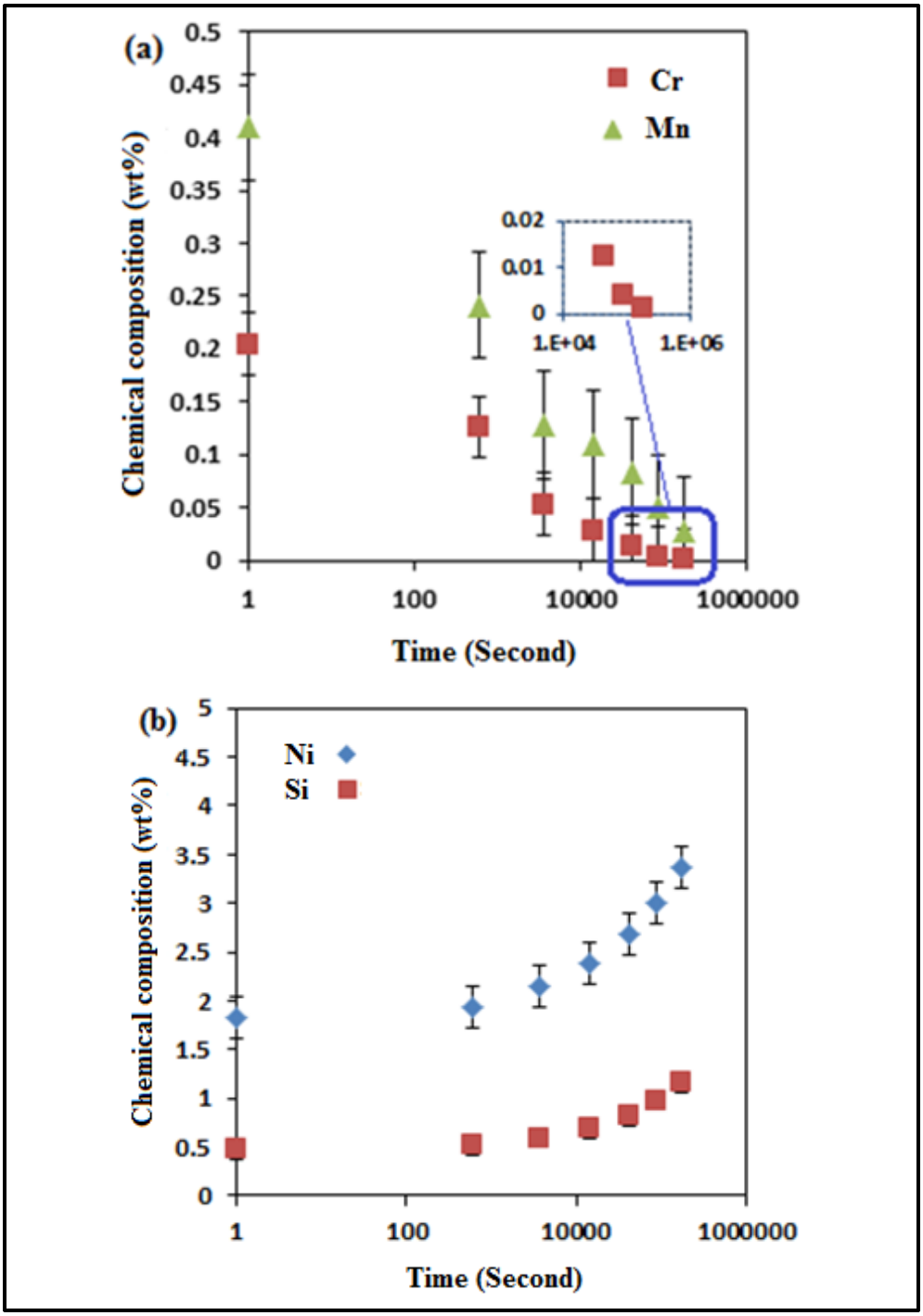

Figure 5-11 The variation of far-field chemical composition of alloying elements versus times (a) Cr, Mn b) Ni, Si wt%., the standard error is calculated for these values.

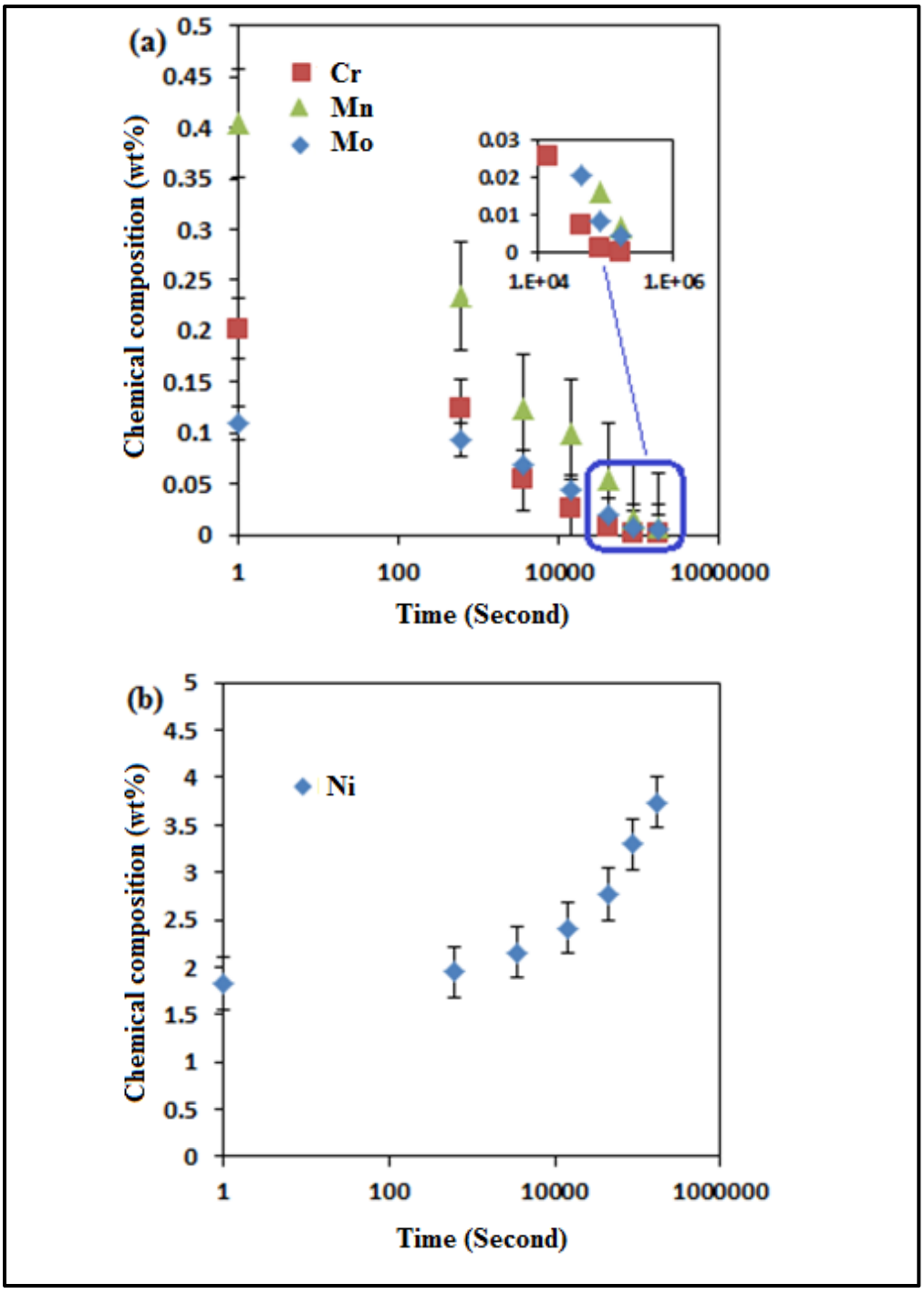

Figure 5-12 The variation of far-field chemical composition of alloying elements versus times (a) Cr, Mn, and Mo b) Ni wt%., the standard error is calculated for these values.

5.9 Modeling kinetics of cementite coarsening and grain growth

The kinetics coarsening of cementite is simulated based on extension of the Björklund model for ternary alloys system in multicomponent AISI 4340 steel in appendix (XI). In counterpart with DICTRA that used a complex partial differential equation for solving diffusion equation, the present model only required a system with two ordinary differential equations for solving diffusion fluxes.

The thermodynamics and kinetics databases partition coefficient and diffusion coefficient respectively are calculated by programming in Python (x,y) 2.7 software. They are coupled with cementite coarsening and ferrite grain growth. The average chemical composition of AISI 4340 steel is considered for this modeling. The effective diffusion coefficient is taken into account for this system. I.e. matrix is not defect free, and it consists of dislocation cells, which on further tempering becomes the ferrite subgrain. In addition, they act as an important mode of transport, and recognized as low resistance diffusion path. Further insight explanation about this method, and related equations can be found in (Björklund, Donaghey et al. 1972) (Venugopalan 1977) (Venugopalan and Kirkaldy.J.S 1978). Ferrite grain growth and cementite coarsening are modeled at 923K (650 °C) and results are shown in Figure 5-13. The interfacial energy 0.55 Jm^{-2} is compatible with experimental data at 923K (650 °C) based on a data fitting procedure.

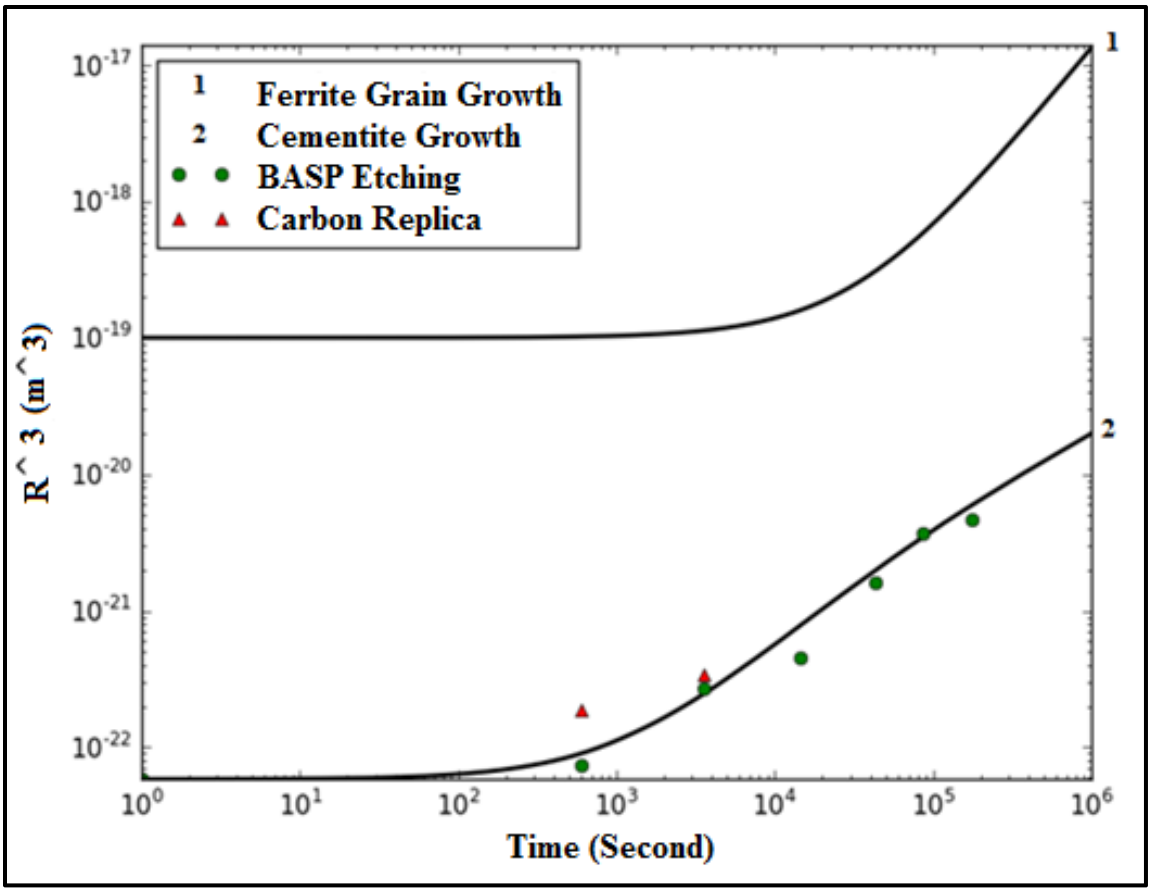

Figure 5-13 The ferrite grain growth, and cementite coarsening in comparison with experimental data at 923 K (650 °C).

5.9.1 Comparison with DICTRA simulation

In counterpart with DICTRA, in this model the matrix diffusivity i.e. AISI 4340 steel alloy is assumed a those of a dilute i.e. ideal (no diffusivity of matrix) alloy. Furthermore, the solute diffuses on the lath boundaries as well as in the matrix. This takes into account the fact that martensite is found to be a hierarchical structure with precipitates growing at lath intersections (big and round precipitates) at the same time as they grow in the matrix (elongated precipitates). This approach allows to get rid of spheroidization step that was difficult to take into account in an overall kinetics model. The resulting model using an

efficient diffusion coefficient that includes grain boundary diffusion is very fast, and it could take into account all elements for calculation.

5.10 Hardness estimation

Yield strength proportional to hardness is estimated based on microstructural features using equation (1.6) (Wang, Appolaire et al. 2006) (Kim, Boucard et al. 2014). Table 5-1 presented the contribution of each strengthening mechanism. Equation (1.7) is used to calculate the contribution of strength due to friction stress at room temperature. The carbon and alloying elements chemical composition of matrix are extracted from the modeling result. These elements contribute on hardness by solid solution strengthening mechanism equations (1.8) and (1.9). Their contribution is just significant at long tempering time by Mo, Ni, and Si see coefficients in Table 1-2.

Meanwhile, equation (1.13) is used to calculate the strength due to dispersion hardening. The increasing size of precipitates during tempering influences significantly on strength using by-passing Ashby-Orowan theory. Orowan theory equation (1.12) presents approximately same values. The total strength is taken into account by Ashby-Orowan theory studied by Kim et.al. The contribution of dislocation density on strength is extracted by equation (1.14). The initial dislocation density is taken into account $2.1\times10^{-15}\ m^{-2}$ using Morito et.al study. XRD measurement to estimate variation of dislocation density is not taken into account due to lack of accuracy. Likewise recovery equation over-estimates the variation of dislocation density. Therefore its value considered small at 923 K (650 °C) tempering. The total summation of strength is converted into hardness through simple equation (5.11) (Nicolas 2009).

$$HV = \frac{1}{3}\sigma \tag{5.11}$$

where HV is hardness, and σ is strength.

The subgrain boundary contribution on strength is extracted by subtracting the calculated hardness from measured hardness (Kim, Boucard et al. 2014). It is also possible to calculate

this term by equation (1.19). The subgrain values are derived from grain growth modeled in section 5.9 and k_t equal 0.3 MNm^{-2}. It is expected to have same values in two last columns. The difference between them could probably belong to the contribution of strength due to strain hardening. Figure 5-14 displays the calculated hardness in compare with measured ones. Good correlation exists for two values.

Table 5-1 Hardening contribution of tempered sample in comparison with measured hardness.

Temp K (°C)	Time (Sec)	σ_{Fe} (MPa)	σ_C (MPa)	σ_{SS} (MPa)	σ_P (Orowan) (MPa)	σ_P (Orowan-Ashby) (Mpa)	σ_ρ (MPa)	σ_{tot} (MPa)
653	1	71.3	23.6	84.1	151.0	171.0	606.1	956.09
923	600	71.3	24.4	87.5	139.0	160.0	0.0	343.19
923	3600	71.3	24.9	100.6	90.8	113.2	0.0	309.90
923	14400	71.3	24.7	114.2	76.1	97.9	0.0	308.11
923	43200	71.3	24.3	131.0	49.9	68.9	0.0	295.39
923	86400	71.3	23.7	149.5	37.8	54.5	0.0	299.01
923	174000	71.3	23.2	172.1	34.9	51.0	0.0	317.54

Hardness Calculated (HV)	Hardness Experiment (HV)	$\frac{\sigma_g}{3}$ (subtraction) (MPa)	$\frac{\sigma_g}{3}$ Hall-Petch (MPa)
318.70	460	141.3	147
114.40	299.6	185.2	146
103.30	279.1	175.8	144
102.70	245.2	142.5	136
98.46	207.1	108.6	121
99.67	199.8	100.1	109
105.85	171.3	65.4	96

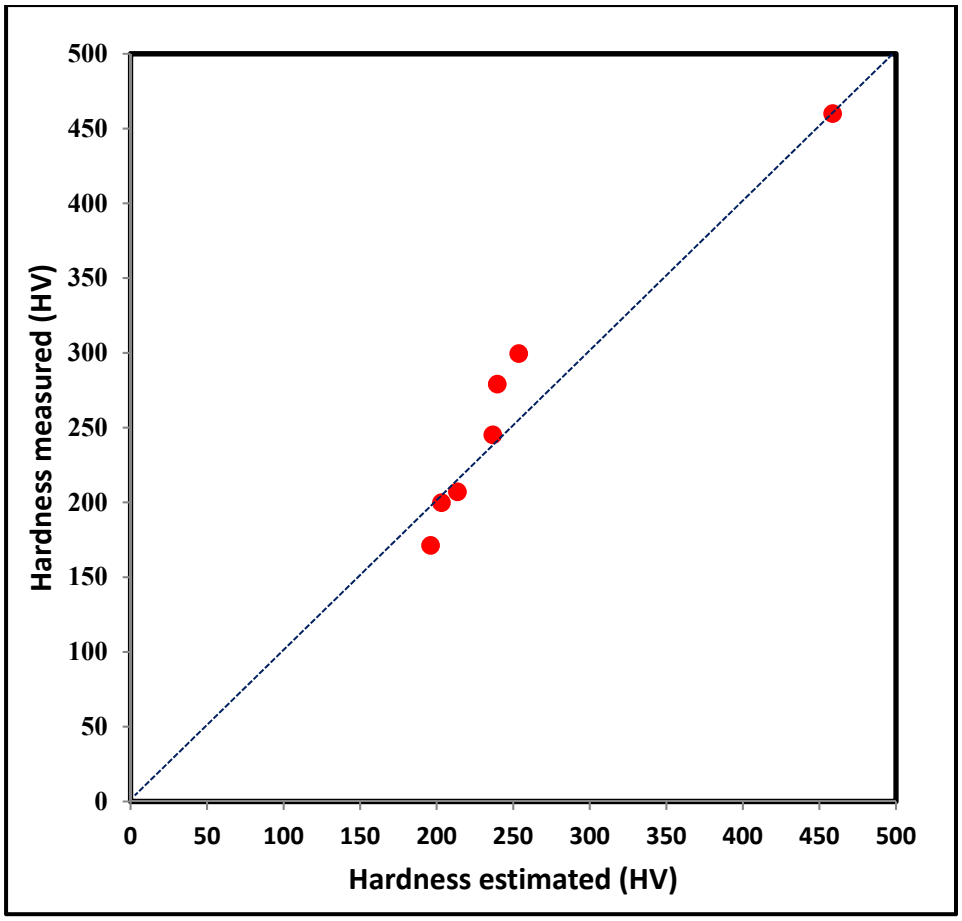

Figure 5-14 Comparison between hardness estimated by experimental data and measured ones.

5.11 Summary

From this chapter, it can be summarized that the prediction of cementite coarsening at 923K (650 °C) for AISI 4340 tempered steel tempered at 653K (380 °C) for 90 min (5400 second) with initial quenched and tempered hardness of 460 HV has been modeled well with DICTRA software. The evolution of chemical composition is predicted in cementite and matrix. These results show that coarsening resistance of the precipitates is controlled by alloying elements. Cr and Mn elements partition into cementite during early stage of the tempering, and Mo at longer exposure time. Ni and Si partition in the matrix also provided

some extra coarsening resistance at longer time. These elements decrease the carbon diffusive rates in matrix under PLE condition, and retard the displacement of the cementite interface. The far-field chemical compositions of alloying elements in matrix have been monitored using DICTRA software. It was shown that the coarsening resistance of AISI 4340 steel is not only due to carbide former elements Cr, Mn, and Mo, but also to Ni and Si, especially at later stages since Ni diffuses rather slowly. In addition, the kinetics coarsening of cementite is simulated based on extension of the Björklund model for ternary alloy system in multicomponent AISI 4340 steel. The resulting model took into account all elements for modeling the cementite coarsening and ferrite grain growth. The evolution of hardness in over-tempered area is predicted by application of microstructural features and presented strengthening model.

CONCLUSIONS

The kinetics of cementite coarsening at 832 K (550 °C), 923 K (650 °C), and 973 K (700 °C), for AISI 4340 tempered steel 460 HV generated at 653 K (380 °C) for 90 min has been studied with experimental investigations. Cementite coarsening during tempering of low-alloyed-medium carbon steel is modeled by DICTRA software. Moreover, extension of Björklund model was used to validate the coarsening results by DICTRA. An adequate consistency between experiment and modeling results are observed even if systematic shifts have been observed due to some simplification applied in the model and experimental analysis. However, some relevant important conclusions can be drawn from the presented work:

1. Based on the microstructural investigation of average precipitate radii, roundnesses, as well as quantities derived from the former (inter-particle spacing and number densities) have been documented for various exposure times, allowing to build a coarsening model.
2. Tempering experiments have shown that when supersaturation in the cementite reaches a critical level, spheroidization and coarsening of particles are taking place, followed by significant variations in morphology. The cementite particles change from plate like particle to the sphere, and small particles are dissolved in profit of larger ones, forming idiomorphic particles.
3. Although the measured coarsening rate constant K is in favor of a dominant Ostwald ripening mechanism, the measured particle distributions obtained using the Saltykov's correction method are not typical of LSW distributions as they reveal that 10% of the precipitates are larger than 1.5 the mean value.
4. Due to the low initial temperature used for tempering the studied steel (compare to the one used during over-tempering 653 K (380 °C) versus 923 K (650 °C)), the coarsening resistance of the precipitates is first controlled by Cr, Mn, and Mo partitions to cementite through the phase interface as the para equilibrium condition that prevail at 653 K (380 °C) is no more an option at 923 K (650 °C) as other

elements can diffuse. These Cr and Mn composition changes retard the coarsening of the cementite during the early stage, and Mo composition at later stage of the over-tempering. Some extra coarsening resistance is also provided by the Ni and Si partition in the matrix at longer exposure time. These elements decrease the carbon diffusive rates in matrix under PLE condition, and retarding the displacement of the cementite interface.

5. The present calculations have shown that in the present experimental condition, the remarkable resistance of the tempered cementite to coarsening is achieved thanks to the low temperature 653 K (380 °C) chosen for initial tempering to reach 460 HV. At this low temperature, only carbon can diffuse to reach thermodynamics stability, and any further high temperature exposure (over-tempering) will require a new set of thermodynamic condition to be reach, preventing rapid cementite growth.
6. The coarsening of cementite and grain growth are simulated based on extension of the Björklund model for ternary alloys system in multicomponent AISI 4340 steel by using efficient diffusion coefficient. The resulting model allows to get rid of spheroidization step, and it is very fast.
7. The hardness of over-tempered zone is calculated by using microstructural features and presented strengthening model. There exists good correlation between calculated and measured hardness.

RECOMMENDATIONS

The precipitates evolution during induction hardening is also suggested to study as follow:

1- It would be interesting to simulate isothermal tempering by a thermo-mechanical simulator such as Gleeble machine. As this machine can reach high temperature of over-tempered zone in very short time very similar condition during induction hardening heat treatment. To do so, this equipment should set first as a dilatometer. It allows to study high heating rate effect during induction hardening on transformation temperature A_{c1} and A_{c3}. It would reveal how these temperatures are shifted to higher temperature during this process. This part is already studied by (Clarke 2008) and in LOPFA group by (Ausseil 2016). This machine is then can be used to study the isothermal tempering with high heating rate to reveal the microstructural changes during fast tempering.

2- To better understand and validate the precipitation evolution during induction hardening which is a non-isothermal heat treatment advanced SAXS small angle X-Ray scattering techniques is recommended (De Geuser and Deschamps 2012). Density, volume fraction, size distribution of precipitates can be determined by in-situ measurement with the progress of quantitative analysis software. Further insight about this technique is studied by previous author (Nicolas 2009).

APPENDIX I

THE DECARBURIZED AND OXIDIZED LAYER MEASUREMENT

Introduction

The kinetic process during heat treatment of steel in which the interstitial carbon atoms diffuse from surface is called decarburization. Since the carbon contents and phases are mainly responsible for the strength of steel, they should be monitored during heat treatment. Therefore, some precautions to take control for removing this deleterious effect whether in industrial procedure or experimental scale would be necessary. Injection of neutral gas during heat treatment procedure to reduce the concentration of oxygen atoms in furnace, or make vacuum environment are some recommended solutions for this phenomena. Due to tempering in furnace with atmosphere environment, the oxidation and decarburization layer were measured to confirm that the only reason for loss of hardness is because of spheroidization and coarsening of precipitates.

Experimental procedure

Tempered samples were tested to measure the decarburized and probably existence of oxidized surface layer. The usual procedure for sample preparation included of mounting, grinding, polishing and etching was done to reveal the microstructure. Then, measurement was done on the images was took by optical microscope.

Result and discussion

a) Decarburization test for tempered sample

The initial quenched and tempered sample after tempering procedure, due to high temperature of second stage of tempering, may suffer from decarburization. A distinguished white ferrite layer created at the surface layer of this material is representative of decarburized layer. This effect on surface region of tempered samples were illustrated on Figure (I)- 1. As it can be seen, there existed very small white ferrite surface layer, which is not uniform in all cases. These measurements were applied on tempered samples at high

temperature according to methods of measuring decarburization and ASTM E 1077 - Standard Test Methods for Estimating the Depth of Decarburization of Steel Specimens.

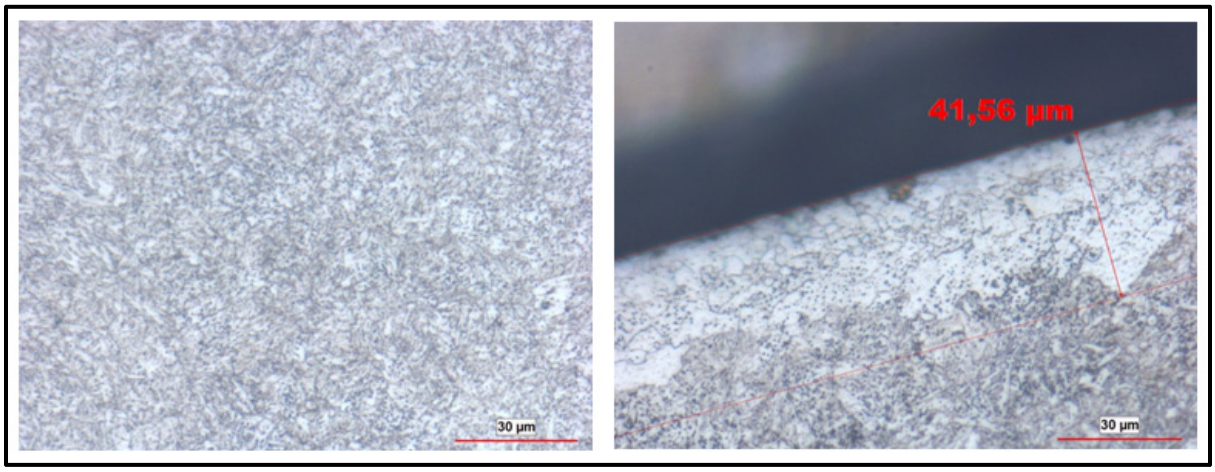

Figure (I)- 1 Illustration of microstructure by optical microscope, for the most frequent decarburized layer during tempering at 700 °C for 12 min with atmosphere furnace, a) Center b) Edge

As it can be seen a very tiny and small white layer about maximum up to 45 micron existed in some parts. There is no dark layer, which is represented of oxidized layer. Then if the sample is looked near the center, it can be safe from composition changes for all conditions. As a complementary procedure the decarburized layer was predicted by DICTRA simulation in Figure (I)- 2. This can be supported microscopic observation in approximately good agreement.

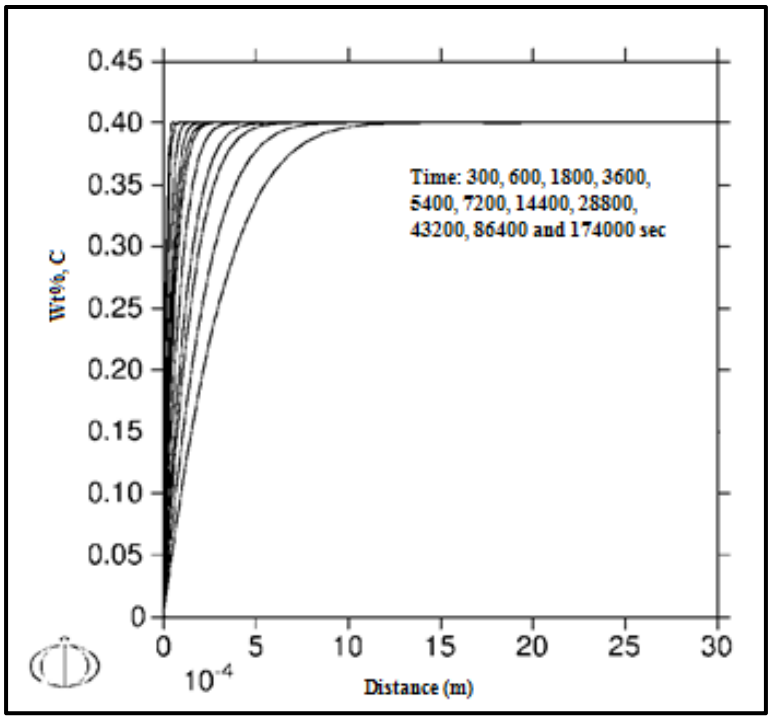

Figure (I)- 2 Illustration of modeling for decarburized layer after tempering procedure at 973 K (700 °C) temperature and long times

APPENDIX II

THERMO-CALC: PARAEQUILIBRIUM CALCULATION (Cr-Mn-Ni-Si)

```
Thermo-Calc 3.1 (build 6388) on WinNT 64-bit word length
 Compiler: Intel(R) Visual Fortran Composer Version 12.1.3.300    Build 20120130
 License library version: 8.5.1.0017
 Linked: Thu Nov 28 13:20:51 2013
 Copyright (1993,2008) Foundation for Computational Thermodynamics,
 Stockholm, Sweden
 Only for use at ETS - Montreal - ME
 Local contact Johann Hamel-Akre

SYS:GO DA
 THERMODYNAMIC DATABASE module
 Current database: TCS Steels/Fe-Alloys Database v7.0

 VA  DEFINED
 L12_FCC             B2_BCC              B2_VACANCY
 HIGH_SIGMA          DICTRA_FCC_A1  REJECTED
TDB_TCFE7:DEF-SP FE C CR MN NI SI
 FE                  C                   CR
 MN                  NI                  SI
     DEFINED
TDB_TCFE7:REJ PH*
 GAS:G               LIQUID:L                                        BCC_A2
 FCC_A1              HCP_A3
            DIAMOND_FCC_A4
 GRAPHITE            CEMENTITE                       M23C6
 M7C3                M5C2                            M3C2
 KSI_CARBIDE         A1_KAPPA                        KAPPA
 FE4N_LP1            FECN_CHI                        SIGMA
 CHI_A12             LAVES_PHASE_C14                 M3SI
 G_PHASE             CR3SI                           FE2SI
 MSI                 M5SI3                           NBNI3
 NI3TI               AL4C3                           FE8SI2C
 SIC  REJECTED
TDB_TCFE7:REST PH BCC CEM
 BCC_A2              CEMENTITE  RESTORED
TDB_TCFE7:GET
 REINITIATING GES5 .....
 ELEMENTS .....
 SPECIES ......
```

```
 PHASES .....
 PARAMETERS ...
 FUNCTIONS ....

TDB_TCFE7:GO P-3

  POLY version  3.32
POLY_3:S-C T=653 N=1 P=101325
POLY_3:S-C W(C)=0.4E-2 W(CR)=0.8E-2 W(MN)=0.7E-2 W(NI)=1.82E-2
W(SI)=0.225E-2
POLY_3:L-C
 T=653, N=1, P=1.01325E5, W(C)=4E-3, W(CR)=8E-3, W(MN)=7E-3, W(NI)=1.82E-2,
    W(SI)=2.25E-3
 DEGREES OF FREEDOM 0
POLY_3:C-E
 Using global minimization procedure
 Calculated                2975  grid points in                    0  s
 Found the set of lowest grid points in                    0  s
 Calculated POLY solution       0 s, total time     0  s
POLY_3:L-E
OUTPUT TO SCREEN OR FILE /SCREEN/:
Options /VWCS/:
 Output from POLY-3, equilibrium =      1, label A0  , database: TCFE7

 Conditions:
 T=653, N=1, P=1.01325E5, W(C)=4E-3, W(CR)=8E-3, W(MN)=7E-3, W(NI)=1.82E-2,
    W(SI)=2.25E-3
 DEGREES OF FREEDOM 0

 Temperature    653.00 K (   379.85 C),  Pressure  1.013250E+05
 Number of moles of components  1.00000E+00,  Mass in grams  5.49324E+01
 Total Gibbs energy -2.31128E+04,  Enthalpy  1.00297E+04,  Volume  7.10630E-06

 Component          Moles          W-Fraction       Activity         Potential        Ref.stat
 C                  1.8294E-02     4.0000E-03       1.3627E+00       1.6800E+03       SER
 CR                 8.4518E-03     8.0000E-03       1.3400E-04       -4.8417E+04      SER
 FE                 9.4482E-01     9.6055E-01       1.6738E-02       -2.2207E+04      SER
 MN                 6.9993E-03     7.0000E-03       6.5770E-05       -5.2281E+04      SER
 NI                 1.7035E-02     1.8200E-02       7.2784E-04       -3.9230E+04      SER
 SI                 4.4007E-03     2.2500E-03       8.5431E-14       -1.6338E+05      SER

 BCC_A2                    Status ENTERED     Driving force  0.0000E+00
 Moles 9.2683E-01, Mass 5.1684E+01, Volume fraction 9.3887E-01  Mass fractions:
 FE  9.77135E-01  SI  2.39140E-03  CR  2.79899E-04
 NI  1.91243E-02  MN  1.06865E-03  C   4.94065E-07
```

```
CEMENTITE                Status ENTERED     Driving force  0.0000E+00
 Moles 7.3168E-02, Mass 3.2480E+00, Volume fraction 6.1127E-02  Mass fractions:
 FE  6.96632E-01  MN  1.01385E-01  NI  3.49137E-03
 CR  1.30849E-01  C   6.76435E-02  SI  4.74524E-13
POLY_3:CH-ST
For phases, species or components? /PHASES/:COMPO
Name(s):C
Status: /ENTERED/:SPE
POLY_3:C-E
 Using global minimization procedure
 Calculated              2975  grid points in                1  s
 Found the set of lowest grid points in                0  s
 Calculated POLY solution       0 s, total time     1  s
POLY_3:L-E,,,
 Output from POLY-3, equilibrium =     1, label A0  , database: TCFE7

 Conditions:
 T=653, N=1, P=1.01325E5, W(C)=4E-3, W(CR)=8E-3, W(MN)=7E-3, W(NI)=1.82E-2,
    W(SI)=2.25E-3
 DEGREES OF FREEDOM 0

 Temperature    653.00 K (   379.85 C), Pressure  1.013250E+05
 Number of moles of components 1.00000E+00, Mass in grams 5.49360E+01
 Total Gibbs energy -2.31093E+04, Enthalpy 1.00308E+04, Volume 7.10665E-06

 Component            Moles              W-Fraction         Activity    Potential  Ref.stat
 C                    1.8222E-02         4.0000E-03         1.3627E+00
            1.6804E+03           SER
 CR                   8.4187E-03         8.0000E-03         1.3398E-04          -
4.8418E+04           SER
 FE                   9.4504E-01         9.6455E-01         1.6739E-02          -
2.2206E+04           SER
 MN                   6.9719E-03         7.0000E-03         6.5740E-05          -
5.2284E+04           SER
 NI                   1.6968E-02         1.8200E-02         7.2511E-04
            3.9250E+04           SER
 SI                   4.3834E-03         2.2500E-03         8.5130E-14          -
1.6339E+05           SER

 BCC_A2                   Status ENTERED     Driving force  0.0000E+00
 Moles 9.2712E-01, Mass 5.1701E+01, Volume fraction 9.3912E-01  Mass fractions:
 FE  9.77227E-01  SI  2.38127E-03  CR  2.79705E-04
 NI  1.90442E-02  MN  1.06716E-03  C   4.94639E-07

 CEMENTITE                Status ENTERED     Driving force  0.0000E+00
```

```
 Moles 7.2881E-02, Mass 3.2352E+00, Volume fraction 6.0884E-02  Mass fractions:
 FE  6.96710E-01  MN  1.01336E-01  NI  3.47780E-03
 CR  1.30833E-01  C   6.76434E-02  SI  4.74523E-13
POLY_3: ADV
Which option? /STEP_AND_MAP/:PARA

This command calculates a paraequilibrium between two phases.
You must calculate an equilibrium with the overall composition first.
Name of first phase:CEMENTITE
Name of second phase:BCC
Fast diffusing component: /C/:
Fast diffusing component: /NONE/:
 NP(CEMENTITE) =   0.0557 with U-fractions C  =  3.33333E-01
 NP(BCC) =   0.9443 with U-fractions C  =  1.10433E-05
 All other compositions the same in both phases
 Note: LIST-EQUILIBRIUM is not relevant
POLY_3:SH VM(CEMENTITE)
VM(CEMENTITE)=7.9157887E-6
```

APPENDIX III

THERMO-CALC: PARAEQUILIBRIUM CALCULATION (Cr-Mn-Mo-Ni)

```
Thermo-Calc 3.1 (build 6388) on WinNT 64-bit word length
 Compiler: Intel(R) Visual Fortran Composer Version 12.1.3.300 Build 20120130
 License library version: 8.5.1.0017
 Linked: Thu Nov 28 13:20:51 2013
 Copyright (1993,2008) Foundation for Computational Thermodynamics,
 Stockholm, Sweden
 Only for use at ETS - Montreal - ME
 Local contact Johann Hamel-Akre

SYS: go da
 THERMODYNAMIC DATABASE module
 Current database: TCS Steels/Fe-Alloys Database v7.0

 VA  DEFINED
 L12_FCC                 B2_BCC                  B2_VACANCY
 HIGH_SIGMA              DICTRA_FCC_A1           REJECTED
TDB_TCFE7:def-sp fe c cr mn mo ni
 FE              C               CR
 MN              MO              NI
   DEFINED
TDB_TCFE7:rej ph *
 GAS:G           LIQUID:L        BCC_A2
 FCC_A1          HCP_A3          DIAMOND_FCC_A4
 GRAPHITE        CEMENTITE       M23C6
 M7C3            M6C             M5C2
 M3C2            MC_ETA          MC_SHP
 KSI_CARBIDE     A1_KAPPA        KAPPA
 Z_PHASE         FE4N_LP1        FECN_CHI
 SIGMA           MU_PHASE        P_PHASE
 R_PHASE         CHI_A12         LAVES_PHASE_C14
 G_PHASE         CR3SI           NBNI3
 NI3TI  REJECTED
TDB_TCFE7:rest ph bcc cem
 BCC_A2          CEMENTITE  RESTORED
TDB_TCFE7:get
 REINITIATING GES5 .....
 ELEMENTS .....
 SPECIES ......
 PHASES .......
```

```
 PARAMETERS ...
 FUNCTIONS ....

TDB_TCFE7:go p-3

 POLY version  3.32
POLY_3:s-c T=653 n=1 P=101325
POLY_3:S-C W(C)=0.4E-2 W(CR)=0.8E-2 W(MN)=0.7E-2 W(MO)=0.25E-2
W(NI)=1.82E-2
POLY_3:L-C
 T=653, N=1, P=1.01325E5, W(C)=4E-3, W(CR)=8E-3, W(MN)=7E-3, W(MO)=2.5E-3,
    W(NI)=1.82E-2
 DEGREES OF FREEDOM 0
POLY_3:C-E
 Using global minimization procedure
 Calculated                2975  grid points in                    0  s
 Found the set of lowest grid points in                    0  s
 Calculated POLY solution       0 s, total time     0  s
POLY_3:L-E
OUTPUT TO SCREEN OR FILE /SCREEN/:
Options /VWCS/:
 Output from POLY-3, equilibrium =     1, label A0  , database: TCFE7

 Conditions:
 T=653, N=1, P=1.01325E5, W(C)=4E-3, W(CR)=8E-3, W(MN)=7E-3, W(MO)=2.5E-3,
    W(NI)=1.82E-2
 DEGREES OF FREEDOM 0

 Temperature    653.00 K (   379.85 C), Pressure 1.013250E+05
 Number of moles of components 1.00000E+00, Mass in grams 5.51096E+01
 Total Gibbs energy -2.24913E+04, Enthalpy 1.06718E+04, Volume 7.11384E-06

 Component                      Moles      W-Fraction          Activity    Potential   Ref.stat
 C                      1.8353E-02          4.0000E-03          1.2678E+00
          1.2881E+03           SER
 CR                     8.4791E-03          8.0000E-03          1.4023E-04          -
4.8171E+04           SER
 FE                     9.4762E-01          9.6030E-01          1.6782E-02          -
2.2192E+04           SER
 MN                     7.0219E-03          7.0000E-03          6.7264E-05          -
5.2159E+04           SER
 MO                     1.4360E-03          2.5000E-03          1.8200E-03          -
3.4254E+04           SER
 NI                     1.7090E-02          1.8200E-02          8.0313E-04          -
3.8695E+04           SER
```

```
 BCC_A2                        Status ENTERED     Driving force  0.0000E+00
 Moles 9.2660E-01, Mass 5.1824E+01, Volume fraction 9.3859E-01  Mass fractions:
 FE  9.78185E-01  MO  1.39087E-03  CR  2.78613E-04
 NI  1.91085E-02  MN  1.03607E-03  C   5.12575E-07

 CEMENTITE                     Status ENTERED     Driving force  0.0000E+00
 Moles 7.3403E-02, Mass 3.2859E+00, Volume fraction 6.1408E-02  Mass fractions:
 FE  6.78221E-01  MN  1.01060E-01  MO  1.99925E-02
 CR  1.29777E-01  C   6.70777E-02  NI  3.87173E-03
POLY_3:CH-ST
For phases, species or components? /PHASES/:COMPO
Name(s):C
Status: /ENTERED/:C-E

 *** ERROR  1654 IN QEQUIM
 *** NO SUCH STATUS
POLY_3:CH-ST
For phases, species or components? /PHASES/:COMPO
Name(s):C
Status: /ENTERED/:SPE
POLY_3:C-E
 Using global minimization procedure
 Calculated                2975  grid points in                0  s
 Found the set of lowest grid points in                  0  s
 Calculated POLY solution       0 s, total time     0  s
POLY_3:L-E,,,
 Output from POLY-3, equilibrium =     1, label A0  , database: TCFE7

 Conditions:
 T=653, N=1, P=1.01325E5, W(C)=4E-3, W(CR)=8E-3, W(MN)=7E-3, W(MO)=2.5E-3,
    W(NI)=1.82E-2
 DEGREES OF FREEDOM 0

 Temperature    653.00 K (   379.85 C), Pressure 1.013250E+05
 Number of moles of components  1.00000E+00,  Mass in grams  5.51125E+01
 Total Gibbs energy -2.24902E+04, Enthalpy 1.06704E+04, Volume 7.11417E-06

 Component                     Moles      W-Fraction           Activity   Potential  Ref.stat
 C                         1.8281E-02      4.0000E-03           1.2681E+00
           1.2895E+03          SER
 CR                        8.4457E-03      8.0000E-03           1.4019E-04          -
4.8172E+04          SER
 FE                        9.4783E-01      9.6430E-01           1.6784E-02          -
2.2192E+04          SER
```

```
 MN                 6.9943E-03          7.0000E-03          6.7230E-05          -
5.2162E+04          SER
 MO                 1.4304E-03          2.5000E-03          1.8159E-03          -
3.4266E+04          SER
 NI                 1.7023E-02          1.8200E-02          7.9980E-04          -
3.8718E+04          SER

 BCC_A2                    Status ENTERED     Driving force  0.0000E+00
 Moles 9.2689E-01, Mass 5.1840E+01, Volume fraction 9.3884E-01  Mass fractions:
 FE  9.78270E-01  MO  1.38775E-03  CR  2.78434E-04
 NI  1.90286E-02  MN  1.03477E-03  C   5.13055E-07

 CEMENTITE                 Status ENTERED     Driving force  0.0000E+00
 Moles 7.3115E-02, Mass 3.2729E+00, Volume fraction 6.1164E-02  Mass fractions:
 FE  6.78341E-01  MN  1.01013E-01  MO  1.99491E-02
 CR  1.29764E-01  C   6.70788E-02  NI  3.85511E-03
POLY_3:ADV
Which option? /STEP_AND_MAP/:PARA

This command calculates a paraequilibrium between two phases.
You must calculate an equilibrium with the overall composition first.
Name of first phase:CEMENTITE
Name of second phase:BCC
Fast diffusing component: /C/:
Fast diffusing component: /NONE/:
 NP(CEMENTITE) =   0.0558 with U-fractions C  =  3.33333E-01
 NP(BCC) =   0.9442 with U-fractions C  =  7.63767E-06
 All other compositions the same in both phases
 Note: LIST-EQUILIBRIUM is not relevant
```

APPENDIX IV

DICTRA: PURE GROWTH CALCULATION (Cr-Mn-Ni-Si)

```
@@----------------------------------------------------------------------------------------------------------
@@      Setup File for Calculating the Pure Growth of Spherical cementite carbides in a
@@                                  martensitic matrix.
@@----------------------------------------------------------------------------------------------------------

@@
@@ RETRIEVE DATA FROM DATABASE
@@
go da
switch tcfe7
def-species fe c cr mn ni si
rej ph * all
res ph bcc cem
get

@@
@@ SWITCH TO MOBILITY DATABASE TO RETRIEVE MOBILITY DATA
@@
app
mobfe2
def-sys fe c cr mn ni si
rej ph * all
res ph bcc cem
get


@@
@@ ENTER THE DICTRA MONITOR
@@
go d-m

@@
@@  ENTER GLOBAL CONDITION T
@@
s-cond glob t 0 923; * N

@@
@@ ENTER REGIONS CEMENTITE AND MART
@@
enter-region cementite
```

```
enter-region mart

@@
@@ ENTER GEOMTRICAL GRIDS INTO THE REGIONS
@@
enter-grid
cementite
5.82E-8
geo
12
0.8

enter-grid
mart
8.9138E-8
geo
36
1.1

@@
@@ ENTER PHASES INTO REGIONS
@@
enter-phase active cementite matrix cem

enter-phase active mart matrix bcc#1


@@
@@ ENTER INITIAL COMPOSITIONS IN THE PHASES
@@ FOR PARAEQUILIBRIUM CEMENTITE
enter-composition
cementite
cem
m-f
cr          lin          8.4187E-03          8.4187E-03
Mn          lin          6.9719E-03          6.9719E-03
Ni          lin          1.6968E-02          1.6968E-02
Si          lin          4.3834E-03          4.3834E-03

ent-composition
mart
bcc#1
fe
m-f
cr          lin          8.4187E-03          8.4187E-03
Mn          lin          6.9719E-03          6.9719E-03
Ni          lin          1.6968E-02          1.6968E-02
Si          lin          4.3834E-03          4.3834E-03
C           lin          1.104317E-5         1.104317E-5
```

```
@@
@@ SET SPHERICAL GEOMETRY
@@
ent-geo 2

@@
@@ SET THE SIMULATION TIME AND VARIOUS SIMULATION PARAMETERS
@@
set-simulation-time 1E5




s-s-cond



y


y
1.0



@@
@@ SAVE THE SETUP ON A NEW STORE FILE AND EXIT
@@
save
y



set-inter
```

APPENDIX V

DICTRA: PURE GROWTH CALCULATION (Cr-Mn-Mo-Ni)

```
@@----------------------------------------------------------------------------------------------------
@@ Setup File for Calculating the Pure Growth of Spherical Cementite Carbides in a
@@                                   Martensitic Matrix
@@----------------------------------------------------------------------------------------------------

@@
@@ RETRIEVE DATA FROM DATABASE
@@
go da
switch tcfe7
def-species fe c cr mn mo ni
rej ph * all
res ph bcc cem
get

@@
@@ SWITCH TO MOBILITY DATABASE TO RETRIEVE MOBILITY DATA
@@
app
mobfe2
def-sys fe c cr mn mo ni
rej ph * all
res ph bcc cem
get


@@
@@ ENTER THE DICTRA MONITOR
@@
go d-m

@@
@@  ENTER GLOBAL CONDITION T
@@
s-cond glob t 0 923; * N

@@
```

```
@@ ENTER REGIONS CEMENTITE AND MART
@@
enter-region cementite
enter-region mart


@@
@@ ENTER GEOMTRICAL GRIDS INTO THE REGIONS
@@
enter-grid
cementite
5.82E-8
geo
12
0.8

enter-grid
mart
8.9138E-8
geo
36
1.1

@@
@@ ENTER PHASES INTO REGIONS
@@
enter-phase active cementite matrix cem

enter-phase active mart matrix bcc#1


@@ ENTER INITIAL COMPOSITIONS IN THE PHASES
@@ FOR PARAEQUILIBRIUM CEMENTITE: cr lin 0.004 0.004
enter-composition
cementite
cem
m-f
Cr      lin     8.4457E-03      8.4457E-03
Mn      lin     6.9943E-03      6.9943E-03
Mo      lin     1.4304E-03      1.4304E-03
Ni      lin     1.7023E-02      1.7023E-02

ent-composition
mart
bcc#1
```

```
fe
m-f
Cr          lin         8.4457E-03          8.4457E-03
Mn          lin         6.9943E-03          6.9943E-03
Mo          lin         1.4304E-03          1.4304E-03
Ni          lin         1.7023E-02          1.7023E-02
C           lin         7.637612E-6         7.637612E-6



@@
@@ SET SPHERICAL GEOMETRY
@@
ent-geo 2

@@
@@ SET THE SIMULATION TIME AND VARIOUS SIMULATION PARAMETERS
@@
set-simulation-time 1E5




s-s-cond



y


y
1.0



@@ SAVE THE SETUP ON A NEW STORE FILE AND EXIT
save
y


set-inter
```

APPENDIX VI

DICTRA: PURE GROWTH PLOT (1)

```
@@ ----------------------------------------------------------------------------------------------------
@@                    Macro File to Save Supersaturation Changes: Matrix
@@ ----------------------------------------------------------------------------------------------------

go d-m

read

post

s-d-a x time

s-pl-co integral

ent-sym fun xcrm=in(bcc#1,cr)/in(bcc#1)*100;

ent-sym fun xcm=in(bcc#1,c)/in(bcc#1)*100;

ent-sym fun xmnm=in(bcc#1,mn)/in(bcc#1)*100;

ent-sym fun xnim=in(bcc#1,ni)/in(bcc#1)*100;

ent-sym fun xsim=in(bcc#1,si)/in(bcc#1)*100;

s-d-a y xcrm
```

```
pl,,

dump-d png hi

s-d-a y xcm

pl,,

dump-d png hi

s-d-a y xnim

pl,,

dump-d png hi

s-d-a y xmnm

pl,,

dump-d png hi

s-d-a y xsim

pl,,

dump-d png hi

set-inter
```

APPENDIX VII

DICTRA: PURE GROWTH PLOT (2)

```
@@ ----------------------------------------------------------------------------------------------------
@@                    Macro File to Save Supersaturation Changes: Interface
@@ ----------------------------------------------------------------------------------------------------

go d-m

read

post

s-d-a x time

s-pl-co interface last

s-ax-ty x log

s-s-s x n 1 1E5

s-d-a y m-p cr

pl,,

dump-d png hi

s-d-a y m-p mn
```

pl,,

dump-d png hi

s-d-a y m-p si

pl,,

dump-d png hi

s-d-a y m-p ni

pl,,

dump-d png hi

s-d-a y m-p c

pl,,

dump-d png hi

set-inter

APPENDIX VIII

DICTRA: COARSENING CALCULATION (Cr-Mn-Ni-Si)

```
@@----------------------------------------------------------------------------------------------------
@@      Setup File for Calculating the Impingement of Spherical Cementite Carbides
@@                                    in a Martensitic Matrix.
@@----------------------------------------------------------------------------------------------------

@@
@@ RETRIEVE DATA FROM DATABASE
@@
go da
switch tcfe7
def-species fe c cr mn ni si
rej ph * all
res ph bcc cem
get

@@
@@ SWITCH TO MOBILITY DATABASE TO RETRIEVE MOBILITY DATA
@@
app
mobfe2
def-sys fe c cr mn ni si
rej ph * all
res ph bcc cem
get


@@
@@ ENTER THE DICTRA MONITOR
@@
go d-m

@@
@@  ENTER GLOBAL CONDITION T
@@
s-cond glob t 0 923; * N

@@
```

```
@@ ENTER REGIONS CEMENTITE AND MART
@@
enter-region cementite
enter-region mart


@@
@@ ENTER GEOMTRICAL GRIDS INTO THE REGIONS
@@
enter-grid
cementite
5.80266E-08
geo
47
0.8

enter-grid
mart
8.93114E-08
geo
57
1.1

@@
@@ ENTER PHASES INTO REGIONS
@@
enter-phase active cementite matrix cem

enter-phase active mart matrix bcc#1


@@
@@ ENTER INITIAL COMPOSITIONS IN THE PHASES
@@ PURE GROWTH

enter-composition
cementite
cem
m-f
cr              read
Mn              read
Ni              read
Si              read

ent-composition
```

```
mart
bcc#1
fe
m-f
cr              read
Mn              read
Ni              read
Si              read
C               read


@@
@@ SET SPHERICAL GEOMETRY
@@
ent-geo 2

@@
@@ ENTER THE INTERFACIAL ENERGY BETWEEN 0.3 TO 0.7.
@@ ENTER THE MOLAR VOLUME PER SUBSTITUTIONAL ATOM 2.4
@@ TRANSFORMATION TO MOLAR VOLUME PER SUBSTITUTIONAL
@@ ATOM IS 4/3
@@
set-surf 2*2.4* (SURFACE TENSION) *(4/3)/X;


@@
@@ ENABLE THE SIMPLIFIED MODEL THE COARSENING (OSTWALD-RIPENING)
@@
coarse YES


@@
@@ SET THE SIMULATION TIME AND VARIOUS SIMULATION PARAMETERS
@@
set-simulation-time 1E6


0.00001


s-s-cond
```

158

y

y
1.0

@@
@@ SAVE THE SETUP ON A NEW STORE FILE AND EXIT
@@
save
y

set-inter

APPENDIX IX

DICTRA: COARSENING CALCULATION (Cr-Mn-Mo-Ni)

```
@@----------------------------------------------------------------------------------------------------
@@      Setup file for Calculating the Impingement of Spherical Cementite Carbides in a
@@                                        Martensitic Matrix
@@----------------------------------------------------------------------------------------------------

@@
@@ RETRIEVE DATA FROM DATABASE
@@
go da
switch tcfe7
def-species fe c cr mn mo ni
rej ph * all
res ph bcc cem
get

@@
@@ SWITCH TO MOBILITY DATABASE TO RETRIEVE MOBILITY DATA
@@
app
mobfe2
def-sys fe c cr mn mo ni
rej ph * all
res ph bcc cem
get


@@
@@ ENTER THE DICTRA MONITOR
@@
go d-m

@@
@@  ENTER GLOBAL CONDITION T
@@
s-cond glob t 0 923; * N

@@
```

```
@@ ENTER REGIONS cementite AND mart
@@
enter-region cementite
enter-region mart


@@
@@ ENTER GEOMTRICAL GRIDS INTO THE REGIONS
@@

@@IT WILL HOWEVER PERFORM THE CALCULATIONS ON A MAXIMUM SIZE
@@ PARTICLE WHICH IS ASSUMED TO 1.5 TIMES THE AVERAGE SIZE. THE
@@SURROUNDING TEMPERED MARTENSITE MATRIX SIZE IS CHOOSEN TO
@@ MAINTAIN THE AVERAGE COMPOSITION
enter-grid
cementite
5.80135E-08
geo
42
0.8

enter-grid
mart
8.93244E-08
geo
51
1.1

@@
@@ ENTER PHASES INTO REGIONS
@@
enter-phase active cementite matrix cem

enter-phase active mart matrix bcc#1


@@
@@ ENTER INITIAL COMPOSITIONS IN THE PHASES
@@ PURE GROWTH

enter-composition
cementite
cem
m-f
cr read
```

Mn read
Mo read
Ni read

ent-composition
mart
bcc#1
fe
m-f
cr read
Mn read
Mo read
Ni read
C read

@@
@@ SET SPHERICAL GEOMETRY
@@
ent-geo 2

@@
@@ ENTER THE INTERFACIAL ENERGY BETWEEN 0.3 TO 0.7.
@@ ENTER THE MOLAR VOLUME PER SUBSTITUTIONAL ATOM 2.4
@@ TRANSFORMATION TO MOLAR VOLUME PER SUBSTITUTIONAL
@@ ATOM IS 4/3
@@
@@
set-surf 2*2.4* (SURFACE TENSION) *(4/3)/X;

@@
@@ ENABLE THE SIMPLIFIED MODEL THE COARSENING (OSTWALD-RIPENING)
@@
coarse YES

@@
@@ SET THE SIMULATION TIME AND VARIOUS SIMULATION PARAMETERS
@@
set-simulation-time 1E6

0.00001

s-s-cond

y

y
1.0

@@
@@ SAVE THE SETUP ON A NEW STORE FILE AND EXIT
@@
save
y

set-inter

APPENDIX X

DICTRA: COARSENING PLOT

```
@@----------------------------------------------------------------------------------------------------
@@                    File for Generating Graphical Output for Coarsening
@@----------------------------------------------------------------------------------------------------

@@
@@ go to the dictra monitor and read the store result file
@@
Go d-m
Read
@@
@@ go to the post processor
@@
Post

@@
@@ we will now plot the average particle size cubed as this assumed to scale linearly with
@@ time, we must then enter a function to be able to access this quantity we also want to
@@ plot this quantity versus time in hours so will enter a function for this
@@
Enter-symbol func rr3=(poi(cementite,u)/1.5)**3;
Enter-symbol func hours=time/3600;
S-d-a x hours
S-d-a y rr3

@@
@@ as we are plotting functions on both axis we must explicitly define the independent
@@ variable and the plot condition
@@
S-ind time
S-p-c inter
Cementite upper


Set-axis-text-status x n
Time (hours)

@@
```

@@ this fairly cryptical axis text will give a nice notation for the average radius cubed once
@@ the plot is printed. For more information on text manipulation in the post processor the
@@ reader is referred to the section on dataplot graphical language in the thermo-calc users
@@ guide.
@@

Set-axis-text-status y n
^ccrm ^up3$ (m^up3$)

Set-title coarsening of cementite in 4340 alloy

Plot

S-ax-ty x log

Plot

Ent-sym tab radtime=hours rr3;

Tabul radtime file

Set-inter

APPENDIX XI

CEMENTITE COARSENING MODEL

```
@@----------------------------------------------------------------------------------------------------
@@    Implementation of a Coarsening Model for Cementite in 4340 Steel (Python Code)
@@----------------------------------------------------------------------------------------------------

from __future__ import division
import pandas as pd
import numpy as np

from scipy.constants import R
from scipy.integrate import odeint

import matplotlib.pyplot as plt

# Thermodynamic and kinetic data
# Thermodynamic: partition coefficients in ferrite
def partition_coeffs(T):
    partition_data = pd.read_csv("partition_data.csv")
    DG = 1540.0 + 1.47 * T
    k_si = 0.05
    k_m = np.exp((partition_data.A + partition_data.B * T - DG) * 4.184 / R / T)
    labels = [element.upper() for element in partition_data.M] + ['SI']
    k_p = pd.Series(np.concatenate((k_m.values, [k_si])), index=labels)

    return k_p

def diffusion_data(T):
    """ Calculate the mobilities in alpha-iron (tracers) for a given system sys
```

```
        elements in sys are Fe, C, Mn, Si, Ni, Cr, Mo, Cu """
    MOB = dict()
    diff_coeffs = pd.read_csv("bulk_diff_coeffs.csv")
    MOB['FE'] = 121e-4 * np.exp(-281.6e3 / R / T)
    X = 1e4 / T
    MOB['C'] = 10 ** (-4.9064 - 0.5199 * X + 1.61e-3 * X ** 2)
    labels = [element for element in diff_coeffs.M] + ['FE', 'C']
    D = diff_coeffs.D0 * np.exp(-diff_coeffs.Q / R / T)
    D = pd.Series(np.concatenate((D.values, [MOB['FE'], MOB['C']])), index=labels)
    # elt_labels = pd.Series(np.concatenate((diff_coeffs.M, ['FE', 'C'])))

    return D

def weight_to_mole(sys):
    """ Converts weight fractions to mole fractions.
        sys = dict('elt' : concentration), where elt is any element contained
        in the UNARY_PROPERTIES.MTC file """
    # Open and read the molar masses for the element in the system
    ppt_file = open('UNARY_PROPERTIES.MTC', 'r')
    ppt_li = ppt_file.readlines()
    ppt_file.close()

    MM = dict()

    # Read molar masses in file
    for line in ppt_li:
        li = line.split()
        if len(li) > 4 and li[1] in sys.keys():
            MM[li[1]] = float(li[3])
    tot = 0.0
```

```
    for i, elt in enumerate(sys):
        tot = tot + float(sys[elt]) / MM[elt]
    mol = dict()
    for i, elt in enumerate(sys):
        mol[elt] = sys[elt] / MM[elt] / tot

    return mol

def nominal_composition(content):
    content["FE"] = 1.0
    for elt in content:
        if elt not in "FE":
            content["FE"] -= content[elt]
    return weight_to_mole(content)

def get_system_data(data_type, system_elements):
    return pd.Series([data_type[element] for element in system_elements])



def coarsening_with_ferrite_growth(y, t, *args):
    """ The coarsening rate differential equations when
        ferrite grain coarsening is taken into account. """
    T, cem_fr, sig, c_m, k_p, d_l = args

    from scipy.constants import R
    Vcem = 24.0e-6
    # GB movement kinetic factor
    k = 3.3e-8 * np.exp(-171544 / R / T)
    # Gl free growth for a spherical grain containing a fraction f of cementite
    G_l = 8.0 * y[1] / 3.0 / cem_fr
```

```
    # K0 cementite free growth factor
    K0 = 8.0 * sig * Vcem / 81.0 / R / T
    # D_eff: effective diffusivity in matrix and dislocation pipes
    d_m = d_l + 2.0 * 5.4e-14 * np.exp(-171544.0 / R / T) / y[0]
    D_eff = 1. / (c_m * (1 - k_p) ** 2 / d_m).sum()

    dydt = [k * (1.0 - y[0] / G_l) / 2.0 / y[0],
            K0 * D_eff / y[1] ** 2]
    return dydt

if __name__ == '__main__':

    # Temperature (K) (constant for now)
    T = 923.0
    # Get thermodynamic and kinetic data
    eq_data = partition_coeffs(T)
    diff_data = diffusion_data(T)
    # substitutional elements
    subs = ["CR", "MN", "MO", "NI", "SI"]
    # reduce the data to the wanted system
    k_p = get_system_data(eq_data, subs)
    d_m = get_system_data(diff_data, subs)
    # Equilibrium cementite fraction
    feq_cem = 0.06
    # Set-up Matrix content
    alloy_wt = ["C": 0.4e-2, "CR": 0.8e-2, "MN": 0.7e-2, "MO": 0.25e-2, "NI": 1.825e-2,
"SI": 0.225e-2 ]
    alloy_mol = nominal_composition (alloy_wt)
    alloy_subs_content = get_system_data (alloy_mol, subs)
    c_m_s = alloy_subs_content / (1.0 + (k_p - 1.0) * feq_cem)
```

```
# Initial values
r0_c = ((2.26 - 6.4e-3 * T + 4.6e-6 * T **2 ) * feq_cem * 1e-3) ** (1.0 / 3.0) * 1e-6
G0 = (2.7e-3 * T - 2.027) * 1e-6
#print G0, r0_c
y0 = [G0, r0_c]
# Interfacial energy
int_en = 0.550
# Pack the arguments (temperature, cementite eq fraction, interfacial energy, matrix equilibrium,
args = (T, feq_cem, int_en, c_m_s, k_p, d_m)
# Set-up time discretization
t = np.logspace(0, 6, num = 500)
# Solve the ode system
sol = odeint(coarsening_with_ferrite_growth, y0, t, args=args)

time = [1, 600, 3600, 14400, 43200, 86400, 174000]
rs_cube = [5.83e-23, 7.48e-23, 2.68e-22, 4.55e-22, 1.62e-21, 3.73e-21, 4.73e-21]
rs = [ r_cube ** (1/3.0) * 1e6 for r_cube in rs_cube ]

plt.semilogx(t, sol[:, 0] * 1e6, 'b', lw=2, label='Ferrite Grain Growth')
plt.semilogx(t, sol[:, 1] * 1e6, 'g', lw=2, label='Cementite Growth')
# plt.semilogx(time, rs, "og")
plt.legend(loc='best')
plt.xlabel(r't (sec.)', fontsize=14)
plt.ylabel(r'radius ($\mu$m)', fontsize=14)
plt.ylim(0, 2.5)
plt.grid()
plt.savefig("results_sig_55mJ.png", dpi=400)
```

BIBLIOGRAPHY

(2011). "DICTRA Software MOBFE2 version 2."

(2013). DICTRA: 'Examples f1: Coarsening of a M6C precipitate in an Fe-Mo-C alloy', Thermo-Calc Software AB, http://www.thermocalc.se.

(2013). Thermo-Calc Software 3.1, TCFE version 7.

Andersson, J.-O. and J. Ågren (1992). "Models for numerical treatment of multicomponent diffusion in simple phases " J. Appl. Phys. **72**: 1350-1355.

Andersson, J.-O., L. Höglund, B. Jönsson and J. Ågren (1990). "Computer simulation of multicomponent diffusional transformations in steel." Fundamentals and Applications of Ternary Diffusion, edited by G.R. Purdy, Pergamon Press, New York, NY: 153-163.

Andersson, J. O., T. Helander, L. Höglund, P. F. Shi and B. and Sundman (2002). Thermo-Calc 3.1 and DICTRA 27, Computational tools for materials science, CALPHAD, 26, **:** 273-312.

Ardell, A. J. (1997). "Temporal behavior of the number density of particles during Ostwald ripening." Material Science and Engineering A **238**: 108-120.

Ardell, A. J. (2013). "Trans-interface-diffusion-controlled coarsening in ternary alloys." Acta Materialia **61**(20): 7749-7754.

ASM (1977). Atlas of isothermal transformation and cooling transformation diagrams. Metals Park, Ohio, USA, American Society for Metals.

ASM (1995). Heat Treater's Guide: Practices and Procedures for Irons and Steels, ASM Internatinal.

Ausseil, L. (2016). Méthodes de Caractérisation des Propriétés Thermomécaniques d'un Acier Martensitique. M. Sc. A., École de Technologie Supérieure, Montreal, Canada.

Ayache, J., L. Beaunier, J. Boumendil, G. Ehret and D. Laub (2010). Sample Preparation Handbook for Transmission Electron Microscopy: Methodology. New York, Springer-Verlag

Baldan, A. (2002). "Review Progress in Ostwald ripening theories and their applications to nickel-base superalloys Part I: Ostwald ripening theories." Journal of Materials Science **37**(11): 2171-2202.

Bhadeshia, H. and R. Honeycombe (2006). Steels: Microstructure and Properties. Oxford, UK, Butterworth-Heinemann.

Bhadeshia, H. K. D. H. (1989). "Theoretical analysis of changes in cementite composition during tempering of bainite." Materials Science and Technology **5**(2): 131-137.

Björklund, S., L. F. Donaghey and M. Hillert (1972). "The effect of alloying elements on the rate of ostwald ripening of cementite in steel." Acta Metallurgica **20**(7): 867-874.

Bramfitt, B. L. and A. O. Benscoter (2002). Metallographer's guide : practices and procedures for irons and steels. Metals Park, Ohio, American Society for Metals.

Byeon, J. W. and S. I. Kwun (2003). "Nondestructive evaluation of thermally degraded 2.25 Cr-1Mo steel by electrical resistivity measurement." Materials Transactions **44**(6): 1204-1208.

Caron, R. N. and G. Krauss (1972). "The tempering of Fe-C lath martensite." Metallurgical and Materials Transactions B **3**(9): 2381-2389.

Chang, L. and G. Smith (1984). "The silicon effect in the tempering of martensite in steels." Le Journal de Physique Colloques **45**(C9): C9-397-C399-401.

Clarke, A. J., M. K. Miller, R. D. Field, D. R. Coughlin, P. J. Gibbs, K. D. Clarke, D. J. Alexander, K. A. Powers, P. A. Papin and G. Krauss (2014). "Atomic and nanoscale chemical and structural changes in quenched and tempered 4340 steel." Acta Materialia **77**: 17-27.

Clarke, K. (2008). The effect of heating rate and microstructural scale on austenite formation, austenite homogenization, and as-quenched microstructure in three induction hardeable steels Ph.D. thesis, Colorado School of Mines (CSM).

Clarke, K., C. Van Tyne, C. Vigil and R. Hackenberg (2011). "Induction Hardening 5150 Steel: Effects of Initial Microstructure and Heating Rate." Journal of Materials Engineering and Performance **20**(2): 161-168.

Coates, D. E. (1972). "Diffusion-controlled precipitate growth in ternary systems I." Metallurgical and Materials Transactions B **3(5)**: 1203-1212.

Coates, D. E. (1973). "Diffusion controlled precipitate growth in ternary systems: II. ." Metallurgical and Materials Transactions B **4(4)**: 1077-1086.

Coates, D. E. (1973). "Precipitate growth kinetics for Fe-C-X alloys." Metallurgical and Materials Transactions B, **4**(1): 395-396.

Cong, Z. and Y. Murata (2011). "Dislocation Density of Lath Martensite in 10Cr-5W Heat-Resistant Steels." Materials Transactions **52**(12): 2151-2154.

De Geuser, F. and A. Deschamps (2012). "Precipitate characterisation in metallic systems by small-angle X-ray or neutron scattering." Comptes Rendus Physique **13**: 246-256.

Ducassy, C. (2010). Prediction of the hardness and the depth of the area on tempering at a rapid induction heating of 4340 steel tempered. M.Eng., L'école de Technologie Supérieure, Montreal, Canada.

Ducassy, C., F. Bridier, P. Bocher and P. Arkinson (2009). "Semi-Empirical Method to Predict Hardness during fast Induction Heating of aTempered Martensitic AMS 6414 Steel." 1st Mediterranean Conference on Heat Treatment and Surface Engineering: 43-52.

Ghosh, G. and G. B. Olson (2002). "Precipitation of paraequilibrium cementite: Experiments, and thermodynamic and kinetic modeling." Acta Materialia **50**(8): 2099-2119.

Ghosh, S. (2010). "Rate-controlling parameters in the coarsening kinetics of cementite in Fe–0.6C steels during tempering." Scripta Materialia **63**(3): 273-276.

Greenwood, G. W. (1956). "The growth of dispersed precipitates in solutions." Acta Metallurgica **4**(3): 243-248.

Grum, J. (2007). "Overview of residual stresses after induction surface hardening." International Journal of Materials and Product Technology **29**(1-4): 9-42.

Guide, T.-C. C. M. U. s. (2013). Thermo-Calc Software AB, Stockholm, Sweden; http://www.thermocalc.com.

Hillert, M. (1986). "Impact of Clarence Zener upon metallurgy." Journal of Applied Physics **60**(6): 1868-1876.

Hillert, M. (2008). Phase Equilibria, Phase Diagrams and Phase Transformations: Their Thermodynamic Basis. New York, USA, Cambridge University Press.

Hoyt, J. J. (1998). "Coarsening in multiphase multicomponent systems—I. The mean field limit." Acta Materialia **47**(1): 345-351.

Hu, X., L. Li, X. Wu and M. Zhang (2006). "Coarsening behavior of M23C6 carbides after ageing or thermal fatigue in AISI H13 steel with niobium." International Journal of Fatigue **28**(3): 175-182.

Hull, D. and D. J. Bacon (2011). Chapter 10 - Strength of Crystalline Solids. Introduction to Dislocations (Fifth Edition). D. Hull and D. J. Bacon. Oxford, UK, Butterworth-Heinemann**:** 205-249.

Jönsson, B. (1992). "On Ferromagnetic Ordering and Lattice Diffusion: A Simple Model. ." Zeitschrift für Met. **83**: 349-355.

Jönsson, B. (1994). " Ferromagnetic ordering and diffusion of carbon and nitrogen in bcc Cr-Fe-Ni alloys. ." Zeitschrift für Met. **85**: 498-501.

Jönsson, B. (1995). "Assessment of the Mobilities of Cr, Fe and Ni in bcc Cr-Fe-Ni Alloys. ." ISIJ International: pp. 1415-1421, .

Kim, B., E. Boucard, T. Sourmail, D. San Martín, N. Gey and P. E. J. Rivera-Díaz-del-Castillo (2014). "The influence of silicon in tempered martensite: Understanding the microstructure–properties relationship in 0.5–0.6 wt.% C steels." Acta Materialia **68**: 169-178.

Kim, B., C. Celada, D. San Martín, T. Sourmail and P. E. J. Rivera-Díaz-del-Castillo (2013). "The effect of silicon on the nanoprecipitation of cementite." Acta Materialia **61**(18): 6983-6992.

Kozeschnik, E. and H. Bhadeshia (2008). "Influence of silicon on cementite precipitation in steels." Materials Science and Technology **24**(3): 343-347.

Krauss, G. (2005). Steels: Processing, Structure, and Performance. Materials Park, Ohio, USA, ASM International.

Kuehmann, C. J. and P. W. Voorhees (1996). "Ostwald ripening in ternary alloys." Metallurgical and Materials Transactions A **27**(4): 937-943.

Lankford, W. T., N. L. Samways, R. F. Craven and H. E. McGannon (1985). The making, shaping and treating of steel. Pittsburgh, Pa., United States Steel Corporation Association of Iron and Steel Engineers.

Lee, H., S. Allen and M. Grujicic (1991). "Coarsening resistance of M2C carbides in secondary hardening steels: Part I. Theoretical model for multicomponent coarsening kinetics." Metallurgical and Materials Transactions A **22**(12): 2863-2868.

Lee, H. M. and S. M. Allen (1991). "Coarsening resistance of M2C carbides in secondary hardening steels: Part III. Comparison of theory and experiment." Metallurgical and Materials Transactions A **22**(12): 2877-2888.

Lewis, H. D., K. L. Walters and K. Allan Johnson (1973). "Particle size distribution by area analysis: Modifications and extensions of the Saltykov method." Metallography **6**(2): 93-101.

Lifshitz, I. M. and V. V. Slyozov (1961). "The kinetics of precipitation from supersaturated solid solutions." Journal of Physics and Chemistry of Solids **19**(1): 35-50.

Liu, Z. K. and J. Agren (1989). "On the Transition from Local Equilibrium to Paraequilibrium during the Growth of Ferrite in Fe-Mn-C Austenite." Acta Metallurgica **37,** (12): 3157-3163.

Lv, Z., S. H. Sun, Z. Wang, M. G. Qv, P. Jiang and W.-t. Fu (2008). "Effect of alloying elements addition on coarsening behavior of pearlitic cementite particles after severe cold rolling and annealing." Materials Science and Engineering A **489**(1-2): 107-112.

Lv, Z. Q., B. Wang, Z. H. Wang, S. H. Sun and W. T. Fu (2013). "Effect of cyclic heat treatments on spheroidizing behavior of cementite in high carbon steel." Materials Science and Engineering: A **574**: 143-148.

Malik, L. and J. Lund (1972). "A study of strengthening mechanisms in tempered martensite from a medium carbon steel." Metallurgical Transactions **3**(6): 1403-1406.

Malik, L. M. (1972). Strengthening mechanisms in some heat-treated low alloy steels. Ph.D. thesis, University of British Columbia, Vancouver, Canada.

Martin, J. W., R. D. Doherty and B. Cantor (1997). Stability of microstructure in metallic systems. Cambridge, U.K., Cambridge University Press.

Massih, A. R. and L. O. Jernkvist (2009). "Transformation kinetics of alloys under non-isothermal conditions." Modelling and Simulation in Materials Science and Engineering **17**(5): 15.

Morral, J. E. and G. R. Purdy (1994). "Particle coarsening in binary and multicomponent alloys." Scripta Metallurgica et Materialia **30**(7): 905-908.

Morral, J. E. and G. R. Purdy (1995). "Thermodynamics of particle coarsening." Journal of Alloys and Compounds **220**(1–2): 132-135.

Murphy, S. and J. H. Woodhead (1972). "An investigation of the validity of certain tempering parameters." Metallurgical and Materials Transactions B **3**(3): 727-735.

Nicolas, M. (2009). Precipitation evolution in an Al-Zn-Mg alloy during non-isothermal heat treatments and in the heat-affected zone of welded joints. Ph.D. thesis, Institut National Polytechnique de Grenoble, France.

Nishizawa, T. (2008). Thermodynamics of microstructures. Ohio, USA, ASM International

Pandit, A. S. (2011). Theory of the pearlite transformation in steels. Ph.D. thesis, University of Cambridge, Cambridge, England.

Perez, M. (2005). "Gibbs–Thomson effects in phase transformations." Scripta Materialia **52**(8): 709-712.

Philippe, T. and P. W. Voorhees (2013). "Ostwald ripening in multicomponent alloys." Acta Materialia **61**(11): 4237-4244.

Porter, D. A. and K. E. Easterling (1992). Phase transformations in metals and alloys. London, England, Chapman & Hall, .

Ratke, L. and C. Beckermann (2001). "Concurrent growth and coarsening of spheres." Acta Materialia, Inc. **49**: 4041–4054.

Rudnev, V. (2005). Be Aware of the 'Fine Print' In the Science of Metallurgy of Induction Hardening: Part 2. Inductoheat Group, Madison Heights, Mich, Heat treating.

Rudnev, V. (2005). Metallurgical 'Fine Points' of Induction Hardening. Inductoheat Group, Madison Heights, Mich, Heat treating.

Rudnev, V. (2008). Induction Hardening of Gears and Critical Components: Part II, Geartechnology.

Rudnev, V., D. Loveless, R. Cook and M. Black (2003). Handbook of Induction Heating. New York, Marcel Dekker Inc.

Rudnev, V., D. Loveless, R. Cook and M. Black (2003). Induction Hardening of Gears: a Review, Heat treatments of the metals**:** 97-103.

Savaria, V. (2014). Contraintes Résiduelles et Leurs Impacts Sur L'amorçage de Fissures en Fatigue de Flexion dans des Engrenages Aéronautiques Durcis Superficiellement par Induction. Ph.D. thesis, Ecole de Technologie Supérieure, Montreal, Canada.

Schindelin, J., I. Arganda Carreras, E. Frise, V. Kaynig, M. Longair, T. Pietzsch, S. Preibisch, C. Rueden, S. Saalfeld, B. Schmid, J.-Y. Tinevez, D. J. White, V. Hartenstein, K. Eliceiri, P. Tomancak and A. Cardona (2012). "Fiji: an open-source platform for biological-image analysis." Nat Meth **9**(7): 676-682.

Schneider, A. and G. Inden (2005). Computer Simulation of Diffusion Controlled Phase Transformations. Continuum Scale Simulation of Engineering Materials, Wiley-VCH Verlag GmbH & Co. KGaA**:** 1-36.

Schneider, C. A., W. S. Rasband and K. W. Eliceiri (2012). "NIH Image to ImageJ: 25 years of image analysis." Nat Meth **9**(7): 671-675.

Speich, G. R. and W. C. Leslie (1972). "Tempering of steel." Metallurgical and Materials Transactions B **3**(5): 1043-1054.

Tiryakioğlu, M., G. Ökten and D. Hudak (2009). "Statistics for estimating the population average of a Lifshitz–Slyozov–Wagner (LSW) distribution." Journal of Materials Science **44**(21): 5754-5759.

Umantsev, A. and G. B. Olson (1993). "Ostwald ripening in multicomponent alloys." Scripta Metallurgica et Materialia **29**(8): 1135-1140.

Underwood, E. E. (1969). "Stereology, or the quantitative evaluation of microstructures." Journal of Microscopy **89**: pp. 161-180.

Underwood, E. E. (1970). Quantitative Stereology, Reading, Mass., Addison-Wesley.

Valery, I. and V. Rudnev (2007). Metallurgical insights for induction heat treaters Part 3: Limitations of TTT And CCT Diagrams. Inductoheat Group, Madison Heights, Mich, Heat Treating Progress.

Vedula, K. and R. Heckel (1970). "Spheroidization of binary Fe-C alloys over a range of temperatures." Metallurgical Transactions **1**(1): 9-18.

Venugopalan, D. (1977). Kinetics of tempering in low alloy steel M.Eng., Mc Master University, Canada.

Venugopalan, D. and Kirkaldy.J.S (1978). "New relations for predicting the mechanical properties of quenched and tempered low alloy steels." Hardenability Concepts with Applications to Steels, AIME, New York: 249.

Wang, Y. (2006). Etude et modélisation de l'effet du revenu sur les évolutions des microstructures, du comportement thermomécanique et des contraintes résiduelles de trempe. Ph.D. thesis, Institut National Polytechnique de Lorraine, France.

Wang, Y., B. Appolaire, S. Denis, P. Archambault and B. Dussoubs (2006). "Study and modelling of microstructural evolutions and thermomechanical behaviour during the tempering of steel." Int.J. Microstructure and Materials Properties **1**(2): 197-207.

Yang, B. J., A. Hattiangadi, W. Z. Li, G. F. Zhou and T. E. McGreevy (2010). "Simulation of steel microstructure evolution during induction heating." Materials Science and Engineering: A **527**(12): 2978-2984.

Zhirafar, S., A. Rezaeian and M. Pugh (2007). "Effect of cryogenic treatment on the mechanical properties of 4340 steel." Journal of Materials Processing Technology **186**(1): 298-303.

Zhu, C., X. Y. Xiong, A. Cerezo, R. Hardwicke, G. Krauss and G. D. W. Smith (2007). "Three-dimensional atom probe characterization of alloy element partitioning in cementite during tempering of alloy steel." Ultramicroscopy **107**(9): 808-812.